12-10-2010

Tunable Optical Delay in Doppler-Broadened Cesium Vapor

Monte D. Anderson

TUNABLE OPTICAL DELAY IN DOPPLER-BROADENED CESIUM VAPOR

DISSERTATION

Monte D. Anderson, Lieutenant Colonel, USAF

AFIT/DS/ENP/10-S01

DEPARTMENT OF THE AIR FORCE
AIR UNIVERSITY

AIR FORCE INSTITUTE OF TECHNOLOGY

Wright-Patterson Air Force Base, Ohio

The views expressed in this dissertation are those of the author and do not reflect the official policy or position of the United States Air Force, the Department of Defense or the United States Government.

AFIT/DS/ENP/10-S01

TUNABLE OPTICAL DELAY IN DOPPLER-BROADENED CESIUM VAPOR

DISSERTATION

Presented to the Faculty

Graduate School of Engineering and Management

Air Force Institute of Technology

Air University

Air Education and Training Command

in Partial Fulfillment of the Requirements for the

Degree of Doctor of Philosophy

Monte D. Anderson, BS, MS

Lieutenant Colonel, USAF

December 2010

AFIT/DS/ENP/10-S01

TUNABLE OPTICAL DELAY IN DOPPLER-BROADENED CESIUM VAPOR

Monte D. Anderson, BS, MS
Lieutenant Colonel, USAF

Approved:

Glen P. Perram, PhD (Chairman)	Date
David E. Weeks, PhD (Member)	Date
Peter E. Powers, PhD (Member)	Date

Accepted:

M. U. Thomas Dean, Graduate School of Engineering and Management	Date

Abstract

Variable-delay tunable optical delay line or optical buffers are critical for the development of all-optical networks components as well as interferometry and analytic instruments. Recent research on slow light may hold the key for the development of the first practical tunable optical delay device. In this research an atomic vapor pulse delay model is developed including hyperfine structure and Voigt lineshape. Frequency tunable pulse delays of 0-37 ns are achieved in Cs D_2 at various vapor pressures of 0.15-5.28 mTorr between 78.9 °C and 137.2 °C in agreement with model prediction. Furthermore full-frequency Cs D_1 line hyperfine optical delay model is validated with the observation of delays of 1.6 ns to 24.1 ns. Additional optical control of delays were demonstrated by pumping the Cs D_2 transition and observing resulting effects in the D_1 delay spectrum. For a pump at four times the saturation intensity, delays are reduced by a maximum of 78% in a narrow region of 110 MHz in agreement with a Kramers-Kronig model prediction. Diode-pumped alkali laser (DPAL) systems depend on accurate models to scale to high power and optimize performance. There is currently no validated bleach wave model of an operating DPAL system. This work partially examines the bleached wave temporal dynamics during a 10 ns high-power D_2 pulse event with 0-400 Torr helium buffer gas. The linear dispersion delay model is a valuable improvement over currently used Lorentzian approximations and provides a significant addition to the field tunable slow light delays. This work presents the first reported spectral hole-burnt linear dispersion delay effects in an alkali vapor. The hyperfine relaxation observations present insight into the complex bleach wave dynamics during a high-intensity pulsed pump in DPAL systems.

To my family

Acknowledgements

I would like to express my sincere appreciation to my advisor Professor Glen Perram, for his guidance and support through the course of my research.

Research would not be complete without those who directly helped in the laboratory taking data and performing experiments including Eric Guild, Michael Cox, and Paul Stanczak. In the laboratory no experiment is complete without technical issues–I would like to thank laboratory technicians Greg Smith and Mike Ranft for their rapid response to all my fires. Special thanks to the Diode Pumped Alkali Laser (DPAL) group especially Greg Pitz and Cliff Sulham. I greatly appreciate Professor John Howell from the University of Rochester for his discussions on slow light in alkali vapor. This work is supported by the Joint Technology Office and the Air Force Office of Scientific Research.

Finally thanks to my family for their support and understanding throughout the course of my research.

Monte D. Anderson

Table of Contents

Page

List of Figures

List of Tables

TUNABLE OPTICAL DELAY IN DOPPLER-BROADENED CESIUM VAPOR

I. Introduction

Variable-delay tunable optical delay line or optical buffers are critical for the development of all-optical networks and optical signal processing (Tucker et al., 2005). Applications for tunable optical delay systems include simple optical delay lines, optical switches and optical storage devices for optical communication systems (Camacho et al., 2007; Tucker et al., 2005), as well as interferometry (Shi et al., 2007; Purves et al., 2006) for remote sensing and analytic instruments (Camacho et al., 2006b). Recent research in an emerging field of optical physics known as slow light may hold the key for the development of the first practical tunable optical delay applications.

Simply stated, "group velocity gives the velocity with which a pulse of light propagates through a material system" (Boyd and Gauthier, 2002). Boyd defines the terms "fast" and "slow" light by comparing the group velocity to the velocity of light c.

> *Recent research has established that it is possible to exercise extraordinary control of the velocity of propagation of light pulses through a material system. Both extremely slow propagation (much slower than the velocity of light in vacuum) and fast propagation (exceeding the velocity of light in vacuum) have been observed.* (Boyd and Gauthier, 2002)

A number of methods have been employed to achieve slow light including exploiting the natural resonant absorption in atomic systems (Khurgin and Tucker, 2009), self-induced transparency (SIT) (Allen and Eberly, 1987) and electronically-induced transparency (EIT) (Marangos, 1998; Milonni, 2002; Boyd and Gauthier, 2002; Fleischhauer et al., 2005; Milonni, 2005). Ideal optical system components for optical delay should have long delay/buffer times, no loss of signal amplitude and no dispersion.

For a delay system to be of practical use in future applications it must be capable of storing large streams of optical information, and allow for random access of buffered optical signals all in compact physical dimensions(Tucker et al., 2005). Fundamental understanding of the delay effects on optical pulse propagation and accurate delay prediction are essential for any slow light system.

The study of slow light in atomic vapors have played an important role in the development of tunable optical delay systems. Many of the preliminary studies in slow light were accomplished using atomic vapors (Khurgin and Tucker, 2009). Knowledge of the physics of slow light in atomic vapors are important in developing any practical optical buffer system. Alkali-metal elements offer well-documented relatively simple atomic systems with physical properties, such as large vapor pressures at moderate temperatures, that make them ideal for slow light laboratory media.

It has been theorized (Brillouin, 1960; Garrett and McCumber, 1970) and demonstrated (Grischkowsky, 1973; Tanaka et al., 2003) to some degree that optical pulse delay is achievable using a single laser tuned in the neighborhood of resonant atomic transitions. Full frequency-dependent delay models have not been developed. In this work a frequency-dependent Kramers-Kronig delay model is developed using complete hyperfine structure treatment with Voigt profile lineshapes in a Doppler-broadened alkali-metal vapor. Delay predictions are compared to observed pulse delay to validate the delay model.

In EIT narrow transmission windows generate areas of steep dispersion. Similarly it has been theorized that spectral holes in an absorption profile could be used to produce tunable delay effects (Shakhmuratov et al., 2005; Agarwal and Dey, 2003). The slow light hole burning technique has been demonstrated in solid photonic media (Bigelow et al., 2003) and recently rubidium vapor (Camacho et al., 2006b). Previous work focused on frequency modulated pump beam. In this work control of pulse delays in cesium vapor were demonstrated by pumping the D_2 $(6\,^2\mathrm{S}_{1/2} - 6\,^2\mathrm{P}_{1/2})$

transition and observing resulting holes in the D_1 delay spectrum. Additionally the frequency dependence of the delays of the probe laser in the vicinity of the spectral holes is examined and compared to the Kramers-Kronig model prediction.

Tunable optical delay systems used in this research are similar to diode-pumped alkali laser (DPAL) system (Rabinowitz et al., 1962; Krupke et al., 2003; Ehrenreich et al., 2005; Beach et al., 2004) and application of the knowledge gained in pulse propagation can be useful in the understanding of the temporal dynamics of a DPAL system. Normally three-level lasers are not possible due to the difficulty in achieving population inversion. The alkali-laser is a gas-phase three-level laser using the ground state ($S_{1/2}$) and the first two excited states ($P_{1/2}$ and $P_{3/2}$) of the alkali-metal vapor. Population from the upper $P_{3/2}$ state is transferred to the lasing $P_{1/2}$ level through a collisional gas species like ethane or methane. The recycle rate at which an individual photon excites the atom, collisionally transferred to the lasing level and lases is very rapid, the quantum efficiency of such a three-level system is higher than other laser systems, and the gas-phase laser does not have the thermal management issues of solid-state laser systems. While DPAL systems have been in use for several years, complete theoretical description of the system is still being developed in order to optimize the lasers for scaling to high output power. Optimization of a DPAL system depends on accurate pressure-broadening models to properly match the atomic absorption profile to the broadband diode pump source. There is currently no validated bleach wave model of an operating DPAL system. Transverse absorption spectroscopy setup is used in this work to partially examine the temporal dynamics of the bleached wave of a pulsed alkali-metal vapor system.

II. Background

Theoretical foundations of for slow light have been well-known for for over a century. The concept of group velocity originated in the study of sound waves by Sir William R. Hamilton (1839) and Lord Rayleigh (1894) (Brillouin, 1960). The problem was of considerable interest in connection with the velocity of light in the early 1900's after Albert Einstein's Special Theory of Relativity because of the possibility of propagation faster than the speed of light, c (Boyd and Gauthier, 2002). In 1907 Arnold Sommerfeld and later in 1914, Sommerfeld and Léon Brillouin, developed the theory of pulse propagation through a collection of Lorentz oscillators (treating photon-atoms interactions as oscillators). As outlined by Brillouin in "Wave Propagation and Group Velocity" (Brillouin, 1960), they concluded that a pulse front travels at c regardless of propagation region and that no signal velocity could exceed c in agreement with Einstein's theory (Brillouin, 1960). However, group velocity, often confused with signal velocity, could be greater than c, less than c, or even take on negative values.

Since the early theoretical work atomic vapors have played a role in the study of slow light and continue to be integral to the fundamental understanding of optical delay research (Khurgin and Tucker, 2009). Slow light research in atomic vapors is broadly categorized by the method used to achieve tunable group delays.

In the simplest case low intensity laser light near naturally occurring resonant atomic transitions of a two-level system provide the necessary dispersion to induce pulse delays (Khurgin and Tucker, 2009). This dissertation will refer to this simple linear case of absorption or refractive index variation as dispersion delay. Typical dispersion delay experiments occur within the linear intensity regime and can be adequately described using the semi-classical approach where the atom is treated quantum mechanically and the field is treated classically.

Historically early studies of slow light were performed as non-linear optics shortly after the invention of the laser (Khurgin and Tucker, 2009). Self-induced transparency (SIT) was first discovered by McCall and Hahn in 1967 (McCall and Hahn, 1967). McCall and Hahn passed pulses generated by a ruby laser through additional ruby rods and observed significant group delay and SIT effect where coherent light near the resonant transition frequency is transmitted with little loss of pulse amplitude. Study of SIT was later applied to gases such as sulphur hexafluoride SF_6 (Patel and Slusher, 1967) and eventually alkali-metal vapors (Bradley et al., 1970; Slusher and Gibbs, 1972). The SIT effect is dependent on the nonlinearity in laser intensity but is similar to dispersion delay in the wings of the absorption profile.

The third major category of slow light mechanisms is electrically-induced transparency (EIT) discovered by Harris *et al.* (Harris et al., 1990). EIT is a coherent optical effect which creates a narrow transparency window due to quantum interference between states to eliminate absorption at the resonant transition frequency (Marangos, 1998; Fleischhauer et al., 2005).

This chapter begins with the necessary foundation in semi-classical theory to explain dispersion delay in the linear region, followed by a discussion of SIT in terms of non-linear optics and EIT in common quantum optics notation. Pertinent research relevant to the understanding of slow light and tunable delays will be presented. Finally a brief description of diode pumped alkali lasers and their similarity to slow light study will be discussed.

Semi-Classical Wave Propagation

From Maxwell equations it is understood that electromagnetic fields have wavelike solutions. Consider the electric field in the common monochromatic plane wave form

$$E(z,t) = E_0 \exp\{i\,(kz - \omega t)\} \tag{1}$$

where $k = n\omega/c = 2\pi/\lambda$, and angular frequency $\omega = 2\pi\nu$ with refractive index n and the speed of light in a vacuum c.

Phase velocity $v_\phi$is the speed with which cophasal surfaces advance in the medium (Born and Wolf, 1999). The phase of the plane wave is given by

$$\phi = kz - \omega t \tag{2}$$

so that points of constant phase move a small distance δz in a small time δt such that

$$k\delta z = \omega\delta t \tag{3}$$

The phase velocity is the *distance/time* or $v_\phi = \delta z/\delta t$,

$$v_\phi = \frac{\omega}{k} = \frac{c}{n} \tag{4}$$

In the medium, the peak of a pulse, or peak of the group, moves with the same phase, thus the phase

$$\phi = kz - \omega t = \frac{n\omega}{c} z - \omega t. \tag{5}$$

If the phase at the peak remains constant with respect to ω, so that $\partial\phi/\partial\omega = 0$

$$\begin{aligned} \frac{\partial\phi}{\partial\omega} &= 0 \\ \frac{\partial n}{\partial\omega}\frac{\omega z}{c} + \frac{nz}{c} - t &= 0 \\ \left\{\frac{\partial n}{\partial\omega}\frac{\omega}{c} + \frac{n}{c}\right\} z - t &= 0 \end{aligned} \tag{6}$$

Rewriting Equation (6) as $z = v_g t$ the group velocity v_g is

$$v_g = \frac{c}{n + \omega\frac{\partial n}{\partial\omega}} = \frac{\partial\omega}{\partial k} \tag{7}$$

Equation (7) may also be written as in terms of the group index of refraction n_g

$$v_g = \frac{c}{n_g} \tag{8}$$

where

$$n_g = n + \omega\frac{\partial n}{\partial\omega}. \tag{9}$$

Starting the works of Hamilton and Raleigh in the field of sound waves, the treatment wave propagation was extended to optics and the speed of a pulse of light. Phase velocity v_ϕ and group velocity v_g are used to describe the velocity of the phase front and propagation a packet. Sommerfeld and Brillouin defined the velocities and clearly outlines how subluminal and superluminal velocities do not violate Einstein causality (Brillouin, 1960). Furthermore Brillouin discussed the Voigt profile and the effects of dispersion near atomic resonant absorption lines (Brillouin, 1960). Subsequent works depend on these fundamental velocity definitions.

An analytical discussion of the effect on pulse propagation near an absorption line is given by C. G. B. Garrett and D. E. McCumber (Garrett and McCumber, 1970). In their article they discuss the potential for superluminal or subluminal velocities in

various regions and show that the pulse remains unchanged (substantially Gaussian) (Garrett and McCumber, 1970).

Complex Index of Refraction

Slow and fast light effects are dependent on rapid variations in the index of refraction as a function of frequency (i.e. dispersion) that occurs in the vicinity of resonant material properties of the propagation medium (Boyd and Gauthier, 2002). Index of refraction is a complex quantity given by the equation

$$\tilde{n} = n_R + i\, n_I \tag{10}$$

Based on the macroscopic Maxwell equations, beam intensity is determined by the Poynting vector $\mathbf{S}$ (Griffiths, 1999)

$$\mathbf{S} = \mathbf{E} \times \mathbf{H} \tag{11}$$

$$= \frac{1}{\mu_0}(\mathbf{E} \times \mathbf{B}) \tag{12}$$

$$= \epsilon_0 c^2 (\mathbf{E} \times \mathbf{B}) \tag{13}$$

where the magnitude of $\mathbf{E}$ and $\mathbf{B}$ are related by

$$\mathbf{E} \times \mathbf{B} = \frac{1}{c}\mathbf{E} \cdot \mathbf{E}^* \tag{14}$$

such that, the time-averaged Poynting vector in terms of the electric field yields

$$I = \langle \mathbf{S} \rangle = \epsilon_0 c \, \langle \mathbf{E} \cdot \mathbf{E}^* \rangle \tag{15}$$

Given the electric field as in Equation (1), using complex index of refraction $\tilde{n}$

$$E(z,t) = E_0 \exp\left[i\left(\tilde{n}\frac{\omega}{c}z - \omega t\right)\right] \tag{16}$$

$$= E_0 \exp\left[i\left(n_R\frac{\omega}{c}z - \omega t\right) - n_I\frac{\omega}{c}z\right] \tag{17}$$

so that

$$\mathbf{E}\cdot\mathbf{E}^* = E_0^2 \exp\left[i\left(n_R\frac{\omega}{c}z - \omega t\right) - n_I\frac{\omega}{c}z\right]\exp\left[-i\left(n_R\frac{\omega}{c}z - \omega t\right) - n_I\frac{\omega}{c}z\right] \tag{18}$$

$$= E_0^2 \exp\left[-2n_I\frac{\omega}{c}z\right] \tag{19}$$

$$= E_0^2 \exp\left[-\alpha(\omega)z\right] \tag{20}$$

where

$$\alpha(\omega) = \frac{2\omega}{c}n_I \quad \text{or} \quad \alpha(\nu) = \frac{4\pi\nu}{c}n_I. \tag{21}$$

Intensity becomes

$$I = \epsilon_0 c E_0^2 \exp\left[-\alpha(\omega)z\right] \tag{22}$$

which decreases exponentially with z if α is positive. Hence α, in cm^{-1}, is called the absorption coefficient if α is positive or gain if α is negative. Notation may vary in other sources if the sign is included in the coefficient.

Given the intensity at the beginning of the medium, $z = 0$, is

$$I(z=0) = I_0. \tag{23}$$

The ratio of the intensity at a given depth z relative to the initial intensity I_0 is

$$I(z) = I_0 \exp\left[-\alpha(\omega)z\right]. \tag{24}$$

This relation known as the Beer-Lambert law (or simply Beer's law) is true only in the linear regime when the intensity I is below the saturation intensity I_{sat}.

Kramers-Kronig Relations

Both parts of the complex index of refraction gives light to important phenomena– the real index of refraction effects group velocity and the imaginary index of refraction accounts for observed absorption in a dispersive medium. The Kramers-Kronig relations connect the real and imaginary parts of the complex index of refraction, assuming $\tilde{n}(\omega)$ is regular at $\omega = 0$ (Jackson, 1999) (Hutchings et al., 1992).

$$n_R(\omega) - 1 = \frac{2}{\pi} \, \mathrm{P} \int_0^\infty \frac{\xi n_I(\xi)}{\xi^2 - \omega^2} \, d\xi \tag{25}$$

$$n_I(\omega) = -\frac{2\omega}{\pi} \, \mathrm{P} \int_0^\infty \frac{n_R(\xi) - 1}{\xi^2 - \omega^2} \, d\xi \tag{26}$$

where P is the Cauchy principal value. If either term, n_R or n_I, is known, the other may be determined. From Equation (21)

$$n_I(\nu) = \frac{c}{4\pi\nu}\alpha(\nu) \tag{27}$$

thus Equation (25) can be written in terms of the absorption coefficient as a function of linear frequency ν

$$n_R(\nu) - 1 = \frac{2}{\pi} \, \mathrm{P} \int_0^\infty \frac{\xi \frac{c}{4\pi\xi}\alpha(\xi)}{\xi^2 - \nu^2} \, d\xi \tag{28}$$

$$= \frac{c}{2\pi^2} \, \mathrm{P} \int_0^\infty \frac{\alpha(\xi)}{\xi^2 - \nu^2} \, d\xi \tag{29}$$

We have developed an expression for the real index of refraction $n_R(\nu)$ as a func-

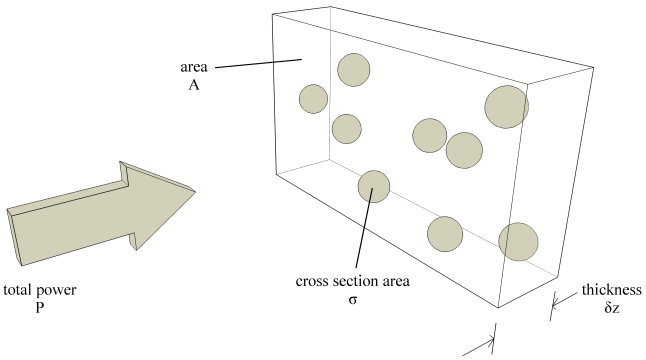

Figure 1. Absorption cross section construct. Atoms within a slab of area A and thickness δz interact with light that strikes in cross sectional area σ_{abs}. Total power P is evenly distributed across the area A.

tion of frequency, known as dispersion (Menzel, 2007). Normally index of refraction increases with increasing frequency known as *normal dispersion*. When index of refraction decreases with increasing frequency, it is known as *anomalous dispersion*.

In spectroscopy it is common to measure attenuation and determine the index of refraction from the Kramers-Kronig relations. For example, an observed discrete absorption line spectrum, discrete step width $\Delta\tilde{\nu}$ in wavenumbers, the discrete values of the dispersion $n_R(p \cdot \Delta\tilde{\nu})$ at the frequencies $p \cdot \Delta\tilde{\nu}$ follow from the Kramers-Kronig relation (Menzel, 2007)

$$n_R(p \cdot \Delta\tilde{\nu}) - n_R(\tilde{\nu} = \infty) = \frac{1}{2\pi^2 \Delta\tilde{\nu}} \sum_{m=0,\neq p}^{\infty} \frac{1 - (-1)^{m+p}}{m^2 - p^2} \alpha(m \cdot \Delta\tilde{\nu}) \qquad (30)$$

Absorption Cross Section

A phenomenological construct for the medium's macroscopic absorption is described using the following model (Siegman, 1986). Consider a slab of material in which absorbing particles are embedded as shown in Figure 1. Number density N is absorbers per unit volume $N = n/V$. For simplicity let the particle cross sectional

area σ_{abs} perpendicular to the incident radiation of total power P represents an area of 100% probability of interaction. Probability of interaction is 0% elsewhere on the surface area of the slab A. Intensity is defined as $I \equiv P/A$. The relative change in intensity of the incident radiation is given by

$$\frac{dI}{I} = \frac{I_{out} - I_{in}}{I_{in}} \tag{31}$$

$$= -\frac{n\sigma_{abs}}{A} \tag{32}$$

$$= -NV\frac{\sigma_{abs}}{A} \tag{33}$$

$$= -\frac{NA\sigma_{abs}\delta z}{A} \tag{34}$$

$$= -N\sigma_{abs}\delta z. \tag{35}$$

Integrating Equation (35) with respect to the distance of propagation through the slab z yields Beer's law attenuation

$$\int_0^z \frac{1}{I}\, dI = -\int_0^z N\sigma_{abs} d\xi \tag{36}$$

$$\ln[I(z)] - \ln[I_0] = -N\sigma_{abs}z \tag{37}$$

$$I(z) = I_0 \exp\left[-N\sigma_{abs}z\right]. \tag{38}$$

Comparing Equation (24) to Equation (38) reveals equations of similar form, such that

$$\alpha(\omega)z = N\sigma_{abs}z \tag{39}$$

$$\alpha(\omega) = N\sigma_{abs}. \tag{40}$$

Applying quantum mechanical principles, we can find the cross section for absorption σ_{abs}. By calculating the number density N as a function of the vapor pressure, we

can calculate the absorption coefficient $\alpha(\nu)$.

If we consider cesium vapor an ideal gas, we can find the number density $N = n/V$ by $n/V = P/k_BT$, where P is the cesium vapor pressure as a function of temperature T given by Equation (104) (Alcock et al., 1984) as shown in Appendix B Figure 42. At this point we seek σ_{abs} as a function of photon-atom interaction to find the absorption coefficient.

Photon-Atom Interaction

Light-matter interactions are described by quantum mechanical transition probabilities. Electric dipole interactions are the dominant factor for determining atomic energy level therefore the matrix elements are based on the electric dipole moment (Fox, 2006). We seek to find the cross section, related to the probability of interaction, in terms of the effective dipole moment $\mu_{F''F'}$ (Steck, 2009, eqn (43))

$$| \mu_{F''F'} |^2 = \frac{1}{3} S_{F''F'} | \langle J | e\mathbf{r} | J' \rangle |^2 \tag{41}$$

where $S_{F''F'}$ is the relative strength factor. The radiative lifetime τ_r is given by (Loudon, 2000, eqn (2.3.21))

$$\frac{1}{\tau_r} = A_{21} = \frac{e^2 \omega_0^3 g_1 D_{12}^2}{3\pi\epsilon_0 \hbar c^3 g_2} = \frac{\omega_0^3}{3\pi\epsilon_0 \hbar c^3} \left(\frac{2J+1}{2J'+1} \right) | \langle J | e\mathbf{r} | J' \rangle |^2 \tag{42}$$

where e is the unit charge, ω_0 is the transition frequency, D_{12} is the transition dipole moment, ϵ_0 is vacuum permittivity, $\hbar$ is the reduced Plank constant, and g_1/g_2 are the

level degeneracies. Equation 42 may be used to solve for the effective dipole moment,

$$|\langle J|e\mathbf{r}|J'\rangle|^2 = \frac{1}{\tau}\frac{3\pi\epsilon_0\hbar c^3}{\omega_0^3}\left(\frac{2J'+1}{2J+1}\right) \tag{43}$$

$$|\mu_{F''F'}|^2 = S_{F''F'}\frac{1}{\tau}\frac{\pi\epsilon_0\hbar c^3}{\omega_0^3}\left(\frac{2J'+1}{2J+1}\right) \tag{44}$$

The absorption cross section is given (Bernath, 2005, eqn (1.57))

$$\sigma_{abs} = \frac{2\pi^2|\mu_{F''F'}|^2}{3\epsilon_0 hc}\nu\ g(\nu-\nu_0) \tag{45}$$

combining Equations (44) and (45) yields

$$\sigma_{abs} = \frac{2\pi^2}{3\epsilon_0 hc}S_{F''F'}\frac{1}{\tau}\frac{\pi\epsilon_0\hbar c^3}{\omega_0^3}\left(\frac{2J'+1}{2J+1}\right)\nu\ g(\nu-\nu_0) \tag{46}$$

$$\sigma_{abs} = \frac{c^2}{24\pi}\frac{1}{\tau}S_{F''F'}\left(\frac{2J'+1}{2J+1}\right)\frac{\nu}{\nu_0^3}\ g(\nu-\nu_0) \tag{47}$$

Line Strength

The remaining pieces in our goal of quantifying the group velocity are related to cesium physical properties and D_1 ($6^2S_{1/2} \rightarrow 6^2P_{1/2}$) and D_2 ($6^2S_{1/2} \rightarrow 6^2P_{3/2}$) D-line properties are cited from published literature, notably Steck's *Cesium D-Line Data* (Steck, 2009), Alcock *et al.* vapor pressure equations (Alcock et al., 1984), and Arimondo *et al.* experimental determination of alkali-metal hyperfine structure (Arimondo et al., 1977). See Appendix B for additional cesium information.

The $S_{F''F'}$ $(6-j)$ symbol provide a measure of the relative strength factors of the

$F'' \rightarrow F'$ transition, given by (Steck, 2009, eqn (41))

$$S_{F''F'} = (2F'+1)(2J+1) \begin{Bmatrix} J & J' & 1 \\ F' & F'' & I \end{Bmatrix}^2 \tag{48}$$

which obeys the probability sum rule

$$\sum_{F'} S_{F''F'} = 1. \tag{49}$$

The values are summarized in Table 8 and Table 9.

For the $S_{1/2}$ ground state, $J = 1/2$, and total nuclear angular momentum $I = 7/2$. $F = J+I$ so that the magnitude of F takes on the values of $|\, J - I \,| \leqslant F \leqslant J+I \Longrightarrow$ $F = 3$ or 4. For the D_1 excited state $P_{1/2}$, $J = 1/2$ and $F = 3$ or 4. See Figure 44. For the D_2 excited state $P_{3/2}$, $J = 3/2$ and $F = 2, 3, 4$ or 5. See Figure 45. The central resonant absorption frequency ν_0 is given in Table 5 and Table 6.

Lineshape Functions

Assuming low alkali vapor pressure such that Cs-Cs collisions are negligible the pressure broadening and spectral line shift are a function of buffer gas pressure alone. The pressure effects are tabulated for several buffer gases in B Table 10.

Pressure effects must be corrected for temperature. Given the data was taken at $T_{data} = 294.15\,\mathrm{K}$, the buffer gas pressure effects on system at temperature T_{sys} (K) and buffer gas pressure P_i (Torr) by

$$\Delta\nu_L = \frac{1}{2\pi}\left(\frac{1}{\tau_r}\right) + \sum_i \gamma_i \left(\frac{T_{sys}}{T_{data}}\right)^{1/2} P_i \tag{50}$$

$$\nu_0 \rightarrow \nu_0 + \sum_i \delta_i \left(\frac{T_{sys}}{T_{data}}\right)^{1/2} \tag{51}$$

where $\Delta\nu_L$ is the Lorentzian line width, ν_0 is the center frequency for each hyperfine line, γ_i is the pressure broadening coefficient for each buffer gas species and δ_i is the frequency shift caused by each buffer gas species.

The lineshape function $g(\nu - \nu_0)$ is a convolution of homogeneous pressure broadening and inhomogeneous Doppler broadening effects. The pressure Broadening (*Lorentzian*) (Bernath, 2005, eqn (1.78)) is given by

$$g_P(\nu - \nu_0) = \frac{\Delta\nu_L/(2\pi)}{(\Delta\nu_L/2)^2 + (\nu - \nu_0)^2} \tag{52}$$

where $\Delta\nu_L$ is the Lorentzian full width at half maximum (FWHM).

The Doppler Broadening (*Gaussian*) (Bernath, 2005, eqn (1.93)) is given by

$$g_D(\nu - \nu_0) = \frac{2}{\Delta\nu_D}\sqrt{\frac{\ln(2)}{\pi}}\exp\left[-4\ln(2)\frac{\nu - \nu_0}{\Delta\nu_D}^2\right] \tag{53}$$

where

$$\Delta\nu_D = 2\nu_0\sqrt{\frac{2k_BT\ln(2)}{mc^2}}. \tag{54}$$

The Voigt profile is a convolution between the inhomogeneous Gaussian g_I and homogeneous Lorentzian g_H line shape functions and is given by (Bernath, 2005, eqn (1.83))

$$g(\nu - \nu_0) = \int g_I(\xi - \nu_0)g_H(\nu - \xi)\, d\xi \tag{55}$$

A useful algorithm for the Voigt profile is found in (Thompson, 1993)

$$V(u, a) = \mathrm{Re}\left[\exp[z^2]\mathrm{erfc}(z)\right] \tag{56}$$

where $z = a + i\,u$, $a = \sqrt{\ln(2)}\frac{\Delta\nu_H}{\Delta\nu_I}$, and $u = 2\sqrt{\ln(2)}\frac{(\nu-\nu_0)}{\Delta\nu_I}$

$$g_V(\nu,\nu_0) = 2\sqrt{\frac{\ln(2)}{\pi}}\frac{1}{\Delta\nu_I}\mathrm{Re}\left[\exp\left[-\left(2\sqrt{\ln(2)}\left(\frac{\nu + i\,\frac{\Delta\nu_H}{2}}{\Delta\nu_I}\right)\right)^2\right]\right]\cdot \\ \mathrm{erfc}\left[-i\left(2\sqrt{\ln(2)}\left(\frac{\nu + i\,\frac{\Delta\nu_H}{2}}{\Delta\nu_I}\right)\right)\right] \quad (57)$$

Each of the six allowed transitions for Cs D_2, are added together, weighted by the relative ground state population assuming Boltzmann population distribution according to

$$f = p_r = \frac{g_r \exp[-\beta E_r]}{\sum_i g_i \exp[-\beta E_i]} \quad (58)$$

resulting in the total absorption cross section.

Any effect that changes the absorption profile will change the group velocity delay through the resonant medium. For example, changing the temperature of the alkali cell varies the cesium concentration in the cell. Attenuation depends on concentration, which directly effects the real index of refraction. Thus varying temperature becomes a knob by which the delay is tunable, albeit a slow-tunable method. Other possible methods of tuning the group velocity in dispersion delay medium include buffer gas pressure or frequency tuning of the pulse across the absorption spectrum. Saturation effects such as SIT and hole burning may also be alternate methods of optical delay tuning.

Wave Propagation and Group Velocity

The defining theoretical work in the propagation of waves comes from the combined works of A. Sommerfeld and L. Brillouin. The definition phase velocity, v_ϕ, and group velocity, v_g, used to describe the velocity of the phase front and propagation a packet as given by Sommerfeld from works originating around 1910, first

published during World War I, and reprinted in complete form in *Wave Propagation and Group Velocity* (Brillouin, 1960) in 1960. Standard definitions for group velocity, signal velocity, and velocity of energy transfer are critically importance and often misunderstood (Born and Wolf, 1999; Jackson, 1999; Chu and Wong, 1982a,b). Brillouin and Sommerfeld opened the possibilities that are disturbing or surprising to many, such as subluminal (slow light), superluminal (fast light) and negative group velocities (Brillouin, 1960). Their work carefully demonstrates that (first) forerunners propagate at velocity c and the signal arrives at the aptly named signal velocity. Signal velocity does not deviate from group velocity except in the region of anomalous dispersion($dn/d\nu < 0$) (Brillouin, 1960, p.78). The signal velocity is always equal to or less than c and Einstein causality is not violated.

The possibility of group velocities that are much greater than c, "or even negative" are outlined in the 1970 work of Garrett and McCumber (Garrett and McCumber, 1970). There is a comment in Brillouin, citing A. Schuster's *Einführung in die theoretische Optik* (Introduction to Theoretical Optics)[Leipzig, 1907], in which he states that "group velocity has meaning only so long as it agrees with the signal velocity...negative parts of the group velocity have no physical meaning". Garrett and McCumber theoretically demonstrate through analytical approximation and numerical analysis, that there remains some physical significance and that the Gaussian pulse is not significantly distorted if the pulse is "spectrally narrow in comparison with the atomic line" (Garrett and McCumber, 1970). An additional article by M. D. Crisp provides theoretical justification in the photon-atom interaction as the cause of the observed group velocity variations in the neighborhood of resonant atomic lines (Crisp, 1971). Crisp states that the shift in the center of gravity (maximum pulse amplitude) is due to the asymmetric absorption or amplification of energy from the light pulse and the pulse will propagate at group velocity despite significant pulse distortion in a dispersive medium (Chu and Wong, 1982a,b).

Another important theoretical pulse propagation publication was printed in 1993, wherein Bolda, Chiao and Garrision prove two theorems for calculating group velocity in dispersive media in the region of atomic resonances (Bolda et al., 1993). The first theorem states that regions of abnormal group velocity, regions where v_g is superluminal, infinite or negative, "are required by the causality arguments that lead to the Kramers-Kronig relations" (Bolda et al., 1993). The second theorem states that information about the abnormal group velocity regions is obtained from the absorption (or gain) curves of the medium (Bolda et al., 1993).

Theoretical description of optical pumping mechanisms and development of the quantum mechanical formalism started with the work of Barrat and Cohen-Tanoudji (Barrat and Cohen-Tannoudji, 1961b,a), as well as Harper and Mathur (Harper and Mathur, 1967). Pulse propagation effects in terms of the density matrix formalism were developed by Mathur, Tang and Harper (Mathur et al., 1970). These works are particularly important to the description of coherent photon-atom interactions such as SIT and EIT.

Slow Light Mechanisms

Previous discussion describe pulse delay in the linear Beer's-law regime. Here pulse delays are the predicted consequence of Maxwell's equations and the Kramers-Kronig relations. There are several other related methods to achieve slow light (or fast light) such as saturation delay, self-induced transparency and electromagnetically-induced transparency. It is possible for these pulse delay mechanisms to be observed simultaneously in certain situations and determination of the cause of the observed delay is often difficult. This section describes the history of slow light research and details the various delay mechanisms.

Linear Dispersion

Linear dispersion delay occurs at pulse intensities well below the saturation intensity. In this region the pulse amplitude transmitted through the absorbing medium follows Beer's law attenuation and the observed pulse delay is not intensity dependent. Historically initial studies in pulse propagation appeared in the context of nonlinear effects primarily self-induced transparency, discussed in a later section, where the observation of linear and nonlinear effects can be blended within a single medium (Khurgin and Tucker, 2009).

Demonstration of optical pulse delay is a direct result of Kramers-Kronig relations and discussed in the theoretical predictions of Garrett and McCumber (Garrett and McCumber, 1970). Initial experiments sought to demonstrate superluminal group velocity in a gain medium. One of the first demonstrations of semi-classical group velocity and the Garret McCumber predictions appear as a measure of pulse velocity greater than the speed of light in vacuum c in a neon absorption cell within a He-Ne laser cavity (Faxvog et al., 1970). Theoretical discussion of these results is reported in a series of works by Casperson and Yariv (Casperson and Yariv, 1970, 1971).

One of the first studies in linear slow light pulse propagation appears in the works of Grischkowsky in 1973 (Grischkowsky, 1973) in relation to earlier reports of SIT (McCall and Hahn, 1967; Faxvog et al., 1970; Slusher and Gibbs, 1972) in that far from resonance pulses can exhibit long linear delays outside the SIT region (Khurgin and Tucker, 2009). Grischkowsky reported difference in delays of circularly polarized light in the Zeeman-split rubidium $^2P_{1/2}$ line (Grischkowsky, 1973). Short pulses of narrow linewidth low-intensity near the resonant line in the dilute alkali vapor were produced group velocities as low as $1/14c$. Grischkowsky contends that most of the energy in the propagating wave was contained in the vapor as coherent atomic excitation and quantitatively explained using adiabatic following, in which "pseudomoments of the

atoms remain aligned along the effective field of the laser" (Grischkowsky, 1973).

Linear dispersion pulse delays as well as advancement (superluminal group velocity) were demonstrated by Chu and Wong (Chu and Wong, 1982a,b) in an epitaxially grown GaP:N crystal. Pulse propagation in dispersion delay gained experimental notoriety when Tanaka *et al.* (Tanaka et al., 2003) documented the observation of negative group delay, or superluminal velocity, in rubidium vapor D_1 transition using "conventional" group velocity.

At the same time Agarwal and Dey proposed a slow light method using linear dispersion delay in a Doppler-broadened saturation spectroscopy system burning a spectral hole in the absorbing medium (Agarwal and Dey, 2003) similar to the EIT-related work in a ruby crystal by Bigelow, Lepeshkin and Boyd (Bigelow et al., 2003).

The next series of significant slow light research came from the Howell group at the University of Rochester, NY. As a much simpler nearly passive alternative to EIT, using the atomic doublet structure (rubidium D_2 transition) as means to control velocity of light through the medium observed in 2006 by Camacho *et al.* (Camacho et al., 2006a). Camacho outlines several desirable criteria for slow light to be used in communication applications. It can be argued that dispersion delay has several advantages over more complex EIT systems. One such potential application was realized with wide-band tunable optical delay using slow light in the two-absorption atomic resonance setup (cesium vapor D_2 transition) by Camacho (Camacho et al., 2007) and all-optical delay (Camacho et al., 2007).

Saturation Delay

For pulse intensities above the linear (Beer's law) region as the intensity is comparable to the saturation intensity a pulse distortion delay effect is apparent. Saturation delay is created as an incoherent delay effect which occurs when the leading edge of the pulse is sufficiently intense such that half of the atoms in a two-level absorber

are excited to the upper level and the absorption line becomes saturated (Allen and Eberly, 1987). The rest of the pulse is then transmitted completely unattenuated as if the absorbing medium were transparent. The pulse appears to undergo delay because the transmitted "center of mass" of the pulse is moved back in time relative to the initial pulse. This is a frequency dependent effect such that saturation intensity is lowest at the absorption feature resonance peak. Saturation delay is necessarily intensity dependent producing pulse distortion and delay that increases to a maximum and decreases with further increase in intensity (Allen and Eberly, 1987). Pulses capable of bleaching the medium are transmitted with little distortion or attenuation.

Self-Induced Transparency

Self-induced transparency (SIT) is a coherent delay effect described theoretically and reported experimentally by McCall and Hahn (McCall and Hahn, 1967, 1969). The SIT delay is attributed to energy leaving the pulse, coherently exciting the atoms of the absorbing medium and energy is coherently redeposited into the trailing edge of the pulse with no loss of signal amplitude. Delay is produced by the temporary storage of the pulse energy in the absorber (Allen and Eberly, 1987).

McCall and Hahn first proposed the theory of self-induced transparency as the coherent coupling of a coherent pulse and dipole moment of the atomic medium and provided experimental results in a series of cooled ruby lasers (McCall and Hahn, 1967). Nonlinear transmission of laser light is observed such that low-intensity pulses are highly attenuated and high-intensity light are transmitted unattenuated, which is very similar to the delay and pulse attenuation results observed with pure incoherent saturation delay. McCall and Hahn introduce the pulse area theorem (McCall and Hahn, 1967, 1969) where the pulse area Θ is a dimensionless parameter defined by

(Fox, 2006)

$$\Theta = \left| \frac{\mu_{12}}{\hbar} \int_{-\infty}^{+\infty} \mathcal{E}_0(t) dt \right|. \tag{59}$$

For pulses of area equal to π is called a π-pulse. An atomic system coherently excited by a π-pulse will have the atoms in the excited state following the pulse, but returned to the ground state following a 2π-pulse (Fox, 2006; Allen and Eberly, 1987). Theoretically for pulse areas above 3π the atoms are coherently excited and deexcited more than once. The resulting pulse breakup is observed for such $n\pi$-pulses by McCall and Hahn (McCall and Hahn, 1967) and is presented as evidence of SIT (Allen and Eberly, 1987).

Patel and Slusher were first to present SIT in a gaseous medium where delays of 0.2 μs were observed in SF_6 (Patel and Slusher, 1967). They also noted pulse shaping effects where the pulse become more symmetric, the pulse tail showed increased intensity, and delay was intensity dependent. The results of the experiment were questioned regarding the degeneracy of SF_6 by Rhodes, Szöke and Javan (Rhodes et al., 1968). Courtens and Szöke demonstrated that in the limit far from the resonsant SIT peak the pulse delay follows linear dispersion theory (Allen and Eberly, 1987; Courtens and Szöke, 1968). Bradley, Gale and Smith reported SIT in potassium vapor (Bradley et al., 1970) using tunable cavity and a streak camera to visualize the resulting pulse delay. In 1972 as a response to previous degeneracy criticism Slusher and Gibbs reported SIT in a rubidium vapor made nondegenerate in a tuned magnetic field (Slusher and Gibbs, 1972) where $n\pi$ pulse breakup appeared in agreement with McCall and Hahn pulse area theory.

Results presented in the present work do not intentionally seek pulse length-intensity combinations which produce pulse area $\Theta = n2\pi$ in which SIT is observed.

Electromagnetically-Induced Transparency

The final slow light mechanism to be discussed is electromagnetically-induced transparency (EIT). In EIT laser-induced coherence between atomic states leads to quantum interference between excitation pathways producing a narrow transmission window at an absorption resonance (Fleischhauer et al., 2005) which has proven as an important slow light (and stored light) mechanism due to the enhanced nonlinear response in the narrow transparency region of steep dispersion. Typical EIT schemes require a three-level atomic system where electronic dipole selection rules dictate that two pairs of the levels are dipole coupled while the third transition is dipole forbidden (Marangos, 1998). Review of EIT systems widely available in the works of Marangos (Marangos, 1998), Fleischhauer, Imamoğlu and Marangos (Fleischhauer et al., 2005), Boyd (Boyd, 2008; Noginov et al., 2009), Boyd and Gauthier (Boyd and Gauthier, 2002), Chiao and Milonni (Chiao and Milonni, 2002) as well as Milonni (Milonni, 2002, 2005).

Harris, Field and Imamoğlu coined the term EIT in 1990 (Harris et al., 1990) theoretically predicting the coherent EIT effect. The following year Boller, Imamoğlu and Harris demonstrated EIT in a Sr heat pipe. In 1999 extreme slow group velocities of $17\,\mathrm{m\,s^{-1}}$ were achieved using EIT in a Bose-Einstein condensate of sodium atoms (Hau et al., 1999; Hau, 2001).

The next milestone experimental measurement of dispersion delay comes in 1995 from the work of Xiao *et al.* (Xiao et al., 1995) using a gas of hot rubidium atoms tuned near the $5S_{1/2} \rightarrow 5P_{3/2}$ in a Mach-Zehnder (MZ) interferometer. They did not directly measure the group velocity, but calculated the velocity via measurement of the phase shift (Boyd and Gauthier, 2002) reaching a group velocity of $c/13.2$ with the coupling laser in a ladder-type EIT system. Also that year Kasapi *et al.* reported Λ-type EIT group velocity of $c/165 \approx 1.817 \times 10^6\,\mathrm{m\,s^{-1}}$ in a ^{208}Pb vapor(Kasapi

et al., 1995).

Alkali-metal vapors have played a central role in EIT slow light research. Zibrov *et al.* (Zibrov et al., 1996) demonstrated enhanced index of refraction without absorption in Rb D_1.

Group velocities as low as $8\,\mathrm{m\,s^{-1}}$ inferred in rubidium experiment in 1999 by Budker *et al.* (Budker et al., 1999). Hot 360 K ^{87}Rb vapors produced group velocities of $90\,\mathrm{m\,s^{-1}}$ (Kash et al., 1999) using a Λ-type EIT scheme.

Also in 2003, Kim *et al.* (Kim et al., 2003) arbitrarily changed the group velocity from subluminal to superluminal by changing the coupling laser intensity, in an EIT-like setup, with v_g from $c/3000$ to $-c/14400$. At this point, experiments focused primarily on the measurement of pulse propagation phenomena in the vicinity of a single resonant absorption line.

In a 2007 analytical paper, Shi *et al.* (Shi et al., 2007) explored theoretical use of dispersion delay systems in MZ interferometer system with slow light cell, allowing for tunable optical path length (OPL) in MZ system. Citing recent experimental results, Shi compared possible SL interferometry applications (Shi et al., 2007).

It has been demonstrated by Vudyasetu (Vudyasetu et al., 2008) that transverse images can be slowed and even stored with little loss of coherence. The Howell group again displayed tunable delay of the image using temperature variation in rubidium vapor dispersion delay cell as well as using pump/probe means to control the absorption and group delay.

Following the University of Rochester work, analytic study of dispersion delay and limitations Shakhmuratov and Odeurs (Shakhmuratov and Odeurs, 2008) refer to Camacho (Camacho et al., 2006a) for criteria to use dispersion delay in communication application. Shakhmuratov cites low group velocity without (EIT) driving fields for low-frequency coherence.

Just as linear dispersion, saturation delay and SIT can appear in a single sys-

tem, theoretical description of a combined SIT and EIT system. Scully *et al.* report theoretical analysis of SIT as a coupling field in a V-type EIT system called "mixed induced transparency" (MIT) (Scully et al., 2001).

Electromagnetically-induced transparency is typically evident in systems where the Rabi frequency Ω_R (Loudon, 2000)

$$\Omega_R \equiv |\, \mu_{12}\mathcal{E}_0\hbar \,| \gg \gamma \tag{60}$$

is much greater than the homogeneous broadening γ (Boyd and Gauthier, 2002). In the present work pump intensities are such that EIT was not observed.

Scope of research

This work seeks to develop a linear dispersion pulse delay prediction from a full-frequency hyperfine structure model with Doppler-broadened Voigt profile lineshape in cesium and rubidium. This pulse delay model will compared to observed pulse delay and non-Voigt double-Lorentzian approximation model predictions.

Once a reliable Doppler-broadened model has been developed, modification of the absorption profile will be attempted using a second laser to depopulate the ground state and observe delays in a narrow spectral hole in the absorption profile in a modified sub-Doppler spectroscopy system.

Finally complete theoretical description of the system is still being developed in order to optimize the lasers for scaling to high output power. Optimization of a DPAL system depends on accurate pressure-broadening models to properly match the atomic absorption profile to the broadband diode pump source. There is currently no validated bleach wave model of an operating DPAL system. Transverse absorption spectroscopy setup is used in this work to partially examine the temporal dynamics of the bleached wave of a pulsed alkali-metal vapor system.

III. Kramers-Kronig Delay Calculation

This chapter originally appeared in SPIE Advances in Slow and Fast Light III

(Anderson and Perram, 2010b).

In this manuscript predicted delay is developed for a pulse propagating through an atomic vapor. Theoretical description for pulse delay is developed from atomic absorption coefficient with hyperfine structure and Voigt lineshape. Predicted delays are in agreement with observed delays in a cesium vapor cell at various temperatures between 78.9 °C *and* 137.2 °C.

Introduction

A number of applications have been conceived for light with slow group velocities, including optical delay lines, interferometry for remote sensing, and quantum information. Electromagnetically induced transparency (EIT) is a well understood method often used to produce slow light (Marangos, 1998; Milonni, 2005; Fleischhauer et al., 2005). Alternatively optical delays in the vicinity of atomic resonance transitions have also been demonstrated (Grischkowsky, 1973; Tanaka et al., 2003; Agarwal and Dey, 2003; Camacho et al., 2006a). One of the early slow light experiments demonstrated group velocities of $c/14$ using Zeeman splitting of the D_1 line of rubidium (Grischkowsky, 1973). Agarwal and Dey used an absorption spectroscopy setup to observe delay (Agarwal and Dey, 2003). More recently, all-optical delays of many times the pulse width have been demonstrated in the double Lorentzian structure of hot alkali vapors (Camacho et al., 2007) where delays of 1.6 GHz-bandwidth pulse by 25 pulse widths, or 7 ns, have also been observed using the hyperfine structure of the Cs D_2 line. Delays of up to 106 ns have been achieved using the hyperfine splitting of the D_2 lines in ^{85}Rb by tuning the temperature of four 10 cm cells to 140 °C (Camacho et al., 2006a). Indeed, double Lorentzian systems provide large bandwidth, large

delays, and minimal absorption and dispersion. Rapid tuning of the delays has also been demonstrated by varying the modulation frequency in a two-laser, pump-probe configuration (Camacho et al., 2006b).

Precise absorption models which fully account for the hyperfine structure can be computationally expensive. Therefore it is often advantageous to approximate the absorption coefficient or complex index of refraction as the summation of Lorentzian lineshapes at a pair of resonant frequencies. Lorentzian absorption lineshapes provide adequate predictions for cases with homogeneous broadening or when the laser is detuned from resonance by an order of magnitude greater then the inhomogeneous linewidth (Camacho et al., 2007). At moderate temperatures (above 100 °C) the Doppler linewidth for the cesium D_2 line approaches 0.5 GHz establishing a significant limit on applicability such that Doppler-broadened lineshapes should be considered. Furthermore, tuning of the delays by varying laser frequency is largely unstudied. In the present work we develop an absorption model, calculate predicted pulse delay and compare delay measurements to predicted delays. Experimental results are in agreement with prediction models using a Voigt lineshape approximation of the broadened absorption with full D_2 hyperfine structure.

Absorption Coefficient

Frequency dependent variations in the index of refraction near resonant absorption transitions give rise to dramatic changes in group velocity. Index of refraction is related to the absorption coefficient. When absorption is known through measurement or calculation, delay can be predicted. A rapid accurate numerical absorption model may prove useful for applications needing pulse delay predictions over a wide frequency range in the neighborhood of resonant atomic transitions.

The absorption is a function of frequency ν as well as temperature T. Frequency

dependence is fundamental to photon-atom interaction in that probability of absorption. Temperature dependence arises from both Doppler broadening and temperature dependent number density of the atomic vapor.

We seek the absorption coefficient from the usual definition of absorbance

$$A_\lambda = -\ln(I/I_0) = \alpha(\nu, T)l = \sigma_{tot}(\nu, T)n(T)l \tag{61}$$

where l is the cell length, α is absorption coefficient, σ is the cross section, and n is the number density. To predict the pulse delay due to absorption, the absorption coefficient $\alpha(\nu, T) = \sigma_{tot}(\nu, T)n(T)$ must be determined.

The total nuclear angular momentum I for cesium is 7/2. For each hyperfine energy level, the total atomic angular momentum, $\mathbf{F}$, is given by $\mathbf{F} = \mathbf{J} + \mathbf{I}$, whose magnitude takes on the values, $|J - I| \leqslant F \leqslant |J + I|$. Transitions follow the selection rule $\Delta F = \pm 1, 0$. In this paper the notation used for the D_2 absorption transitions follows spectroscopy notation $F'' \rightarrow F'$, where F'' refers a hyperfine level from the ground state $S_{1/2}$ and F' refers to a hyperfine level in the $P_{3/2}$ level.

The cross section σ for a single hyperfine transition can be calculated using

$$\sigma_{F''F'}(\nu, T) = \frac{2\pi^2}{3\epsilon_0 hc}\,\mu^2_{F''F'}\,\nu\,g(\nu - \nu_{F''F'}) \tag{62}$$

where $\mu^2_{F''F'}$ is the transition dipole moment such that

$$\mu^2_{F''F'} = S_{F''F'}\,|\,\langle J''\,||\,e\,\mathbf{r}\,||\,J'\rangle\,|^2 = S_{F''F'}\,e^2 D^2_{J''J'}. \tag{63}$$

The lineshape function $g(\nu - \nu_0)$ is discussed later in this paper.

Strength of the photon-atom interaction is characterized by the dipole matrix elements. Relative strength of each transition can be expressed as a reduced matrix element and a relative strength factor, Wigner 6-j symbol, for each $F'' \rightarrow F'$ transition

such that

$$S_{F''F'} = (2F'+1)(2J''+1)\begin{Bmatrix} J'' & J' & 1 \\ F' & F'' & I \end{Bmatrix}^2 \tag{64}$$

The relative strength factor $S_{F''F'}$ follows the summation rule $\sum_{F'} S_{F''F'} = 1$. The frequency for each hyperfine $F'' \rightarrow F'$ transition is calculated (Arimondo et al., 1977; Gerginov et al., 2003). Cesium D_2 properties are summarized in Table 1.

Table 1. Summary of hyperfine transition frequencies and relative line strengths cesium D_2.

Transition $F'' \rightarrow F'$	$\nu_{0_{F''F'}}$ * (MHz)	Strength Factor $S_{F''F'}$
$3 \rightarrow 2$	4831.14	5/14
$3 \rightarrow 3$	4982.37	3/8
$3 \rightarrow 4$	5183.65	15/56
$4 \rightarrow 3$	-4210.26	7/72
$4 \rightarrow 4$	-4008.98	7/24
$4 \rightarrow 5$	-3757.89	11/18

* Calculated from references (Arimondo et al., 1977; Gerginov et al., 2003)

In solving for the transition dipole moment (Loudon, 2000),

$$\frac{1}{\tau} = \frac{\omega_0^3}{3\pi\epsilon_0\hbar c^3}\frac{g_{J''}}{g_{J'}}e^2 D_{J''J'}^2 \tag{65}$$

where g_i the J degeneracy such that $g_i = 2J_i + 1$, so that

$$\mu_{F''F'}^2 = \frac{3\epsilon_0 h c^3}{16\pi^3\nu_0^3}\left(\frac{2J'+1}{2J''+1}\right)S_{F''F'}\frac{1}{\tau}. \tag{66}$$

Combining Equation (62) and Equation (66) the cross section can be calculated

$$\sigma_{F''F'}(\nu, T) = \frac{c^2}{8\pi}\frac{\nu}{\nu_0^3}\left(\frac{2J'+1}{2J''+1}\right)S_{F''F'}\frac{1}{\tau}g(\nu - \nu_0) \tag{67}$$

For the cesium D_2 transitions, $J'' = 1/2$ and $J' = 3/2$ so that Equation (67) can be

simplified to

$$\sigma_{F''F'}(\nu, T) = S_{F''F'} \frac{1}{\tau} \frac{c^2}{4\pi} \frac{\nu}{\nu_0^3} g(\nu - \nu_0) \tag{68}$$

The relative ground state population must also be considered when calculating absorption for each hyperfine $F'' \rightarrow F'$. Assuming the $S_{1/2}$ population follows a Boltzmann distribution as a function of temperature and the ground state hyperfine energies, the relative population is given by

$$f_{F''} = \frac{g_{F''} e^{-\beta E_{F''}}}{\sum_i g_i e^{\beta E_i}} \tag{69}$$

where $\beta = 1/k_B T$ and k_B is the Boltzmann constant. The total absorption cross section σ_{tot} is the sum each $F'' \rightarrow F'$ cross section.

$$\sigma_{tot}(\nu, T) = \sum_{F'', F'} f_{F''} \, S_{F''F'} \frac{1}{\tau} \frac{c^2}{4\pi} \frac{\nu}{\nu_0^3} g(\nu - \nu_0) \tag{70}$$

Lorentzian lineshapes are often used to approximate atomic transitions for Doppler-free spectroscopic techniques. Close to the absorption peaks or when inhomogeneous broadening effects are considerable, a Voigt profile should be used for more accurate depiction of the atomic absorption. Thus the lineshape itself is both frequency and temperature dependent. The Voigt profile is a convolution of both homogeneous and inhomogeneous broadening lineshapes, such that

$$g_V(\nu - \nu_0) = \int_{-\infty}^{\infty} g_I(\nu_0' - \nu_0) g_H(\nu - \nu_0') d\nu_0' \tag{71}$$

where $g_I(\nu_0' - \nu_0)$ is the inhomogeneous lineshape and $g_H(\nu - \nu_0')$ is the homogeneous

lineshape given by the formulas (Bernath, 2005)

$$g_I(\nu - \nu_0) = \frac{2}{\Delta\nu_G}\sqrt{\frac{\ln(2)}{\pi}}\exp\left[-4\ln 2\left(\frac{\nu-\nu_0}{\Delta\nu_G}\right)^2\right] \tag{72}$$

$$g_H(\nu - \nu_0) = \frac{\Delta\nu_H/2\pi}{(\Delta\nu_H/2)^2 + (\nu-\nu_0)^2} \tag{73}$$

in terms of the Gaussian (inhomogeneous) full width at half maximum (FWHM) $\Delta\nu_G$ and the Lorentzian (homogeneous) FWHM $\Delta\nu_L$.

A useful algorithm for the Voigt lineshape (Thompson, 1993) is

$$V(u,a) = \mathrm{Re}\left[\exp(z^2)\mathrm{erfc}(z)\right] \tag{74}$$

where

$$z = a + iu \tag{75}$$

$$a = \sqrt{\ln 2}\frac{\Delta\nu_L}{\Delta\nu_G} \tag{76}$$

$$u = 2\sqrt{\ln 2}\frac{(\nu-\nu_0)}{\Delta\nu_G}. \tag{77}$$

Three broadening mechanisms were included in this model, Doppler broadening, lifetime broadening and buffer gas effects. Lifetime, or natural broadening, and buffer gas effects are homogeneous broadening effects. Doppler broadening comes from the Maxwell-Boltzmann velocity distribution as a function of the temperature T and the atomic mass M. The Doppler FWHM is given by the formula

$$\Delta\nu_G = \nu_0\left(\frac{8k_BT\ln 2}{Mc^2}\right)^{1/2}. \tag{78}$$

Homogeneous broadening from natural broadening and pressure broadening is given

by the formula

$$\Delta\nu_H = \frac{1}{2\pi}\left(\frac{1}{\tau_r}\right) + \sum_i \gamma_i \left(\frac{T_{sys}}{T_{data}}\right)^{1/2} P_i \tag{79}$$

where γ_i is the pressure broadening constant and P_i is the pressure for each buffer gas species. The pressure broadening constants are temperature dependent and are scaled by the temperature of the system T_{sys} and the temperature at which the values were measured T_{data}. Buffer gases can both broaden the lineshape profile and cause a frequency shift as a function of buffer gas pressure. Included in the alkali models are helium, neon, nitrogen and ethane (Rotondaro and Perram, 1997). For simplicity model predictions and data are shown without pressure broadened lineshapes so that the only source of homogeneous broadening is natural broadening.

Vapor pressure equations for cesium used in this model are given by the "precise equations" from Alcock *et al.* (Alcock et al., 1984). In general the vapor pressure is an exponential function $P_V(T)$. Assuming the alkali vapor acts as an ideal gas we can determine the number density

$$PV = Nk_BT \rightarrow n(T) = \frac{P_v(T)}{k_BT} \tag{80}$$

The model calculated absorption coefficient plots are shown in Figure 2 for 78.9 °C, 102.5 °C and 137.2 °C.

Predicted Delay

Once the absorption coefficient is known the predicted delay for a pulse propagating through the alkali medium is determined. The absorption coefficient is related to the imaginary part of the complex index of refraction $n = n_R + in_I$, by the equation

$$n_I = \frac{c}{4\pi\nu}\alpha(\nu). \tag{81}$$

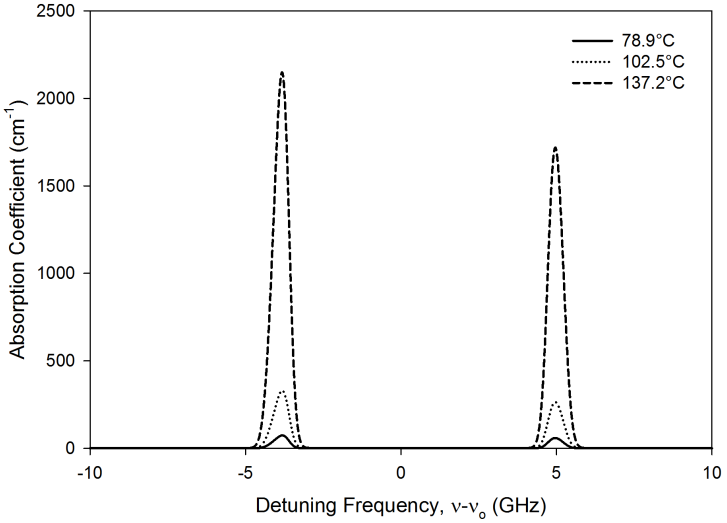

Figure 2. Simulation output for cesium D_2 absorption coefficient (cm^{-1}) at various cell temperatures detuned ± 10 GHz from the central D_2 transition frequency 351.7257185 THz.

Using the familiar Kramers-Kronig relations

$$\mathrm{Re}\left[\epsilon_r(\nu)\right] = 1 + \frac{2}{\pi}\,\mathrm{P}\int_0^\infty \frac{\xi\ \mathrm{Im}\left[\epsilon_r(\xi)\right]}{\xi^2 - \nu^2} d\xi \tag{82}$$

$$\mathrm{Im}\left[\epsilon_r(\nu)\right] = -\frac{2\nu}{\pi}\,\mathrm{P}\int_0^\infty \frac{\mathrm{Re}\left[\epsilon_r(\xi)\right] - 1}{\xi^2 - \nu^2} d\xi \tag{83}$$

we can connect the complex index of refraction or the absorption coefficient to the real index of refraction. The symbol P represents the Cauchy principal value of the integral. Combining Equation 81 and Equation 82 yields an expression for the real index of refraction in terms of the absorption coefficient

$$n_{_R}(\nu) = 1 + \frac{c}{2\pi^2}\,\mathrm{P}\int_0^\infty \frac{\alpha(\xi)}{\xi^2 - \nu^2} d\xi. \tag{84}$$

The calculated real index of refraction for Cs D_2 is shown in Figure 3.

The group velocity shown in Figure 4 is found from the real index of refraction

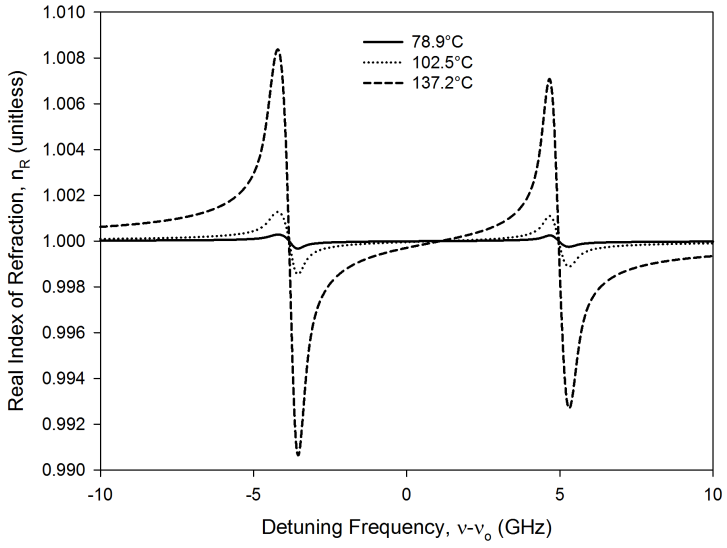

Figure 3. Calculated real index of refraction for cesium D_2 at various cell temperatures detuned ±10 GHz from the central D_2 transition frequency.

with the equation,

$$v_g = \frac{c}{n_R + \nu \frac{dn_R}{d\nu}}. \tag{85}$$

Time for the pulse to transit the alkali cell is calculated by $t = l/v_g$ and shown in Figure 5 for a 5 cm alkali cell.

Delay of a signal through the cell is determined by comparing the transit time of a signal frequency near the absorption features with transit time of a signal far detuned from the peaks. The lead FWHM point on the temporal pulse is used as a reference point for determining delay. Tunable delays are achieved by selecting various signal frequencies across the absorption spectrum. Near the absorption peaks pulses realize the greatest group delay.

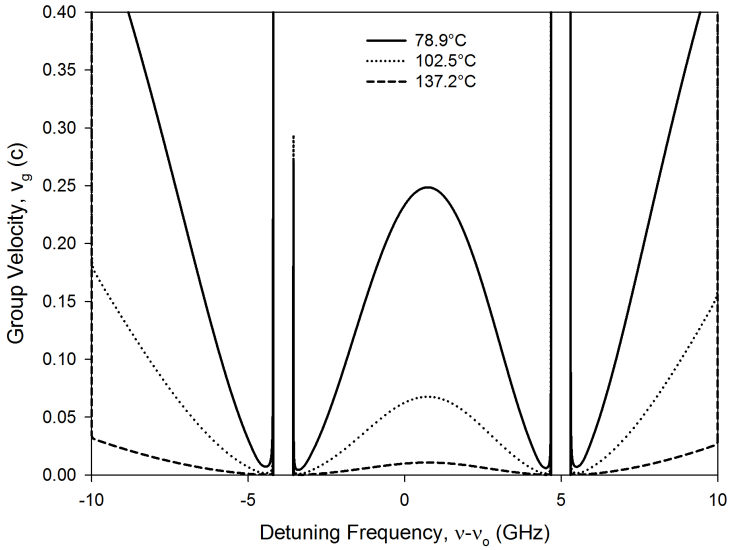

Figure 4. Calculated group velocity (units of c) for cesium D_2 at various cell temperatures detuned $\pm$10 GHz from the central D_2 transition frequency.

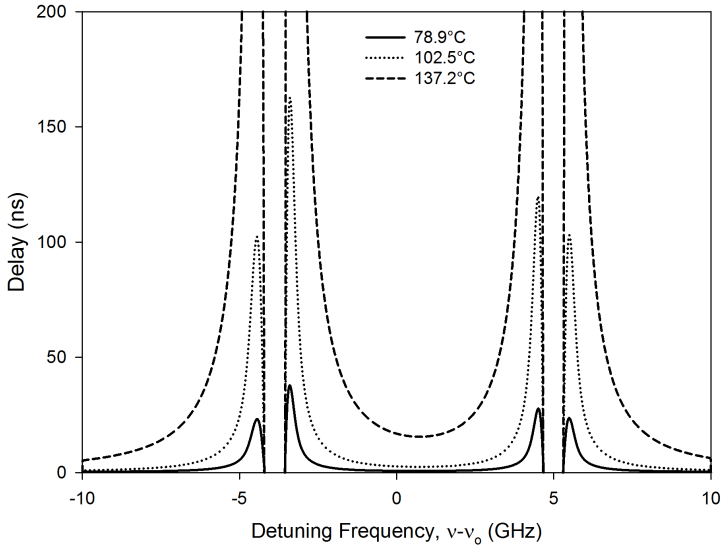

Figure 5. Calculated delay (ns) for cesium D_2 at various cell temperatures detuned $\pm$10 GHz from the central D_2 transition frequency.

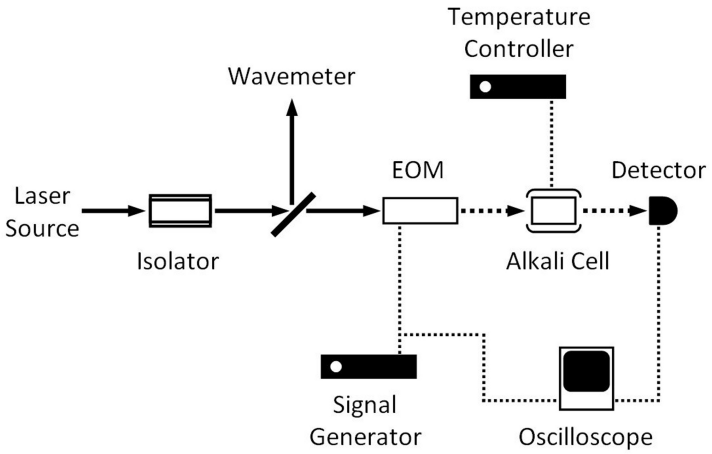

Figure 6. Experimental setup for delay measurements.

Experimental Setup

The experimental apparatus for delay measurements shown in Figure 6 is similar to the absorption spectroscopy setup of Agarwal and Dey (Agarwal and Dey, 2003).

A 25 mW tunable diode laser with less than 300 kHz linewidth is tuned across the Cs D_2 transition. The 1.5 mm diameter laser beam is directed through an optical isolator and a pellicle beam splitter to a fiber coupled Mach-Zehnder interferometric lithium niobate ($LiNbO_3$) electro-optic intensity modulator (EOM). A pulse signal generator drives the EOM to create a 10 ns FWHM pulse with 1 kHz repetition rate.

Part of the beam is sent to a Bristol wavemeter with $0.003\,\mathrm{cm}^{-1}$ accuracy for frequency reference. The modulated pulse propagates through a 5 cm long, low-pressure alkali cell enclosed in a machined aluminum heater block maintained at a constant temperature between 78.9 °C to 137.2 °C using a temperature controller system.

The pulse delay is monitored by a silicon photodiode detector with a 1 ns response time. At a fixed alkali temperature, the laser source is tuned across the cesium D_2 spectrum. At each sample frequency the recorded time-dependent pulse is a

15 s average. This was repeated for approximately 90 frequencies ±25 GHz from the central D_2 frequency.

Results

Pulse delay data were recorded in the range from $T = 78.9\,^{\circ}\mathrm{C}$ to $137.2\,^{\circ}\mathrm{C}$. The delay increases and transmitted intensity decreases at the resonant frequencies and the hyperfine splitting of the ground ${}^2S_{1/2}(F'' = 3 \text{ and } 4)$ levels is clearly evident. At the two peaks of the absorption feature, the transmitted pulse intensities were less than five standard deviations (arbitrary limit) above the background, making accurate determination of the delay difficult. Indeed, the optical depth at line center of the transitions originating from $F'' = 3$ at $T = 114\,^{\circ}\mathrm{C}$ is $\ell = 1/\sigma(\nu_0)n = 0.02\,\mathrm{mm}$. Delays were defined by the leading edge at half the peak intensity.

Pulse delay predicted with this model and measured pulse delays are shown in Figure 7. Predicted delays closely match calculations from the absorption model described previously in this manuscript.

The delays are tuned from 0 ns to 30 ns, up to 3 pulse widths in a single pass through a 5 cm cell, for the $T = 114.0\,^{\circ}\mathrm{C}$ data. The present results compare favorably with the previously observed delay of about 7 ns at zero detuning in a 10 cm cell at 120 °C (Camacho et al., 2007).

Conclusion

Tunable slow light delays are demonstrated through frequency modulation across the hyperfine doublet structure of an alkali metal vapor. Delays of 0 ns to 37 ns have been observed in a single pass through a 5 cm cesium cell at 137.2 °C by detuning from resonance ±25 GHz. Predicted delays closely match calculations from an absorption profile model including Voigt lineshapes and full hyperfine structure. Frequency

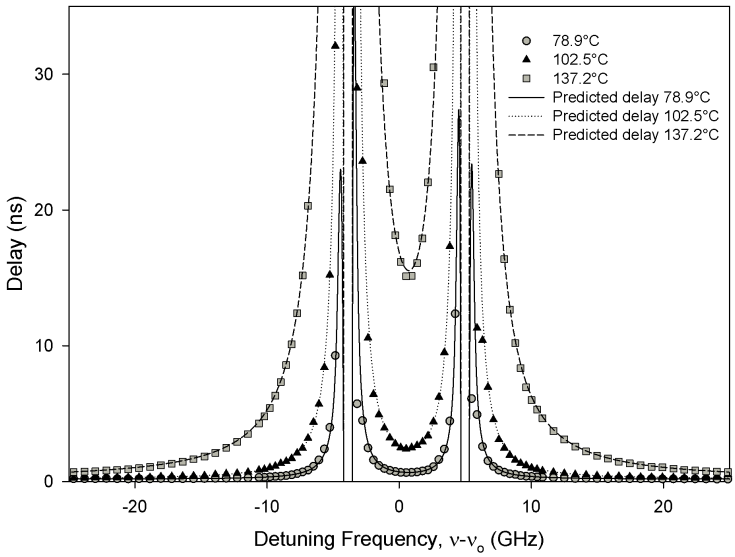

Figure 7. Pulse delay measurements in 5-cm cesium cell at 78.9 °C, 102.5 °C and 137.2 °C with predicted delay calculated from simulation output.

dependence of the delays are sensitive to vapor pressure and Doppler broadening, constraining vapor temperature uncertainties to about 0.1 °C.

IV. Delay Prediction

This chapter originally appeared in Physical Review A 81(3)033842 (Anderson and Perram, 2010a).

The frequency dependence of optical delays in both the wings and core of the cesium D_2 transition have been observed and modeled with a Voigt lineshape convolved with the six hyperfine components. Tunable delays of 0-37 ns are achieved by tuning the laser frequency through resonance at various vapor pressures of 0.15-5.28 mTorr.

Introduction

A number of applications have been envisioned for light with slow group velocities, including optical delay lines, interferometry for remote sensing, and quantum information. Electromagnetically induced transparency (EIT) is often used to produce slow light (Fleischhauer et al., 2005). However, optical delays in the vicinity of atomic resonance transitions have also been demonstrated (Tanaka et al., 2003; Grischkowsky, 1973; Camacho et al., 2006a). One of the early slow light experiments demonstrated group velocities of $c/14$ using Zeeman splitting of the D_1 line of rubidium (Grischkowsky, 1973). More recently, all-optical delays of many times the pulse width have been demonstrated in the double Lorentzian structure of hot alkali vapors (Camacho et al., 2007). Delays of up to 106 ns have been achieved using the hyperfine splitting of the D_2 lines in ^{85}Rb by tuning the temperature of four 10-cm cells to 140 °C. Delays of 1.6-GHz-bandwidth pulse by 25 pulse widths, or 7 ns, have also been observed using the hyperfine structure of the Cs D_2 line. Indeed, the double Lorentzian systems provide large bandwidth, large delays, and minimal absorption and dispersion. A more rapid tuning of the delays has also been demonstrated by

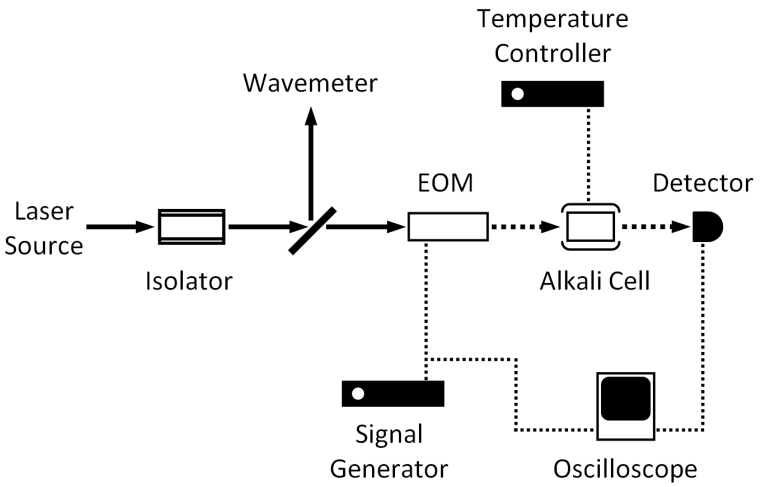

Figure 8. Experimental setup for delay measurements.

varying the modulation frequency in a two laser, pump-probe configuration (Camacho et al., 2006b).

Previous work approximates the complex index of refraction as the summation of Lorentzian lineshapes at a pair of resonant frequencies. Lorentzian absorption lineshapes provide adequate predictions for cases with homogeneous broadening or when the laser is detuned from resonance by an order of magnitude greater then the inhomogeneous linewidth (Camacho et al., 2007). At moderate temperatures the Doppler linewidth for the cesium D_2 line is almost 0.5 GHz establishing a significant limit on applicability. Furthermore, tuning of the delays by varying laser frequency is largely unstudied. In the present work we report on delay measurements across the resonances and show the results are in agreement with Voigt lineshapes including the full hyperfine structure.

Experimental Setup

The experimental apparatus for delay measurements is shown in Figure 6.

A 20-mW tunable diode laser with less than 300 kHz linewidth is tuned across the Cs D_2 transition. The 1.5-mm diameter laser beam is directed through an optical

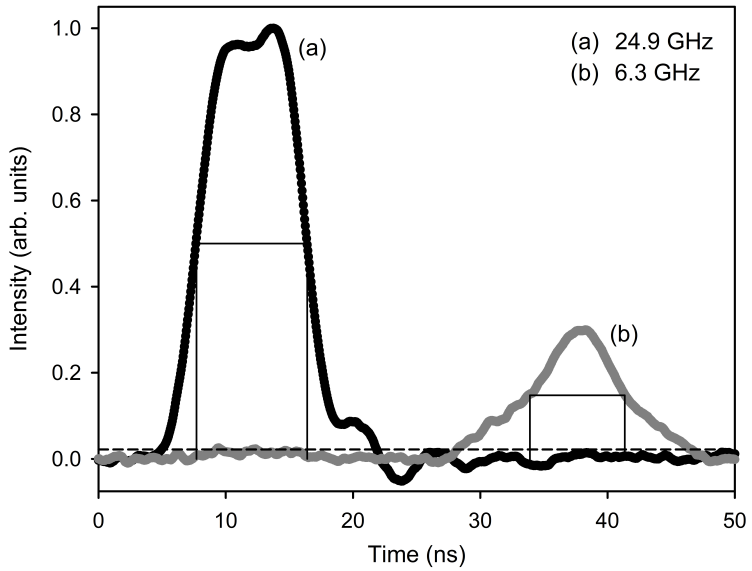

Figure 9. Amplitude modulated 10-ns FWHM laser pulses transmitted through a 5-cm Cs cell at 114.0 °C (a) detuned by 24.9 GHz and (b) detuned by 6.3 GHz. The FWHM for each pulse (solid lines) and pre-trigger noise levels (dashed line) are illustrated.

isolator and a pellicle beam splitter to a fiber coupled Mach-Zehnder interferometric lithium niobate ($LiNbO_3$) electro-optic intensity modulator. A pulse signal generator drives the amplitude modulator to create a 10 ns full-width half maximum (FWHM) pulse with 1 kHz repetition rate as shown in Figure 9.

Part of the beam is sent to a wavemeter with $0.003\,\mathrm{cm}^{-1}$ accuracy for frequency reference. The modulated pulse propagates through a 5-cm-long, low-pressure alkali cell enclosed in a machined aluminum heater block maintained at a constant temperature between 78.9 °C to 137.2 °C using a temperature controller system.

The pulse delay is monitored by a silicon photodiode detector with a 1 ns response time. At a fixed alkali temperature, the laser source is tuned across the cesium D_2 spectrum. At each sample frequency the recorded time-dependent pulse is a 15 s average. This was repeated for approximately 90 frequencies ±25GHz from the central D_2 frequency.

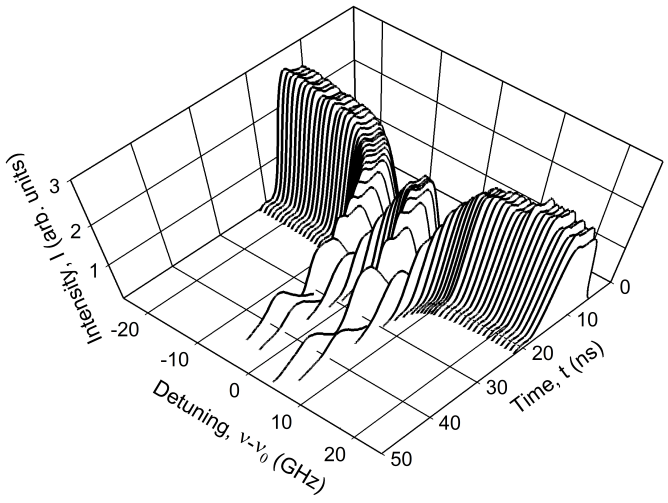

Figure 10. Frequency dependence of transmitted pulses delays through 114.0 °C 5-cm cesium cell.

Results

The observed transmitted pulses for a series of laser wavelengths at $T = 114.0\,^{\circ}\mathrm{C}$ are illustrated in Figure 10. Similar data were recorded at $T = 78.9\,^{\circ}\mathrm{C}$ to $137.2\,^{\circ}\mathrm{C}$. The delay increases and transmitted intensity decreases at the resonant frequencies and the hyperfine splitting of the ground ${}^2S_{1/2}(F'' = 3 \text{ and } 4)$ levels is clearly evident. At the two peaks of the absorption feature, the transmitted pulse intensities were less than five standard deviations above the background, making accurate determination of the delay difficult. Indeed, the optical depth at line center of the transitions originating from $F'' = 3$ at $T = 114\,^{\circ}\mathrm{C}$ is $\ell = 1/\sigma(\nu_0)n = 0.02\,\mathrm{mm}$. Delays were defined by the leading edge at half the peak intensity and are illustrated for $T = 78.9\,^{\circ}\mathrm{C}$ and $114.0\,^{\circ}\mathrm{C}$ in Figure 11.

The delays are tuned from 0 ns to 30 ns, up to 3 pulse widths in a single pass through a 5 cm cell, for the $T = 114.0\,^{\circ}\mathrm{C}$ data. The present results compare favorably with the previously observed delay of about 7 ns at zero detuning in a 10-cm cell at

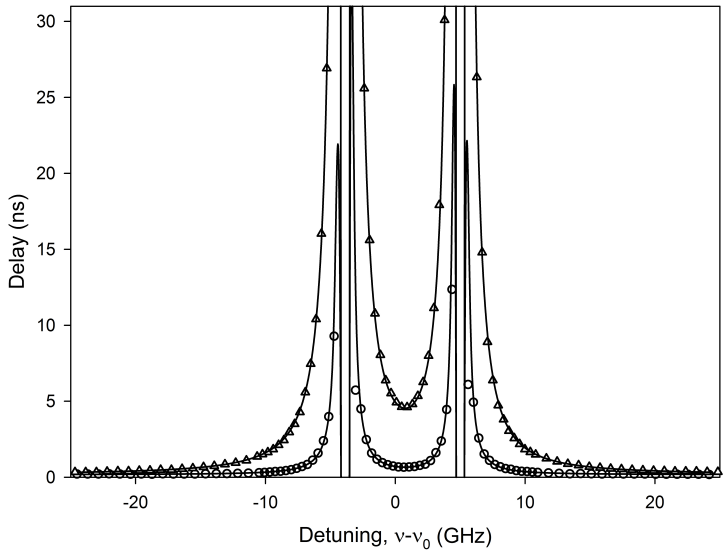

Figure 11. Cesium D_2 delay data for 78.9 °C (open circles) and 114.0 °C (open triangles). Predicted delays (solid lines) are calculated using the full spectrum hyperfine structure absorption model. Maximum error in the delay measurement is ±0.15 ns while the average error is ±0.03 ns.

120 °C (Camacho et al., 2007).

The pulse delays are directly related to the absorption spectrum. Figure 12 illustrates a diode laser absorption spectrum of the Cs D_2 hyperfine split line at low pressure.

The absorption is readily computed from the hyperfine splittings, line strengths, and broadened lineshape (Pitz and Perram, 2008). The absorbance A at a given cell temperature T and length l is related to the effective absorption cross section σ and number density n by

$$A = -\ln(I/I_0) = \alpha(\nu, T)l = \sigma_{tot}(\nu, T)n(T)l \tag{86}$$

where each of the six hyperfine components, $F'' = 3 - 4$ and $F' = 2 - 5$, contributes

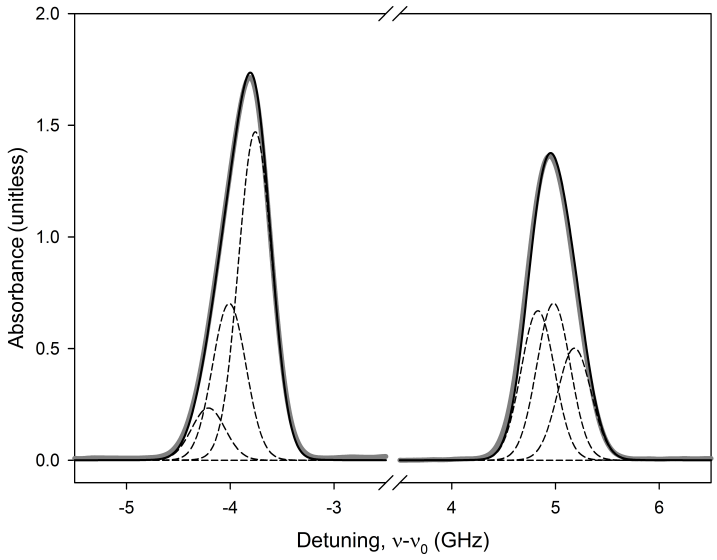

Figure 12. Cesium D_2 absorbance for a 2-cm cesium cell at 25 °C at low pressure (gray line), model prediction for total absorbance (solid black line), and model-simulated absorbance for individual hyperfine transitions (dashed black lines).

to the cross section such that

$$\sigma_{tot} = \sum_{F'',F'} f_{F''} S_{F''F'} \frac{1}{\tau} \frac{c^2}{4\pi} \frac{\nu}{{\nu_0}_{F''F'}{}^3} g_V(\nu - \nu_{0_{F''F'}}). \tag{87}$$

The frequencies $\nu_{0_{F''F'}}$ and the line strengths $S_{F''F'}$ of each hyperfine component are summarized in Table 2.

Radiative lifetime for the Cs D_2 line is $\tau = 30.32(5)$ ns (Amini and Gould, 2003). The statistical distribution of the populations in the two hyperfine split $6^2S_{1/2}$ levels is

$$f_{F''} = \frac{(2F''+1)e^{-\frac{\Delta E}{kT}}}{7 + 9e^{-\frac{\Delta E}{kT}}} \tag{88}$$

where k is Boltzmann's constant and $\Delta E = 9.192\,631\,770$ GHz is the energy difference of the hyperfine levels of the Cs $6\,^2S_{1/2}$ ground state.

The Voigt profile $g_V(\nu - \nu_0)$ is a convolution of both homogeneous and inhomo-

Table 2. Summary of cesium D_2 hyperfine transition frequencies and relative line strengths.

Transition $F'' \rightarrow F'$	$\nu_{0_{F''F'}}$ † (MHz)	Strength Factor $S_{F''F'}$
$3 \rightarrow 2$	4831.14	5/14
$3 \rightarrow 3$	4982.37	3/8
$3 \rightarrow 4$	5183.65	15/56
$4 \rightarrow 3$	-4210.26	7/72
$4 \rightarrow 4$	-4008.98	7/24
$4 \rightarrow 5$	-3757.89	11/18

†Calculated from references (Arimondo et al., 1977; Gerginov et al., 2003)

geneous broadening lineshapes and is approximated by (Thompson, 1993)

$$g_V(u,a) = \mathrm{Re}[\exp(z^2)\mathrm{erfc}(z)] \tag{89}$$

where

$$z = a + iu \tag{90}$$

$$a = \sqrt{\ln 2}\,\frac{\Delta\nu_H}{\Delta\nu_D} \tag{91}$$

$$u = 2\sqrt{\ln 2}\,\frac{(\nu-\nu_0)^2}{\Delta\nu_D} \tag{92}$$

The inhomogeneous Doppler width, $\Delta\nu_D \approx 0.43\,\mathrm{GHz}$ at 114 °C, is relatively large compared to the homogeneous broadening. The cell contains no buffer gas and the alkali pressure is low, so that the homogeneous broadening approaches the natural limit of $\Delta\nu_H = 5.2\,\mathrm{MHz}$.

The temperature dependence of the cesium vapor pressures P are derived from Alcock *et al.* (Alcock et al., 1984) and the corresponding concentrations $n = P/kT$ range from 4.08×10^{12} to 1.24×10^{14} atoms/cm^3 for $T = 78.9\,°\mathrm{C}$ to $137.2\,°\mathrm{C}$. The modeled absorption from Equations (86) and (87) compares very well with the ob-

served spectrum, as illustrated in Figure 12. The only adjustable parameter employed is a small correction to the thermocouple temperatures. The reported temperatures are determined by matching the observed and predicted absorption or delays. For example, the thermocouple temperatures were taken at a position not touching the heater element, in contact with only the alkali cell and exposed to room temperature air within the laboratory. For data reported at 114 °C, thermocouples read 113.7 °C and hyperfine model temperature was adjusted until the observed delay best fit model predicted values within 0.1 °C. The hyperfine splitting of the excited state is smaller than the Doppler width as shown in Figure 12.

The delays are readily predicted from the absorption coefficient by employing the Kramers-Kronig relationship between the real and imaginary portions of the index of refraction $n = n_R + in_I$,

$$n_R = 1 + \frac{1}{2\pi} \mathrm{P} \int_0^\infty \frac{\xi n_I(\xi)}{\xi^2 - \nu^2} d\xi \tag{93}$$

where P represents the Cauchy principal value of the integral. The absorption is related to the imaginary part of the index

$$\alpha(\nu) = \frac{4\pi}{c} \nu \, n_I(\nu). \tag{94}$$

Thus the real portion of the index is related to Equations (86) and (87) by

$$n_R = 1 + \frac{c}{2\pi^2} \mathrm{P} \int_0^\infty \frac{\alpha(\xi)}{\xi^2 - \nu^2} d\xi. \tag{95}$$

Finally, the observed delays are predicted as $t_d = l/v_g$, where the group velocity is defined as

$$v_g = \frac{c}{n_R + \nu \frac{dn_R}{d\nu}}. \tag{96}$$

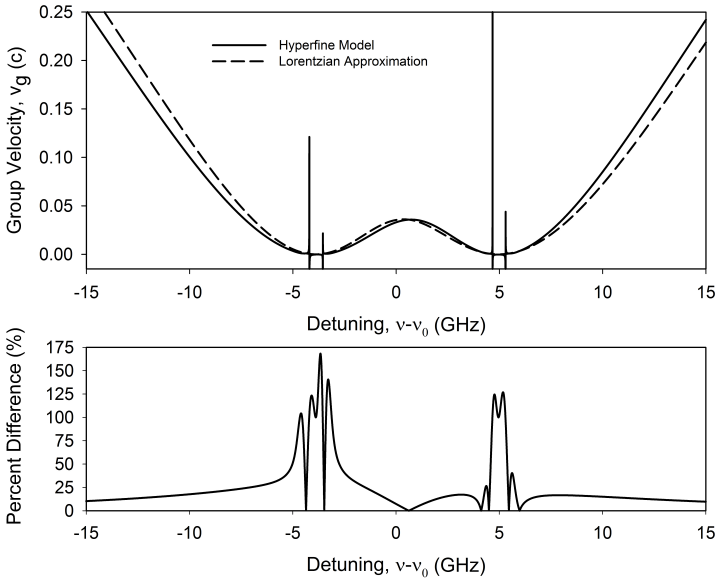

Figure 13. Comparison of group velocity at 114 °C computed from the hyperfine model of Equation (87) (solid line) and double Lorentzian index of refraction approximation (dashed line). Percent difference between models is shown for comparison.

These predicted delays are overlaid with the experimental observations in Figure 11. The agreement is excellent for all frequencies and temperatures.

The delays are often computed assuming two Lorentzian profiles split by the ground state hyperfine structure (Camacho et al., 2007, 2006a, 2007; Shi et al., 2007). This approximation is adequate when the laser is detuned from the resonances by an order of magnitude greater than the inhomogeneous linewidth (Camacho et al., 2007). However, significant differences in the frequency dependence of the predicted group velocities are observed when the two approaches are compared, as seen in Figure 13.

For the two Lorentzian model of the index of refraction (Camacho et al., 2007)

$$n(\delta) = 1 - \frac{\mathcal{A}}{2}\left(\frac{g_1}{\delta - \omega_1 + i\gamma} + \frac{g_2}{\delta - \omega_2 + i\gamma}\right) \tag{97}$$

and

$$\mathcal{A} = \frac{N|\mu|^2}{\epsilon_0 \hbar (g_1 + g_2)} \tag{98}$$

where N is number density, $|\mu|^2 = 2.1947 \times 10^{-29}\,\mathrm{C\,m}$ is the far detuned dipole moment (Steck, 2009), $g_1 = 7/16$, $g_2 = 9/16$, $\omega_1 = -3880\,\mathrm{MHz}$, $\omega_2 = 4980\,\mathrm{MHz}$, $\gamma = 2.617\,45\,\mathrm{MHz}$ (2γ is the Lorentzian FWHM $\approx$ natural linewidth), and $\mathcal{A} = 2.984\,65\,\mathrm{MHz}$ at 114 °C.

Across the vapor pressure equation's temperature range (Alcock et al., 1984), 300 K to 550 K, used in the hyperfine Voigt profile model, the group velocity deviation due to Doppler broadening remains approximately as shown in Figure 13. Indeed the best case for model agreement occurs with no pressure broadening. Between the absorption peaks at zero detuning a 7.3% difference in the predicted group velocity is observed for the model baseline conditions of Figure 13. For comparison at higher pressure broadening, with 1/4 atmospheres helium buffer gas and the alkali cell at 114 °C, the Lorentzian FWHM $\Delta\nu_H$ is approximately 1/3 of the hyperfine splitting. In this case, where the two absorption peaks remain relatively well defined as the absorption coefficient at zero detuning is approximately half the peak values, the two-Lorentzian approximation group velocity deviates 49.6% from the full hyperfine structure Voigt profile group velocity.

Pulse Delay Images

Pulse delays were observed using a setup similar to the aforementioned single-beam pulse delay measurements using a Princeton Instruments PI-MAX intensified charge-coupled device (ICCD) gated camera system, shown in 14. A beam expander was placed before the alkali cell so the expanded pulse flooded the alkali cell and surrounding space inside the heater block. The PI-MAX was used in place of the silicon detector without the compound lens attached so the expanded beam shown directly on the PI-MAX ICCD array.

The PI-MAX camera used is capable of imaging frame gates as small as 0.5 ns.

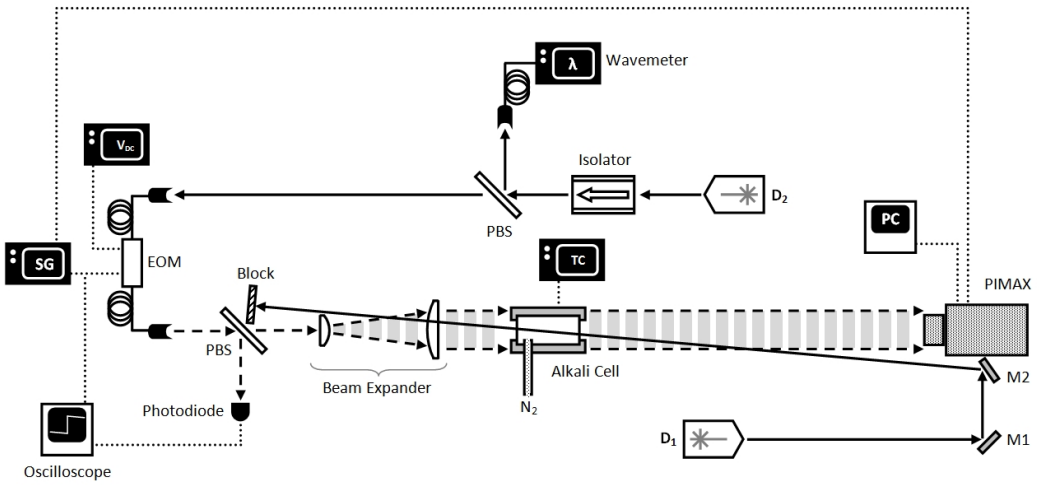

Figure 14. Experimental setup for pulse delay observation with Princeton Instruments PI-MAX image array.

The camera used contains 256 × 1024 spectrometer ICCD array. The camera was turned on its side to align the ICCD array vertically with the expanded beam and the vapor cell such that pulses arriving both inside and outside the cell could be imaged simultaneously thus providing temporally imaged evolution of delayed and non-delayed pulses. Close-up detail of the image array relative to the alkali-metal vapor cell are shown in 15.

Four 0.5-ns frames of a multi-frame TIFF imaged with the PI-MAX ICCD are shown in 16. Each image of the 256 × 1024 array captures laser pulses outside the alkali-metal vapor cell shown at the top of each image and laser pulses imaged through the reference cell. The edge of the Pyrex®reference cell is highlighted with dashed curves. The series of images details the time evolution of a 10-ns FWHM pulse delayed 20 ns where frame (a) shows the cell prior to the pulse arrival at 0 ns, (b) shows peak non-delayed pulse intensity outside the cell at 23 ns, (c) captures the peak delayed pulse intensity at 43 ns, and (d) shows the vapor cell after the pulse passage at 55 ns.

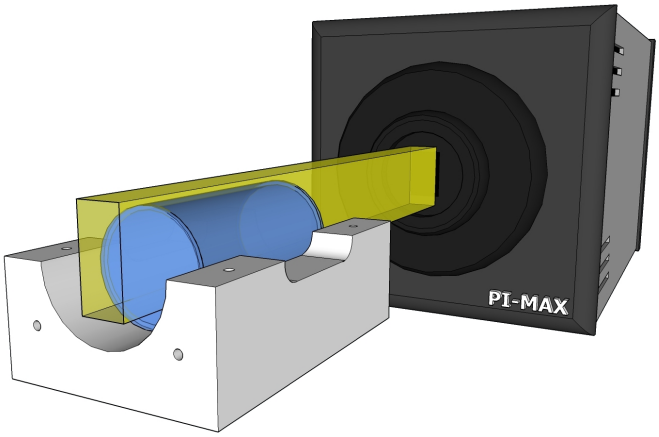

Figure 15. Close up detail showing half heater block with alkali-metal vapor cell. The PI-MAX intensified CCD (ICCD) image array is shown as the extruded rectangle intersecting the vapor cell. Notice the image array captures non-delayed pulses outside the alkali-metal vapor cell with the expected delayed pulses imaged through the reference cell.

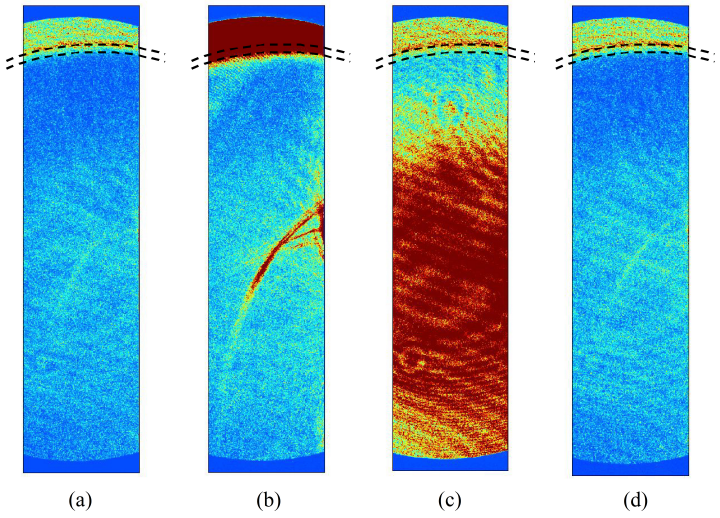

Figure 16. Four frames taken from PI-MAX intensified CCD (ICCD) image array. Each 256×1024 image array frame captures laser pulses outside the alkali-metal vapor cell shown at the top of each image and laser pulses imaged through the reference cell. The edge of the Pyrex®reference cell is highlighted with dashed curves. The series of images details the time evolution of a 10-ns pulse delayed 20 ns where (a) shows the cell prior to the pulse arrival at 0 ns, (b) shows peak non-delayed pulse intensity outside the cell at 23 ns, (c) captures the peak delayed pulse intensity at 43 ns, and (d) shows the vapor cell after the pulse passage at 55 ns.

Conclusion

Tuning of optical pulse delays obtained in the hyperfine doublet structure for the alkali atoms may be achieved through frequency modulation. Indeed, delays of 0 ns to 37 ns have been observed in a single pass through a 5-cm Cs cell at 137.2 °C by detuning from resonance 25 GHz. Delay predictions are nearly exact when the modeling precisely matches the absorption profile including Voigt lineshapes and full hyperfine structure. The frequency dependence of the delays are sensitive to vapor pressure, constraining cell temperature uncertainties to about 0.1 °C. Using the Voigt profile and hyperfine structure allows for accurate prediction of the pulse delay achieved by frequency tuning.

V. Hole Burning

The full frequency dependence of the optical delay in the Cs D_1 ($6\,^2S_{1/2} - 6\,^2P_{1/2}$) line has been observed, including all four hyperfine split components. Pulse delays of 1.6 ns to 24.1 ns are obtained by scanning across the hyperfine splitting associated with the lower $^2S_{1/2}$ state. Optical control of pulse delays in cesium vapor were demonstrated by pumping the D_2 ($6\,^2S_{1/2} - 6\,^2P_{1/2}$) transition and observing resulting holes in the D_1 delay spectrum. For a pump at four times the saturation intensity, the pulse delays are reduced by a maximum of 78% in a narrow region of 110 MHz. The frequency dependence of the delays of the probe laser in the vicinity of the spectral holes agrees with a Kramers-Kronig model prediction.

Introduction

Numerous applications from communications to interferometry for remote sensing stand to benefit from the tunable delay of optical pulses. Several methods have been used seeking to achieve a rapidly tunable optical delay system capable of delaying pulsed information multiple pulse widths with little loss of signal amplitude and no pulse dispersion. It is well understood that coherently coupled fields can produce slow light through electronically induced transparency (EIT) (Fleischhauer et al., 2005; Boller et al., 1991; Kasapi et al., 1995). Researchers have exploited an alternate method of controlling pulse delays through the rapidly varying frequency-dependent absorption near atomic transitions (Grischkowsky, 1973; Tanaka et al., 2003; Camacho et al., 2006a). We previously reported controlling optical delay by tuning a single laser across the D_2 ($6\,^2\mathrm{S}_{1/2} - 6\,^2\mathrm{P}_{1/2}$) absorption spectrum of cesium vapor (Anderson and Perram, 2010a). By extending the spectral analysis to include Voigt profiles with the Doppler component, the full frequency dependence of the observed delays was adequately described. In this paper we extend this analysis to the Cs D_1 ($6\,^2\mathrm{S}_{1/2} - 6\,^2\mathrm{P}_{1/2}$) spectrum where the hyperfine splitting the large enough to resolve all four

components. Agarwal and Dey proposed using hole burning in a Doppler-broadened atomic vapor using a counter propagating pump beam to saturate the media and achieve group indices of about 10^3(Agarwal and Dey, 2003). Narrower resonances may be achieved using quantum coherence effects (Bigelow et al., 2003). Shakhmuratov *et al.* extended the technique to persistent spectral hole burning and slow light in inhomogeneously broadened solid materials (Shakhmuratov et al., 2005). Most recently, Camacho *et al.* experimentally realized these concepts in hot rubidium vapor (Camacho et al., 2006b). The pump laser induces transparency by moving population from the probed hyperfine state to the other hyperfine component, not by coherent effects. This work focused on frequency modulation of the pump beam to tune delays of up to 45 ns (Camacho et al., 2006b).

In this experiment we use a continuous wave (CW) D_2 pump laser to depopulate a given velocity group in the Cs ground state and probe the full frequency dependence of the delays observed in the D_1 absorption spectrum. Monitoring pulse delays as a function of probe frequency clearly revealed a pump intensity dependent hole.

Experimental Setup

Experimental setup for hole burning delay measurements shown in Fig. 17 is a modified sub-Doppler absorption spectroscopy experiment where counter propagating beams intersect in the hot cesium vapor cell. A New Focus Velocity™ model 6316 20-mW tunable diode laser with a linewidth less than 300 kHz serves as the pump laser on the D_2 Cs transition (852 nm). The pump laser is directed through a pellicle beam splitter where a beam sample is sent to a Bristol model 621A wavelength meter with 0.075 GHz (0.0025 cm^{-1}) accuracy for frequency reference. The main pump beam is directed through a 5-cm-long, low-pressure cesium vapor cell enclosed in a machined aluminum heater block maintained at a constant temperature $\pm 2\,^{\circ}C$ between $40\,^{\circ}C$

and 120 °C using a temperature controller system.

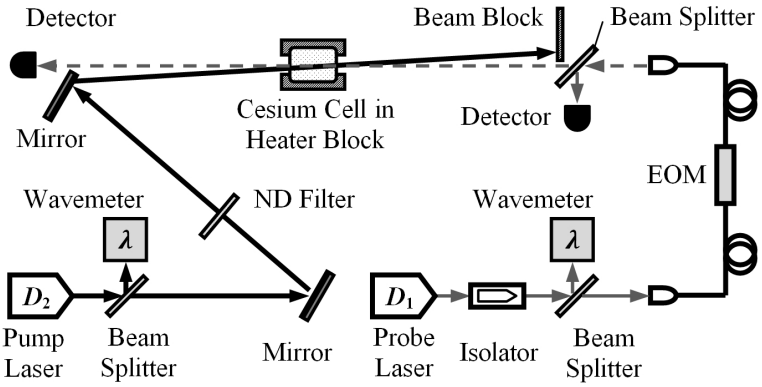

Figure 17. Experimental setup for hole burning delay measurements.

A New Focus Velocity™ model 6318 6-mW tunable diode laser with less than 300-kHz linewidth is used as the D_1 probe laser at 894 nm. The probe beam is directed through an optical isolator and a pellicle beam splitter. A probe beam sample is sent to a second Bristol model 621A wavelength meter while the main probe beam continues to a EOSPACE fiber-coupled Mach-Zehnder interferometric lithium niobate ($LiNbO_3$) electro-optic intensity modulator (EOM). A Picosecond Pulse Labs 1.6-GHz pulse/pattern generator drives the EOM to create a Gaussian 7.5-ns full-width at half-maximum (FWHM) pulse with 133 Hz repetition rate. The modulated probe is split exiting the EOM fiber to a silicon photodiode detector with 2.3-ns response time providing initial intensity reference before the alkali-metal vapor cell. The probe beam is aligned overlapping but counter propagating to the pump beam in the Cs cell enclosed in the heater block. Probe pulse delay is measured after the alkali-metal vapor cell by a silicon photodiode detector with a 1-ns response time.

Pulse delay temporal waveforms were 2000 pulse averages recorded on a 3 GHz oscilloscope triggered by the pulse generator signal. The CW D_2 pump is set at a fixed power and frequency detuned from an absorption peak. Neutral density filters placed in the D_2 pump beam path to vary pump power at 0 mW (blocked), 5 mW

and 16 mW. Probe laser is scanned across the D_1 absorption spectrum near $F'' = 4$ to $F' = 3, 4, 5$ as depicted on the Cs energy level diagram in Fig. 18. Simulated absorption coefficients for Cs D_1 and D_2 at 50 °C are shown in Fig. 19. The x-axis is labeled using both nanometer (nm) and detuning frequency $\nu_{\Delta 1}$ and $\nu_{\Delta 2}$ (GHz) scales. The detuning frequencies $\nu_{\Delta 1}$ and $\nu_{\Delta 2}$ represent detuning from the central atomic transition frequency 335.116049 THz for D_1 and 351.725718 THz for D_2. Regions of the absorption spectra used in this experiment are highlighted with gray squares.

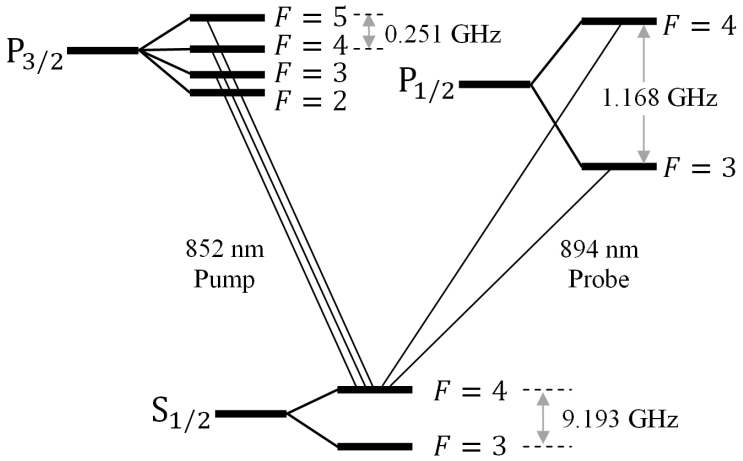

Figure 18. Energy level diagram depicting the pump D_2 transitions and probe D_1 transitions Energy level separations are not drawn to scale.

Optical Delay

Previous work estimated pulse delay using a group velocity through the Kramers-Kronig relations to find the real index of refraction n_R from the absorption coefficient α (Anderson and Perram, 2010a,b) such that

$$n_R = 1 + \frac{c}{2\pi^2} \mathrm{P} \int_0^\infty \frac{\alpha(\xi)}{\xi^2 - \nu^2} d\xi. \tag{99}$$

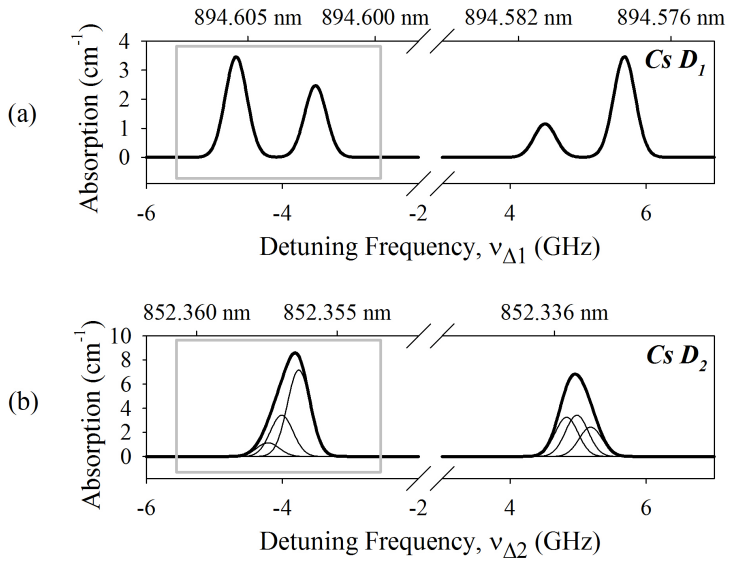

Figure 19. Simulated absorption coefficients for the (a) D_1 and (b) D_2 transitions at 50 °C. Single hyperfine transition absorption lineshapes are shown in the D_2 spectrum as thin black lines. Regions of the D-line absorption spectra used in this experiment are highlighted by gray squares.

Optical pulse delays are calculated as $t_d = l/v_g$ for cell length l where the group velocity is defined as

$$v_g = \frac{c}{n_R + \nu \frac{dn_R}{d\nu}}. \tag{100}$$

Observed D_1 pulse delays compared favorably to previous work in Cs D_2 at similar temperatures. Kramers-Kronig delay model prediction and observed delays for a Cs vapor cell at 109.5 °C are shown in Fig. 20 where the solid line represents the delay model prediction. The Cs D_1 on resonance optical thickness $\ell = 1/\sigma(\nu_0)n \approx 0.05$ mm for the $F'' = 4 \rightarrow F' = 3$ transition $\nu_{\Delta 1} = -4.665$ GHz at 109.5 °C.

The pulse/pattern generator produced a nearly Gaussian 7.5-ns pulse as shown in Fig. 21. Sample pulses at three D_1 detuning frequencies $\nu_{\Delta 1}$ are depicted as a series of gray shapes where (1) is farthest from the absorption peak while pulse (3) is closest to the resonant transition frequency. Solid black lines show Gaussian fit curves, and the peak of the fit curve is marked for reference. As expected the pulse

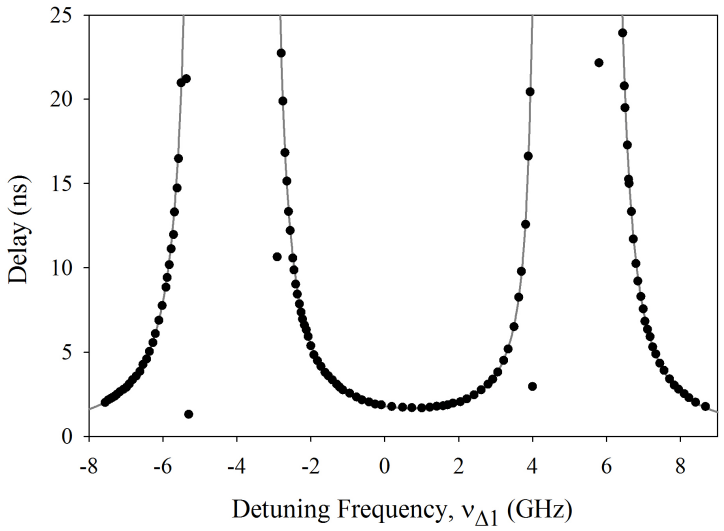

Figure 20. Pulse delay for full spectrum Cs D_1 scan from $\nu_{\Delta 1}$ = -8 GHz to +8 GHz. Cesium cell was maintained at 109.5 °C. No D_2 pump was used.

amplitude decreases for pulses closer to the peak absorption while the pulse width increases due to dispersion. Peak time for each Gaussian fit is recorded as the pulse arrival time. Zero-delay time is determined when the probe is detuned far off resonant frequency and the value is subtracted from the arrival time for each pulse to calculate the pulse delay. Maximum error in delay time measurement is ±0.15 ns with average error ±0.03 ns. Near the resonant transitions resolving the peak is difficult as the pulse amplitude is attenuated approaching detector noise level. Pulse peaks lost in the noise appear in Fig. 20 as 'stray' data points below the model prediction curve.

As demonstrated in Fig. 21, pulses generally decrease in amplitude near absorption peaks and the pulse FWHM increase. Dispersion of the Gaussian fit is shown in Fig. 22. As the probe is tuned toward the transition frequency with no pump laser, pulses initially appear to broaden before pulse narrowing is briefly observed. At higher pump intensities, pulse dispersion appears more evident near resonant frequency peaks, however narrowing is not observed before pulse attenuation prevents

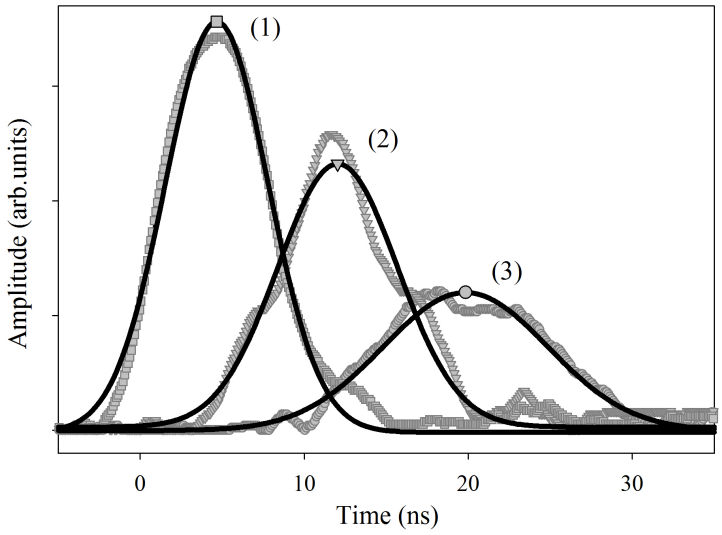

Figure 21. Pulse shape for selected pulses from data depicted in Fig. 20 at 109.5 °C. Pulse data for pulse at three D_1 detuning frequencies $\nu_{\Delta 1}$ are depicted using gray lines. Solid black lines show Gaussian fit curves, and the peak of the fit curve is marked for reference. (1) $\nu_{\Delta 1} = 7.44$ GHz, peak at 4.66 ns, width 7.37 ns (2) $\nu_{\Delta 1} = 6.73$ GHz, peak at 12.04 ns, width 8.60 ns (3) $\nu_{\Delta 1} = 6.5$ GHz, peak at 19.84 ns, width 11.83 ns.

accurate resolution of the pulse.

High-temperature delay, where Doppler-broadened absorption masks the individual hyperfine D_1 peaks as in Fig. 20, compares favorably to previous work(Anderson and Perram, 2010a). This work reports higher frequency sampling with 200 frequency samples over 20 GHz compared to previous work in Cs D_2 90 samples over 20 GHz (Anderson and Perram, 2010a). The full frequency dependence of the optical delays for the Cs D_2 line, similar to that now reported for the D_1 line in Fig 20, have been successfully modeled as expressed by equations 99 and 100. However, the hyperfine structure of the excited $^2P_{3/2}$ state was unresolved and delays at frequencies between upper state hyperfine components has not previously been investigated. The spectral simulation illustrated in 20 agrees very well with the observed pulse delays in this region.

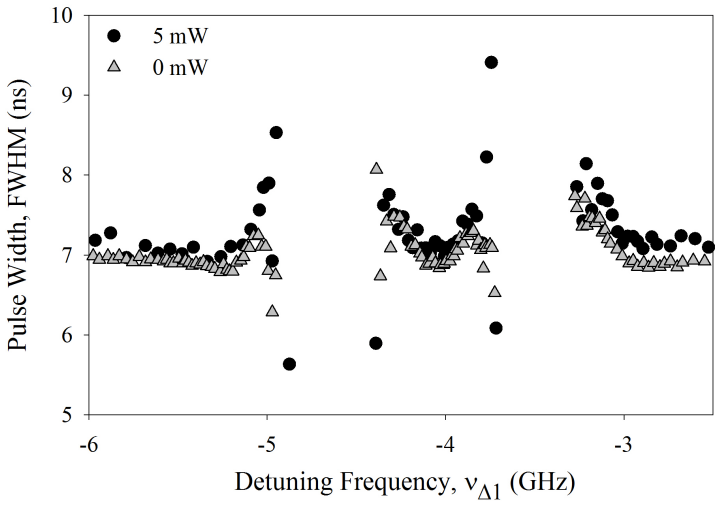

Figure 22. Pulse width in the neighborhood of D_1 absorption peaks. Gaussian pulse fit FWHM is shown for 0 mW (no pump) and 5.6 mW across the D_1 spectrum between $\nu_{\Delta 1}$ = -6 GHz and -2.5 GHz.

Intensity-Dependent Delay

Crossing laser beams in a modified saturation spectroscopy setup is a simple way to reduce Doppler broadening of spectral lines and examine hyperfine structure near the natural broadening limit. Given a pump at frequency ν_{pump} and D_2 hyperfine transition at ν_{D2}, the beams interact at similar velocity groups determined by the frequency difference $\delta\nu_{pump} = \nu_{pump} - \nu_{D2}$. Spectral holes are burnt at frequency ν_{hole} such that $\nu_{hole} = \nu_{D1} - \delta\nu_{pump}$ for each hyperfine transition. For beams that are not perfectly aligned to be counter propagating and intersecting, there will be some residual Doppler component. The depth and width of the holes are intensity dependent where hole width $\Delta\nu_{hole}$ is a function of intensity and saturation intensity I_{sat} such that

$$\Delta\nu_{hole} \propto \left(1 + \frac{I}{I_{sat}}\right)^{1/2}. \tag{101}$$

Overall D_1 absorption decreases as D_2 pump laser power increases due to ground state depletion and spectral holes are evident in the D_1 absorption. The absorption

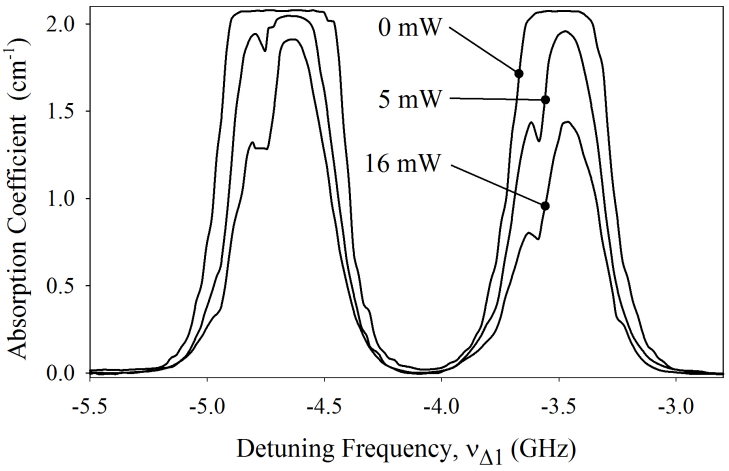

Figure 23. Absorption coefficients for Cs D_1 with Cs D_2 pump at $\nu_{\Delta 2}$ = -3.84 GHz (852.3566 nm, 11732.1790cm^{-1}) various pump powers.

spectra for a low-pressure Cs cell at 44 °C with a D_2 pump at a fixed frequency $\nu_{\Delta 2}$ = -3.84 GHz (852.3566 nm, 11732.1790 cm^{-1}) at 0 mW (no pump), 5.7 mW and 16.4 mW are shown in Fig. 23. At the resonant frequency, the D_1 laser is 2.3% I_{sat} while D_2 pump intensity is approximately $4 \times I_{sat}$ at 5.6 mW and $12 \times I_{sat}$ at 16.4 mW.

In the presence of holes burnt in the D_1 absorption spectra, predicted delay is calculated from observed absorption spectra using the Kramers-Kronig model to calculate group velocity and pulse delay. Observed delay and the predicted delay for Cs at 52.5 °C, $\nu_{\Delta 2}$ =-3.84 GHz at three D_2 pump powers are shown in Fig. 24. Pump power is adjusted using neutral density filters as changing diode current causes a subsequent shift in pump laser frequency.

Rapid variations in predicted delay near absorption peaks in Fig.24 are due to frequency instability of the pump/probe lasers in a region of highly dispersive absorption. In general the D_1 optical delay decreased with increasing D_2 pump power. It is speculated that this may provide a rapidly tunable optical delay mechanism by varying pump power though it has not been verified how quickly the system can

respond to changes in pump intensity.

Hole Burning Effects

Sub-Doppler spectroscopy removes some of the velocity-induced broadening using counter propagating beams interacting with atoms moving within a narrow velocity class. For a single resonant transition at ν_0 a pump beam detuned $+\delta\nu$ interacts with atoms at $\nu_0 + \delta\nu$ effecting the observed spectrum of a counter propagating probe beam at $\nu_0 - \delta\nu$. In cesium D_2 there are three closely spaced hyperfine components corresponding to the allowed transitions of the $^2P_{3/2}$ energy splitting as shown in Fig. 18 and Fig. 19. A D_2 pump interacts with velocity groups detuned $+\delta\nu_i$ from each hyperfine component. The counter propagating D_1 probe sees spectral holes at corresponding velocity groups $-\delta\nu_i$ from each D_1 hyperfine component.

In the neighborhood of the spectral hole absorption changes rapidly across a narrow frequency range. The Kramers-Kronig delay model predicts a significant change in delay in the hole region. To observe the effect of a spectral hole on the pulse delay, the D_2 pump laser was set at $\nu_{\Delta 2}$ =-3.86 GHz for 16.4 mW and 52.5 °C while the D_1 probe was scanned across the absorption spectrum from $\nu_{\Delta 1}$ =-6 GHz to -2 GHz.

The observed transmittance is shown in Fig. 25 with a no pump reference absorption spectrum (dashed lines) to visualize the spectral holes. A simulated absorption spectrum was then created using the observed spectrum as a reference by subtracting a series of Lorentzian line shapes from the reference absorption spectrum. The resulting difference is in the absorption spectrum is shown in Fig. 25 as the solid lines. Lorentzian line shapes used in the prediction have frequency differences of 192 MHz and 285 MHz compared to accepted hyperfine splitting of approximately 201 MHz and 251 MHz. The Lorentzian FWHM for the absorption corrections is 110 MHz which is more than 20 times the natural linewidth for Cs D_1 and D_2 and less than

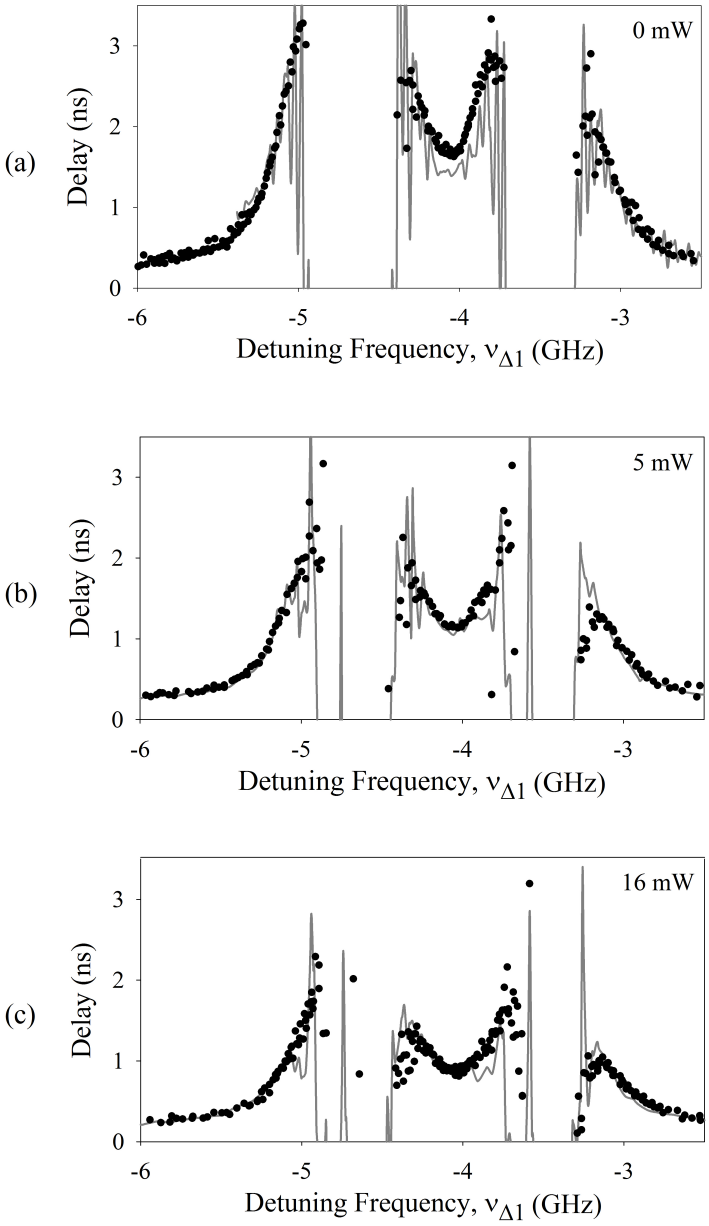

Figure 24. Observed delay (black dots) and the predicted delay (gray lines) for Cs at 52.5 °C, $\nu_{\Delta 2}$ = -3.84 GHz at three D_2 pump powers of (a) 0 mW (no pump), (b) 5.7 mW and (c) 16.4 mW. Predicted delay at each power is calculated using the observed absorption spectra and the Kramers-Kronig relations model.

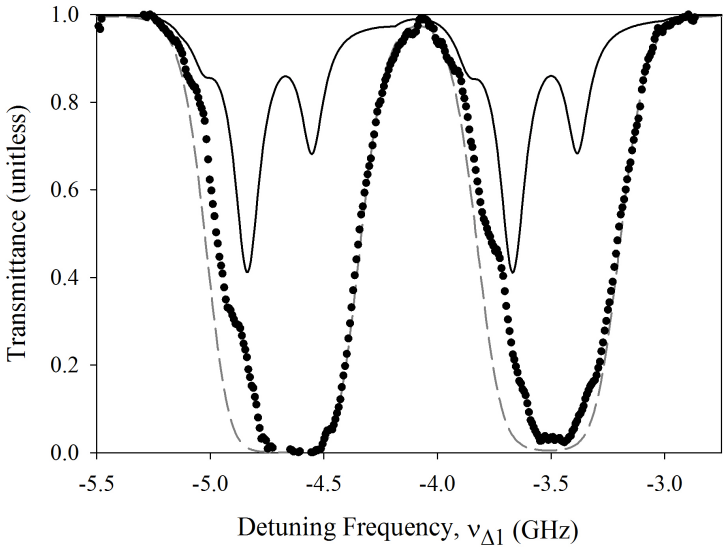

Figure 25. Observed Cs D_1 transmittance with reference absorption spectrum (dashed lines) to visualize the spectral holes. Difference in the absorption spectrum is shown as solid lines.

the Doppler width (∼400 MHz). Frequencies used for each Lorentzian line shape used to approximate the reference absorption spectrum are on the order of the hyperfine separation of the Cs D_2 $F'' = 4 \rightarrow F' = 3, 4, 5$ transitions. The modified absorption curve similar to the observed absorption spectrum is then used to predict the optical delay using the Kramer-Kronig model and the resulting delay prediction and observed delay is given in Fig. 26. The observed delay in the region of the hole match the Kramer-Kronig model prediction in general shape and magnitude.

Conclusion

The frequency dependence of the optical pulse delay in cesium D_1 closely match the previously developed model predictions using Voigt lineshapes and the full hyperfine structure. The observed D_1 optical pulse delays compared favorably to similar results in Cs D_2. The delay prediction Kramers-Kronig model accurately predicts the delays between D_1 upper state hyperfine components at lower temperatures than

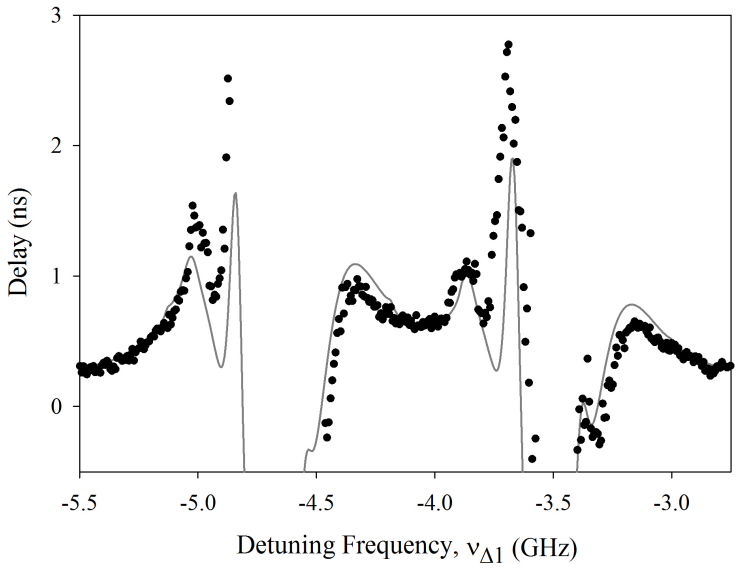

Figure 26. Pulse delay in the narrow spectral region surrounding a hole burnt in the Cs D_1 absorption spectrum. Solid line depicts the model delay prediction.

previously reported with smaller frequency sampling separation. Delays up to 24 ns where achieved by detuning from resonance by 10 GHz.

Tunable optical delays were demonstrated with a Cs D_1 pulse by varying D_2 pump laser power. Increasing D_2 pump power reduced D_1 absorption overall. Observation of hole burning effects on delay close to the spectral hole were noted. Location of the holes and predicted delay from a modified absorption spectrum matched model predictions. For a pump intensity of four times saturation intensity I_{sat} observed delay is reduced by an average of 50% across the spectrum and reaches a maximum of 78% in a narrow 110 MHz spectral hole region.

VI. Hyperfine Relaxation

A Cesium D_2 ($6\,^2S_{1/2} - 6\,^2P_{3/2}$) probe laser is used to examine temporal pulse dynamics during a 10-ns high-power D_2 pulse event. The probe laser is set perpendicular to the pump pulse in a heated Cs optical cell with helium buffer gas. The probe frequency is scanned across the D_2 transitions and the dynamic excitation and relaxation of the hyperfine components is studied relating to temperature, buffer gas pressure, and pump/probe intensity.

Introduction

Alkali-metal vapor laser systems were available shortly after the laser's invention using cesium vapor $6S_{1/2} \rightarrow 8P_{1/2}$ pumped at 388.8 nm (Rabinowitz et al., 1962). Alkali-metal elements have a simple atomic structure with a single valence electron and are relatively simple to model. The quantum defect can be quite small leading to highly efficient laser systems such as diode-pumped alkali laser (DPAL) systems (Krupke et al., 2003). Diode-pumped alkali lasers are excellent three-level lasers provided the D_1 and D_2 absorption profiles are sufficiently broadened to match pump linewidth and population excited to the $^2P_{3/2}$ level can be quickly relaxed to the upper lasing $^2P_{1/2}$ state. Broadening is typically achieved using a homogeneous pressure broadening species such as helium and a collisional $P_{3/2} \rightarrow P_{1/2}$ relaxation gas such as ethane (Krupke et al., 2003). DPAL systems have been successfully demonstrated in Rb (Krupke et al., 2003), Cs (Beach et al., 2004; Ehrenreich et al., 2005) and other alkali-metal vapors building hopes that DPAL systems offer a scaling path to high power laser systems without the thermal management issues of solid state lasers or the hazards of chemical laser systems.

Modeling of the intra-cavity dynamics, such as thermal effects and bleached amplification medium, of a DPAL system and subsequent validation of the theoretical

description are critical to power scaling and maximizing laser efficiency. Optical measurement of the bleach wave dynamics have not been previously accomplished. Except for a very small increase in probe intensity at the absorption peak, the methodology described in this section did not prove successful in imaging the bleach wave, however other significant pulsed-pump hyperfine dynamics were observed.

Direct observation of hyperfine relaxation is difficult due to the hyperfine filters required to observe resonance lines (Beverini et al., 1971). Typical hyperfine relaxation rates are measured for alkali-foreign-gas collision-induced relaxation of the various ground state levels (Beverini et al., 1971; Bernabeu and Alvarez, 1980; Tornos and Amare, 1986), normally accomplished at low temperatures to reduce Cs-Cs collisions. Wall collisions and diffusion are predominant factors besides the intended foreign-gas interactions. In previous work hyperfine relaxation of the moderately spaced D_1 levels with a collisional gas were studied (Morgus et al., 2008) using counter propagating pump beams at Cs D_1 and to excite $6P_{1/2}$ atoms to the $8S_{1/2}$ level with a 761.1 nm pump laser. Relaxation was observed measuring side fluorescence of the $8S_{1/2} \rightarrow 6P_{3/2}$ photons.

To the best of my knowledge pump-probe study of the hyperfine relaxation related to pulsed pump rates for DPAL systems has not been accomplished. This work examines pulsed pump dynamics of a DPAL-like cesium vapor cell related to the excitation and relaxation to pre-pulse equilibrium of hyperfine components.

Experimental Setup

The experimental setup to measure pulse dynamics is shown in Figure 27. A Spectra Physics™ Quanta Ray PRO-290 Nd:YAG laser is used as a pump laser for the Sirah™ Precision Scan PRSC-D-18 pulse dye laser (LDS 867 dye mixture) which produced a 10 ns pulse with 800 KJ per pulse at 10 Hz and a spectral linewidth

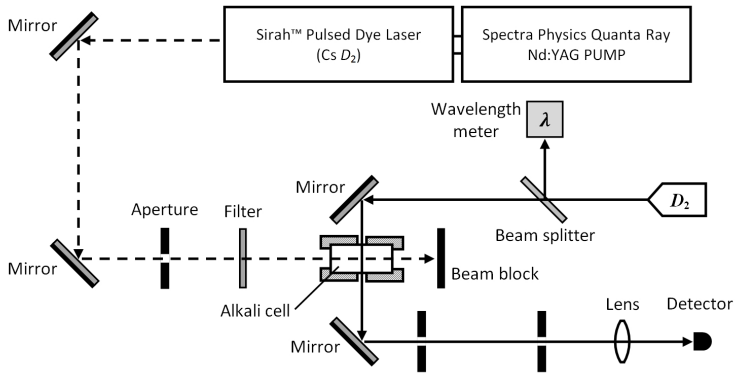

Figure 27. Setup for hyperfine relaxation experiments. A 10 Hz Sirah dye laser generates high-power pump pulses sent through the Cs vapor cell. A low-power D_2 probe passes perpendicular to the pump pulse.

of 1.4 GHz at 852.34 nm. For comparison closely spaced group of three hyperfine lines at Cs D_2 $\nu_{\Delta 2} \approx -4\ GHz$ has a Doppler-broadened FWHM of 0.8 GHz so that the pump pulses cover the full set of three Cs D_2 upper state hyperfine split energy levels. The pulsed pump beam is directed through a series of mirrors and an aperture to limit the spatial pump beam width to the diameter of the cesium cell. The 2.5 cm beam passes through the heated alkali cell and into a beam block. Care was taken to eliminate reflections and scattered pump light with the extensive use of black foam board and blackout curtains.

A New Focus Velocity™ model 6316 20-mW tunable diode laser with a linewidth less than 300 kHz serves as the continuous wave probe laser on the D_2 Cs transition (852 nm). The probe laser is directed through a pellicle beam splitter where a beam sample is sent to a Bristol model 621A wavelength meter with 0.075 GHz (0.0025 cm^{-1}) accuracy for frequency reference. The probe beam is directed through the alkali-metal vapor cell perpendicular to the pump beam and is then directed along a 5 m path through two apertures to eliminate pump beam reflections and side fluorescence on the way to the detector. A 1-ns rise time silicon photodiode is used to collect probe beam intensity measurements recorded on a 3 GHz oscilloscope.

Results

The pump laser output 50 mW pulsed power at the cesium cell and was set to pump the D_2 absorption feature peaks at (1) 852.357 nm ($\nu_{\Delta 2}$ =-4. GHz) and (2) 852.335 nm ($\nu_{\Delta 2}$ =+5 GHz) as shown in Figure 28. Points A, B, C and D refer to frequencies detuned from the absorption peaks until the probe beam transmission is approximately 50%. Hyperfine $F'' \rightarrow F'$ transitions are labeled in Figure 28 for reference.

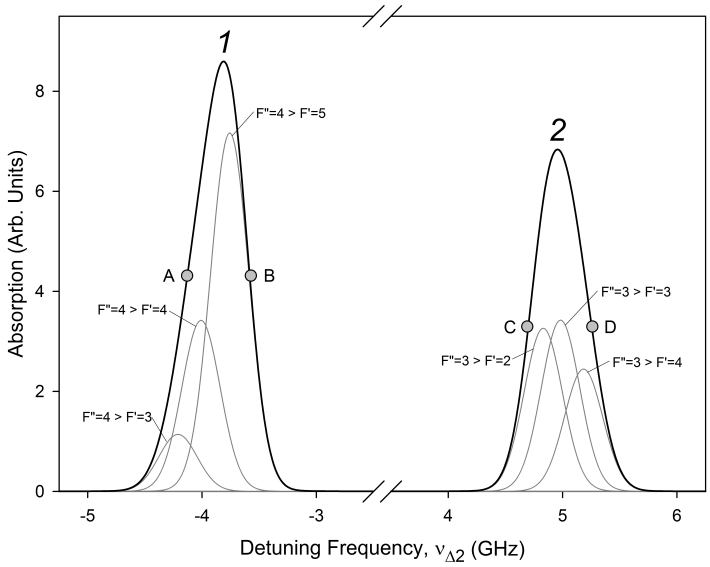

Figure 28. Cesium D_2 absorption with hyperfine structure. Reference locations A, B, C and D are set at 50% probe transmission and pump locations are labeled 1 and 2 at the absorption peaks.

It was hoped that the pump beam would bleach the Cs vapor and the probe beam would pass unattenuated around the pulse arrival time so that temporal and spatial observation of the DPAL bleach wave could verify theoretical results. While this was not the case, other interesting frequency-dependent hyperfine relaxation-related phenomena were observed.

There are distinct short-term and long-term effects following a pump pulse event.

Sample pump and probe intensities are shown in Figure 29. Pulse data is shown

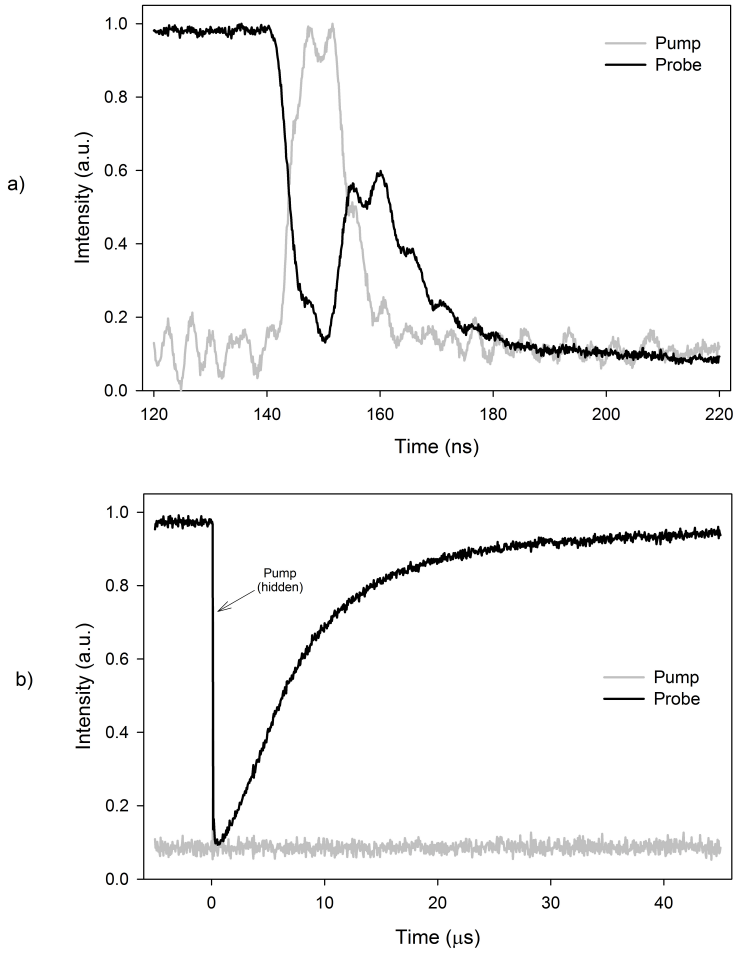

Figure 29. Sample pump and probe intensities at the detector. These sample pulses taken for probe Point A at 80 °C illustrate (a) the short-term nanosecond timescale effects in the neighborhood of the pump pulse and (b) long-term microsecond hyperfine effects and relaxation to pre-pump equilibrium.

for probe frequency at point A (852.357 nm), pump at frequency (2) 852.335 nm ($\nu_{\Delta 2}$ =+5 GHz), Cs cell temperature $T = 80\,^{\circ}\mathrm{C}$. The time axis is synchronized to the q-switch signal from the Quanta Ray Nd:YAG laser. Arrival time for the pump at 140 ns is shown as the gray line. Figure 29 (a) shows short-term effects on probe intensity, dropping initially during pulse arrival, partially returning before decreasing again past 200 ns. Figure 29 (b) shows long-term probe intensity decay to return to

pre-pulse equilibrium around 50 µs.

Full frequency spectra from $\nu_{\Delta 2} = \pm 7$ GHz illustrating short-term and long-term effects are shown in Figure 30 through Figure 33 for a pump at frequency (2) 852.335 nm ($\nu_{\Delta 2}$ =+5 GHz). In these figures, the absorbance spectrum plot is interpreted such that lower values indicate little absorption so that high probe signal intensity is transmitted.

Figure 30 shows nanosecond-scale pulsed pump effects as the probe is scanned in frequency across the Cs D_2 absorption spectrum. Figure 31 shows the absorbance at four distinct frequencies (A, B, C and D) from Figure 30 (see Figure 28 for frequency reference points).

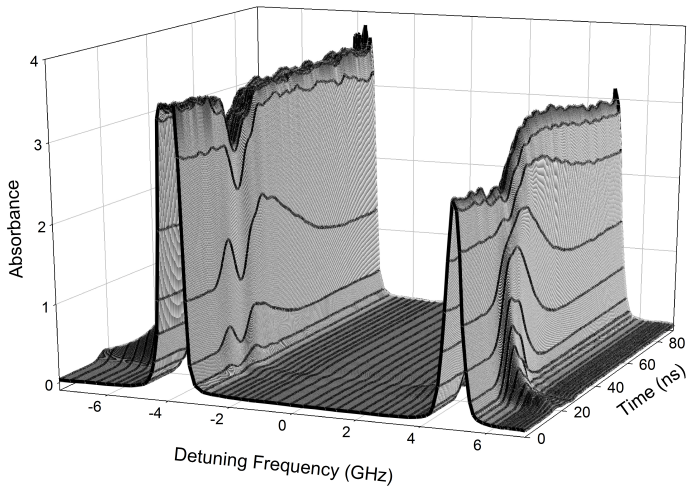

Figure 30. Nanosecond-scale frequency-dependent probe intensity after a pump pulse event at +5 GHz**.**

Figure 32 shows microsecond-scale pulsed pump effects as the probe is scanned in frequency across the Cs D_2 absorption features. Figure 33 shows the absorbance at four distinct frequencies (A, B, C and D) from Figure 32 (see Figure 28 for frequency reference points).

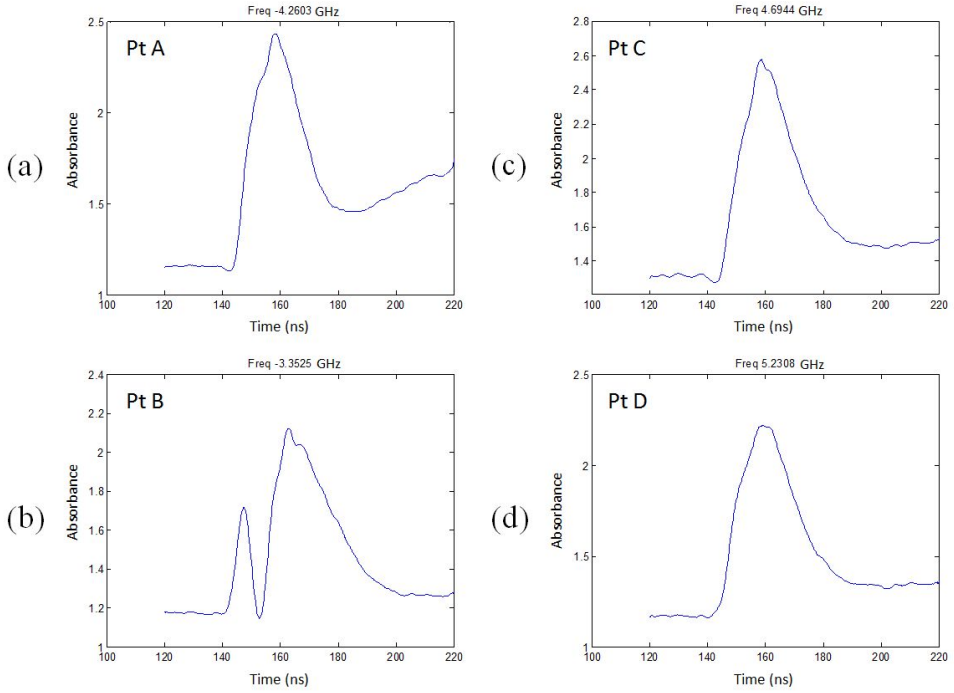

Figure 31. Nanosecond-scale frequency-dependent probe intensity after a pump pulse event at $+5\,\mathrm{GHz}$ at Points A, B, C, and D (See Figure 28 for graphical depiction of reference points).

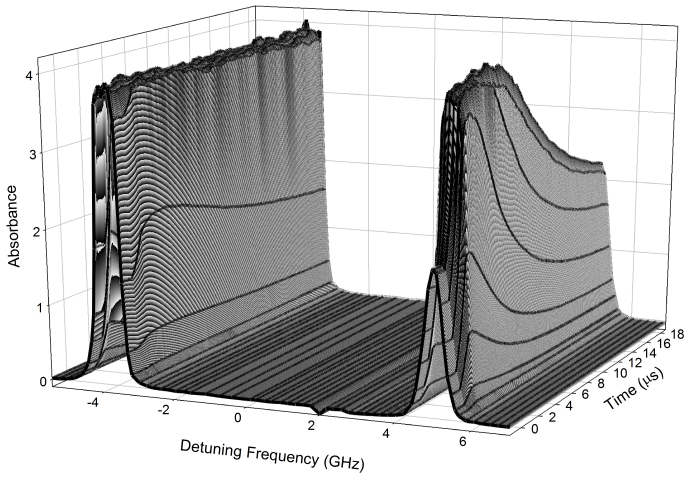

Figure 32. Microsecond-scale frequency-dependent probe intensity after a pump pulse event at $+5\,\mathrm{GHz}$.

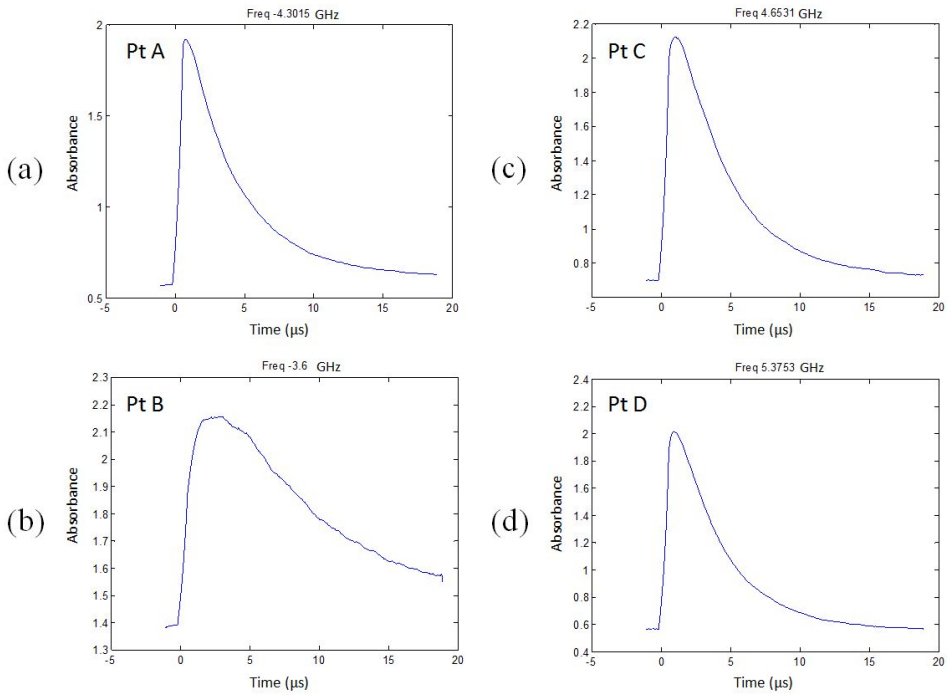

Figure 33. Microsecond-scale frequency-dependent probe intensity after a pump pulse event at $+5\,\mathrm{GHz}$ at Points A, B, C, and D (See Figure 28 for graphical depiction of reference points).

For the long-term effect each pulse is fit to a double exponential of the form

$$y = a + b\exp(-cx) + d\exp(-ex). \tag{102}$$

Detector intensity data is transformed using

$$y = -\ln\frac{I}{I_0} \tag{103}$$

where I_0 is the pre-pulse intensity. A sample pulse data plot with double exponential fit is shown in Figure 34 for a probe at point B with 21.4 mW probe power. Data

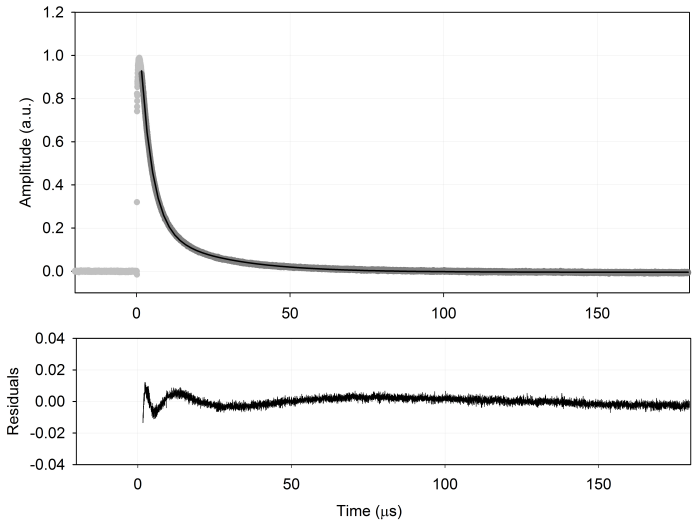

Figure 34. Sample data fit is shown for a probe at point B with 21.4 mW probe power. Data before the peak is excluded from the fit data and the fit function is shown as a solid black line.. Data for all samples is fit to a double exponential function of the form $y = a + b\exp(-cx) + d\exp(-ex)$. Residuals from the fit are shown below the data plot.

before the peak is excluded from the fit data, the resulting fit function is shown as a solid black line over the pulse data and residuals are shown below the data plot.

Data Trends

It should be noted in that in Figure 30 the short-term timescale pulse effects at the time of the pulse are observed far from the absorption peak, especially near point A, the Cs D_2 $F'' = 4 \rightarrow F' = 3, 4$ transitions. Little pulse effect is noted around point B in Figure 30 and the shape of the pump pulse is dramatically different compared the response at other frequencies. There is a small region of increased intensity (decreased absorption) at the -4 GHz absorption peak with the pump tuned to peak 2 at 5 GHz.

Similar hyperfine frequency-dependent pulse response and double-exponential return to equilibrium is evident in the long-term microsecond scale Figures 32 and 33. Decay curves in the A, C, and D regions are similar while the decay around B is markedly longer lived at 80 °C.

Recall some of the general trends in the absorption coefficient. As temperature increases, alkali concentration and inhomogeneous Doppler-broadening increase. Homogeneous broadening increases with buffer gas pressure. Pressured broadened Cs D_2 with He is broadened sufficiently that the 50% transmission "saddle" between the ground state splitting is no longer distinguishable before 15 Torr He at 90 °C. Therefore at higher temperatures and buffer gas pressures all four frequency points are no longer distinguishable. Therefore it is only possible to compare points A and B at low pressures and temperatures. Figure 35 shows the double exponential fit decay constants c and e for points A and B at various HE pressures up to 12 Torr at 93.5 °C. It it evident that the constants rapidly approach constant values with increasing He pressure.

Temperature dependence for points A and B data in Figure 36 shows that the c and e values converge to a single value indicating that the double-exponential decay curve converges to a single-exponential decay.

Closer examination of the He pressure dependence is shown in Figure 37. As He

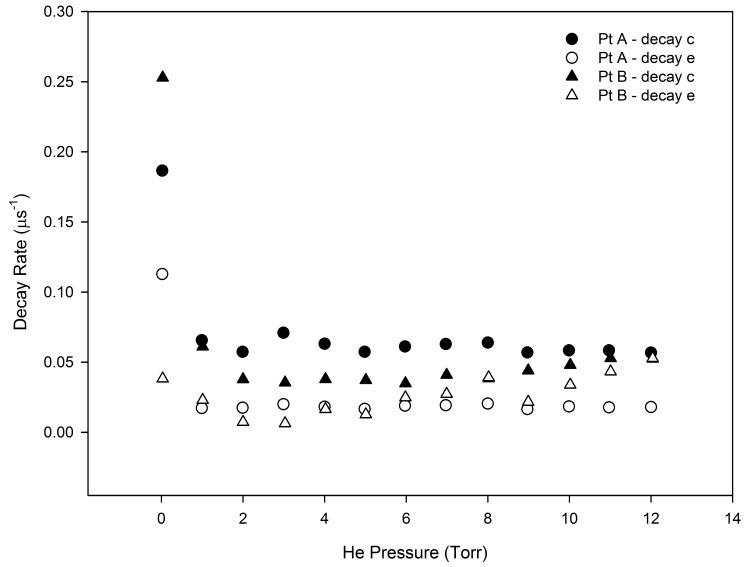

Figure 35. Decay rates c and e (from the double exponential fit function $y = a + b\exp(-cx) + d\exp(-ex)$) for probe frequencies A and B are shown at various He pressures (Torr).

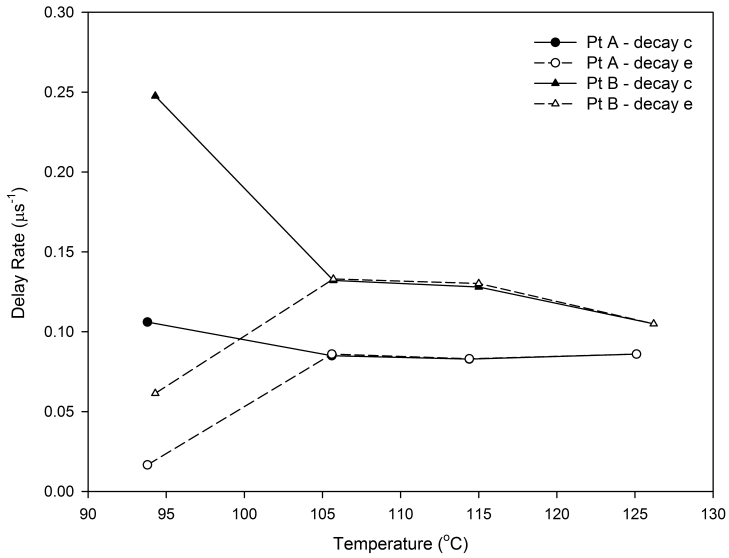

Figure 36. Decay rates c and e (from the double exponential fit function $y = a + b\exp(-cx) + d\exp(-ex)$) for probe frequencies A and B are shown at low He pressures (0.06 Torr).

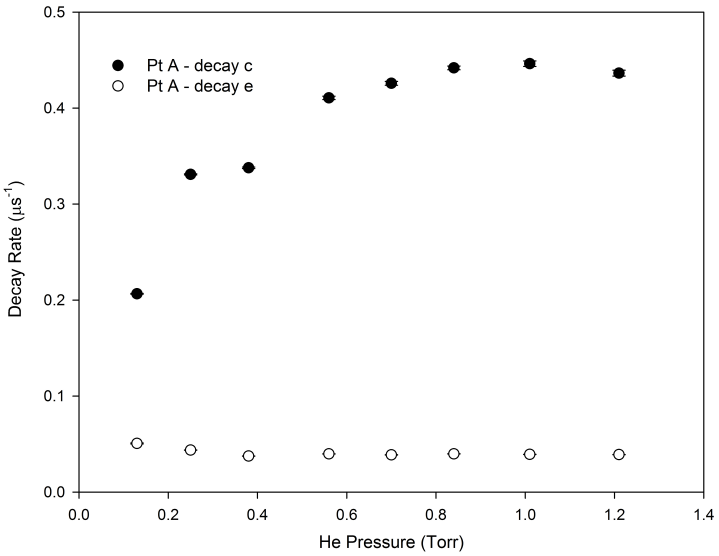

Figure 37. Decay rates c and e (from the double exponential fit function $y = a + b\exp(-cx) + d\exp(-ex)$) for probe frequency A are shown at low He pressures (0-1.2 Torr).

pressure increases the c decay rate peaks around 1 Torr He for point A at 93.5 °C and begins to decrease to the high-pressure value. The e decay constant remains relatively constant.

The decay constants quickly approach an asymptote at higher pressures as shown in Figure 38.

Decay rate as a function of pump and probe laser power is also examined in Figures 39 and 40 with a low-pressure alkali sample at 95.5 °C and pump laser at peak 2 (5 GHz). Decay rate as a function of probe power is shown in Figure 40.

Discussion

Several pump and probe characteristics were also examined. Various linear and circular pump polarization combinations were used and no polarization-induced changes could be identified. Pump intensity has the intuitive effect in that excitation increases with pump power (no pump shows no excitation or relaxation). Probe power depen-

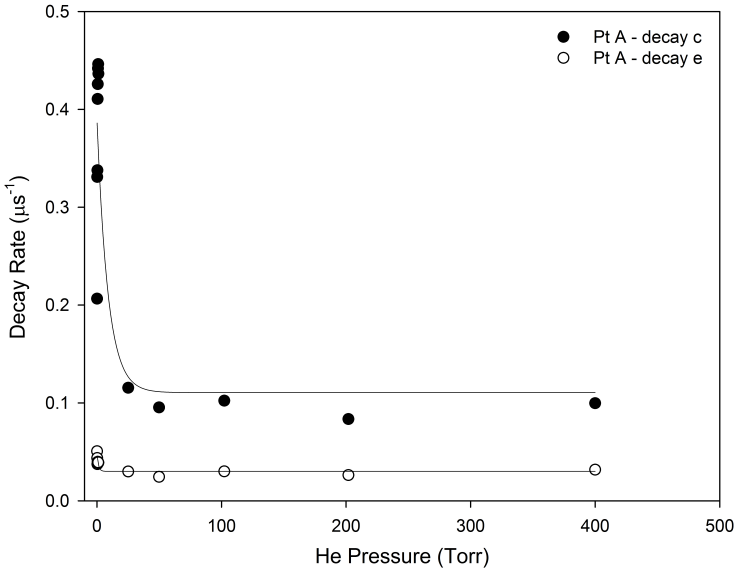

Figure 38. Decay rates c and e (from the double exponential fit function $y = a + b\exp(-cx) + d\exp(-ex)$) for probe frequency A are shown at moderate He pressures (0-400 Torr).

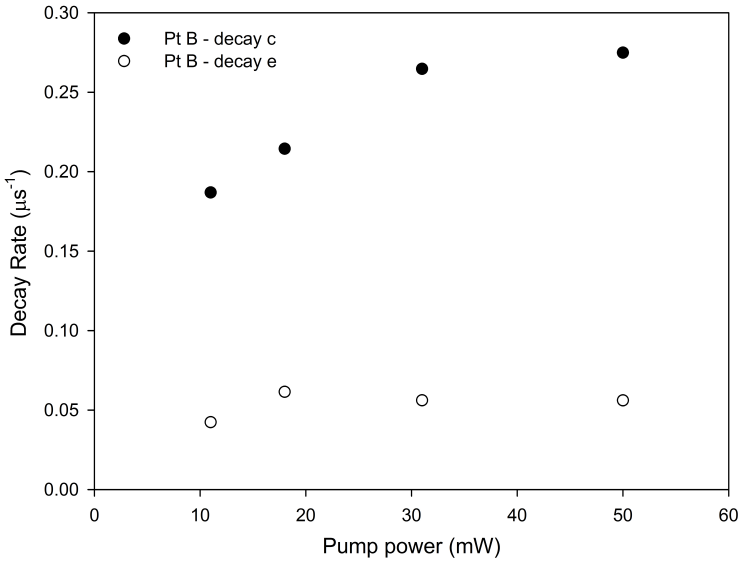

Figure 39. Decay rates c and e (from the double exponential fit function $y = a + b\exp(-cx) + d\exp(-ex)$) for probe frequency B are shown at low He pressures (0.06 Torr) at various pump powers.

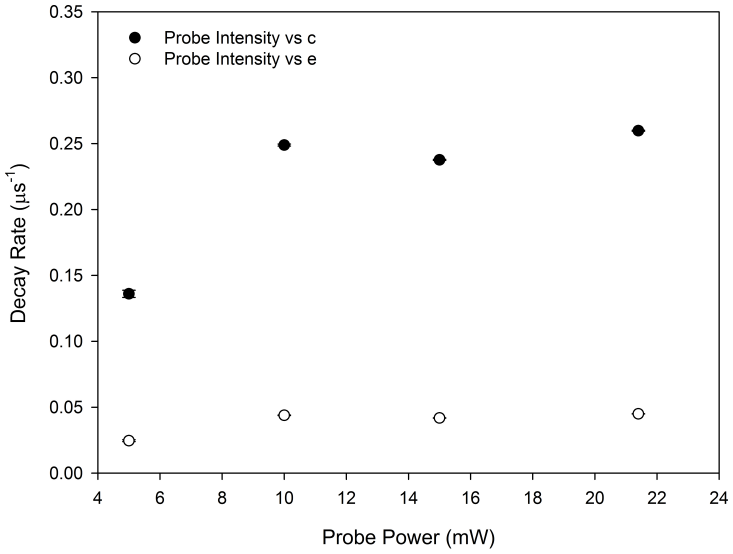

Figure 40. Decay rates c and e (from the double exponential fit function $y = a + b\exp(-cx) + d\exp(-ex)$) for probe frequency B are shown at low He pressures (0.05 Torr) at various probe powers.

dence was not evident. Decay rates were constant over useful range of probe powers sufficient to penetrate the optically thick alkali-metal vapor and produce detector signal outside noise limitations.

The full-frequency spectra of Figures 30 through 33 illustrate the pump pulse induced effect on hyperfine state excitation and relaxation return to equilibrium.

For short-term nanosecond scale effects, there are several potential explanations for the observed decrease in probe intensity at pump arrival including spatial variations in temperature, pressure caused by the pump laser inducing changes in the index of refraction reducing the probe beam incident on the detector, indicated by a rise to the long-term maximum on the time scale of the Cs D_2 lifetime sfter the pump pulse. To test this theory a fast frame rate (200k frames/second) camera was setup to capture images of probe spot movement as the 30-mW pump laser is focused through the alkali vapor cell at 80 °C as shown in Figure 41. Beam deflection was observed up to 1 mm at 60 cm after the alkali vapor cell, which would translate to over 3 mm

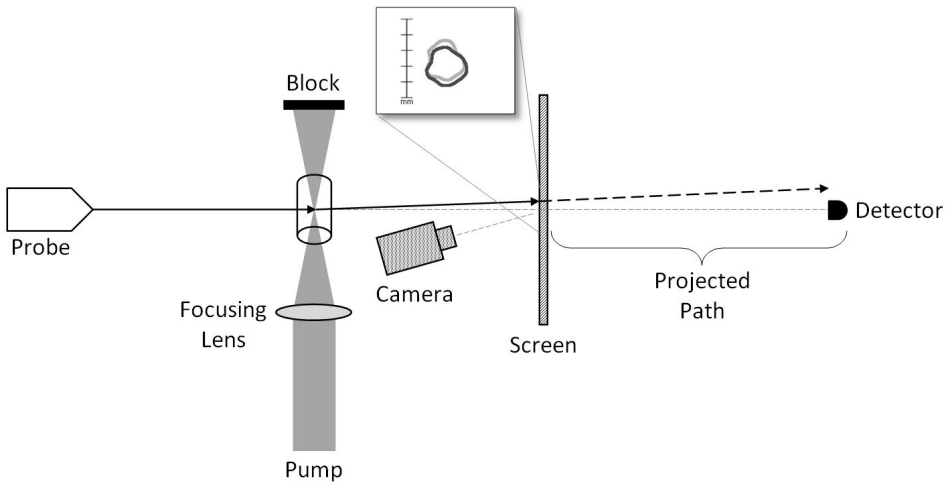

Figure 41. Experimental setup for beam steering observation. Movement of the probe beam is captured using a high speed (200k frame/second) camera as the pulsed pump beam is focused through the alkali-metal vapor cell.

deflection at the approximately 2-m path length used in the experimental setup depicted in Figure 27. In such cases the probe beam would be steered completely away from the 1 mm detector for deflections of this magnitude. Observed deflections lasted up to 100 µs. Deflections were most evident when the probe beam, detuned from cesium D_2 peak (-4 GHz), was closely aligned spatially to the tightly focused pump beam tuned to the D_2 peak absorption (+5 GHz). Repetition of the probe beam deflection roughly followed the 10-Hz pulsed pump rate, though deflection was not consistent in magnitude or direction from pulse to pulse. This may have resulted from inconsistent pulse-to-pulse pump intensity or frame synchronization artifacts as well as physical variations within the vapor cell.

Frequency dependence of the absorption shows there is a hyperfine component to the decay rate's return to equilibrium. In the cases illustrated the $F' = 5$ upper state, the primary transition for frequency point B, is electronically forbidden from the $F'' = 3$ pump tuning. The deviation of the point B excitation and decay from the other frequency regions is expected.

Temperature and He pressure dependence is predicted as the total Voigt lineshape broadening increases transfer between upper state components. The $F' = 4 \rightarrow F' = 5$ energy separation is only 251 MHz. At 90 °C the Doppler-dominated Voigt FWHM is 420 MHz. Over the range of temperatures used in this experiment the Voigt FWHM ranges from 410 MHz to 440 MHz at 0 Torr He.

Pressure broadening with He has a pronounced effect on the total broadening of the hyperfine lines. At low pressures the homogeneous broadening is natural broadening limited at 5.25 MHz. As pressure increases to 0.24 Torr the pressure induced broadening is equal to the natural linewidth. By 18.6 Torr He at 90 °C the total homogeneous broadening exceeds the Doppler-broadening and the total Voigt broadening is 680 MHz. The total separation of the Cs $^2P_{3/2}$ upper state is 603 MHz. Laser excitation should be well mixed and the frequency dependence is reduced. Therefore the asymptotic relaxation rates at high He pressures is expected as depicted in Figure 35 where the c decay rates for points A and B quickly reach a common constant value.

Low pressure response shows decay rates initially increase due to He pressure before attaining the pressure-broadened asymptotic constant showing that He helps the energy transfer return to equilibrium before the states are sufficiently pressure broadened.

It is therefore beneficial to examine the effect at low He pressures at various temperatures. Temperature has little effect on Doppler broadening over the range used in this experiment. However the concentration of alkali-metal vapor atoms varies exponentially with temperature above the room temperature melting point. Collisions between Cs-Cs are rare at 93 °C where the number density is 1.0×10^{12} atoms/cm^3 and 2.2×10^{13} atoms/cm^3 by 105 °C. Cesium-cesium collisional broadening is less then natural broadening until approximately 120 °C. As evidenced by the change in decay rate as a function of temperature as shown in Figure 36 temperature effects the data fit decay rates as the double-exponential decay becomes a single-exponential

decay. This suggests that decay rates trend toward a single dominant hyperfine relaxation process. At low temperatures at least two processes are present in the decay which could be representative of Cs-wall collisions or Cs-Cs interactions.

VII. Conclusion

A hyperfine structure cross section model was created to generate simulated absolute absorption coefficients for cesium and rubidium. The absorption coefficients were used to predict group velocity and group delay used a Kramers-Kronig delay model and the predicted delays were validated by measuring pulse delays across the Cs D_1 and Cs D_2 spectra.

Tunable slow light delays are demonstrated through frequency modulation of a single probe laser across the hyperfine structure of an alkali metal vapor. Delays of 0 ns to 37 ns have been observed in a single pass through a 5 cm cesium cell at 137.2 °C by detuning from resonance ±25 GHz. Predicted delays closely match calculations from an absorption profile model including Voigt lineshapes and full hyperfine structure. Frequency dependence of the delays are sensitive to vapor pressure and Doppler broadening, constraining vapor temperature uncertainties to about 0.1 °C. Additionally temporal delay of pulses using a gated camera demonstrated the pulse delay effect in an image.

Tuning of optical pulse delays obtained in the hyperfine doublet structure for the alkali atoms may be achieved through frequency modulation. Indeed, delays of 0 ns to 37 ns have been observed in a single pass through a 5-cm Cs cell at 137.2 °C by detuning from resonance 25 GHz. Delay predictions are nearly exact when the modeling precisely matches the absorption profile including Voigt lineshapes and full hyperfine structure. The frequency dependence of the delays are sensitive to vapor pressure, constraining cell temperature uncertainties to about 0.1 °C. Using the Voigt profile and hyperfine structure allows for accurate prediction of the pulse delay achieved by frequency tuning.

The frequency dependence of the optical pulse delay in cesium D_1 closely match the previously developed model predictions using Voigt lineshapes and the full hyper-

fine structure. The observed D_1 optical pulse delays compared favorably to similar results in Cs D_2. The delay prediction Kramers-Kronig model accurately predicts the delays between D_1 upper state hyperfine components at lower temperatures than previously reported with smaller frequency sampling separation. Delays up to 24 ns where achieved by detuning from resonance by 10 GHz.

Spectral hole burning produced optical delays in Cs D_1 pulses by varying D_2 pump laser power. Increasing D_2 pump power reduced D_1 absorption overall. Observation of hole burning effects on delay close to the spectral hole were noted. Location of the holes and predicted delay from a modified absorption spectrum matched model predictions. For a pump intensity of four times saturation intensity I_{sat} observed delay is reduced by an average of 50% across the spectrum and reaches a maximum of 78% in a narrow 110 MHz spectral hole region.

Hyperfine relaxation and temporal dynamics were examined in a cesium vapor cell. Short-term nanosecond scale pump effects and long-term microsecond scale relaxation of hyperfine populations were observed. Temperature and helium pressure-dependent absorption features were noted.

Fundamental understanding of pulse delays may lead to the development of practical all-optical delays for optical communication systems, improved interferometry instruments, remote sensing techniques and analytic devices. Exploration of the temporal dynamics in alkali-metal vapors is crucial to the optimization of scalable pumped DPAL systems.

Appendix A. Physical Constants

Table 3. Physical constants[†]

Symbol	Description	Value/Units
α_{fs}	Fine-structure constant	$1/137.035\,999\,679(94)$
c	Speed of light in vacuum	$299\,792\,458\,\mathrm{m\,s^{-1}}$
h	Planck constant	$6.626\,068\,96(33) \times 10^{-34}\,\mathrm{J\,s}$
		$4.135\,667\,33(10) \times 10^{-15}\,\mathrm{eV\,s}$
$\hbar$	Planck constant / 2π	$1.054\,571\,628(53) \times 10^{-34}\,\mathrm{J\,s}$
		$6.582\,118\,99(16) \times 10^{-16}\,\mathrm{eV\,s}$
k_B	Boltzmann constant	$1.380\,650\,4(24) \times 10^{-23}\,\mathrm{J\,K^{-1}}$
		$8.617\,343(15) \times 10^{-5}\,\mathrm{eV\,K^{-1}}$
ϵ_0	Permittivity (Electric constant)	$8.854\,187\,817 \times 10^{-12}\,\mathrm{F\,m^{-1}}$
μ_0	Permeability (Magnetic constant)	$12.566\,370\,614 \times 10^{-7}\,\mathrm{N\,A^{-2}}$
e	Elementary charge	$1.602\,176\,487(40) \times 10^{-19}\,\mathrm{C}$
m_e	Electron mass	$9.109\,382\,15(45) \times 10^{-31}\,\mathrm{kg}$
m_p	Proton mass	$1.672\,621\,637(83) \times 10^{-27}\,\mathrm{kg}$
m_u	Atomic mass constant	$1.660\,538\,782(83) \times 10^{-27}\,\mathrm{kg}$
atm	Standard atmosphere	$101\,325\,\mathrm{Pa} = 760\,\mathrm{Torr}$

[†] NIST 2006 CODATA recommended values

Appendix B. Cesium Data

Physical Properties

Table 4. Cesium (Cs) physical properties

Property	Symbol	Value
Atomic number†	Z	55
Total nucleons†	$Z + N$	133
Ground state†	—	$6s^2S_{1/2}$
Relative natural abundance†	$\eta(^{133}Cs)$	100%
Atomic mass†	m	132.905 452(1) u
Melting point‡	T_m	28.44 °C
Boiling point‡	T_b	671.0 °C
Density (solid)‡	ρ	1879 kg m^{-3}
Nuclear spin†	I	7/2
Magnetic moment	μ	+2.579
Ionization energy†	E_I	3.893 90(2) eV

† NIST "Chemistry Webbook." 2005

‡ Winter, M. "WebElements." 2008

Cesium Vapor Pressure

Cesium vapor pressure, in atmospheres, and Figure 42 are derived from Equation (104) (Alcock et al., 1984) where temperature T (K) is between melting point and 550 K. Number density derived from Equation (104) and the ideal gas las is shown in Figure 43.

$$\log_{10} P_V = 8.232 - 4062T^{-1} - 1.3359 \log_{10} T \tag{104}$$

Cesium D Line Optical Properties

D_1 optical properties are listed in Table 5 and illustrated in Figure 44.

D_2 optical properties are listed in Table 6 and illustrated in Figure 45.

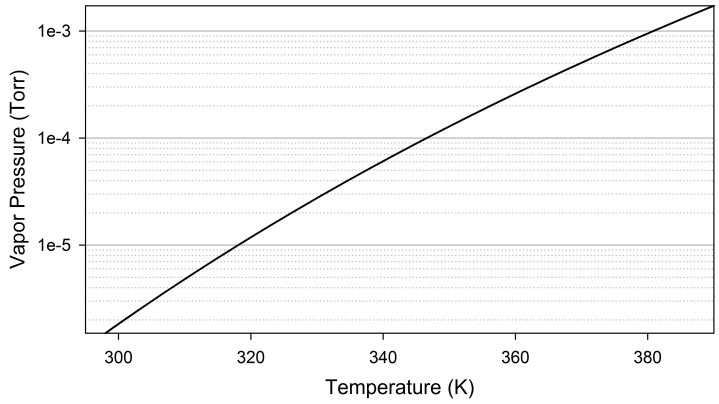

Figure 42. Cesium vapor pressure as given by equation (104) Alcock et al. (1984).

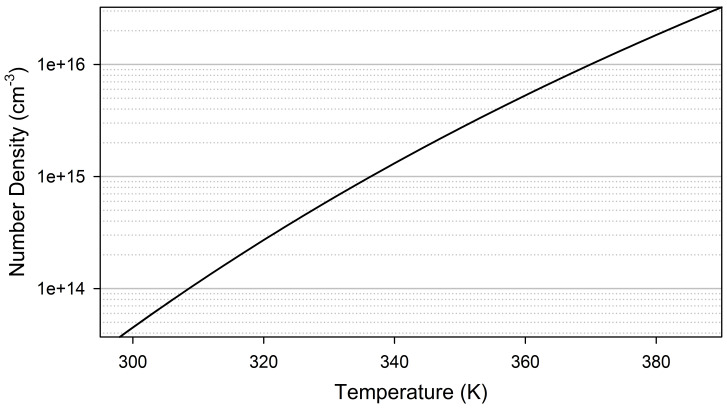

Figure 43. Cesium number density derived from equation (104) Alcock et al. (1984).

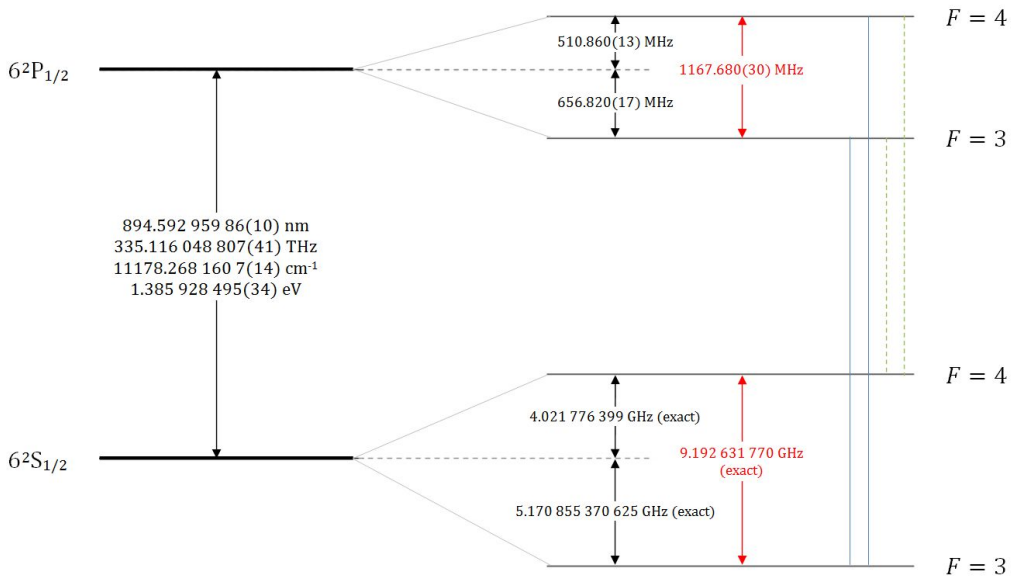

Figure 44. Cesium D_1 ($6^2S_{1/2} \rightarrow 6^2P_{1/2}$) hyperfine energy level splitting. Hyperfine splitting not drawn to scale. Relative splitting is only accurate for each hyperfine level.

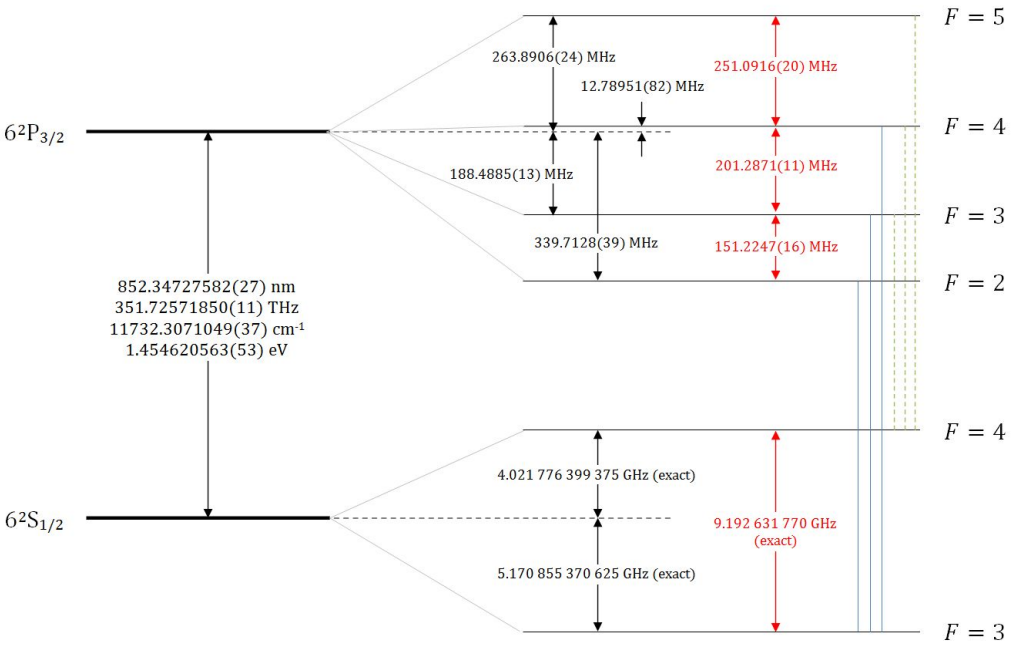

Figure 45. Cesium D_2 ($6^2S_{1/2} \rightarrow 6^2P_{3/2}$) hyperfine energy level splitting. Hyperfine splitting not drawn to scale. Relative splitting is only accurate for each hyperfine level.

Table 5. Cesium D_1 ($6^2\mathbf{S}_{1/2} \rightarrow 6^2\mathbf{P}_{1/2}$) transition optical properties(Steck, 2009)

Property	Symbol	Value
Frequency	ν_0	335.116 048 807(41) THz
Energy	$h\nu_0$	1.385 928 495(34) eV
Wavelength	λ	894.592 959 86(10) nm
Lifetime	τ	34.791(90) ns
Decay Rate	Γ	$28.743(75) \times 10^6\,\mathrm{s}^{-1}$
Natural Line Width (FWHM)		4.575(12) MHz
Absorption Oscillator Strength	f	0.3449(26)

Table 6. Cesium D_2 ($6^2\mathbf{S}_{1/2} \rightarrow 6^2\mathbf{P}_{3/2}$) transition optical properties(Steck, 2009)

Property	Symbol	Value
Frequency	ν_0	351.725 718 50(11) THz
Energy	$h\nu_0$	1.454 620 563(35) eV
Wavelength	λ	852.347 275 82(27) nm
Lifetime	τ	30.405(77) ns
Decay Rate	Γ	$32.889(84) \times 10^6\,\mathrm{s}^{-1}$
Natural Line Width (FWHM)		5.234(13) MHz
Absorption Oscillator Strength	f	0.7164(25)

Cesium D Line Hyperfine Energy Levels

$$\Delta E_{hfs} = \tfrac{1}{2}A_{hfs}K + B_{hfs}\frac{\frac{3}{2}K(K+1)-2I(I+1)J(J+1)}{4I(2I-1)J(2J-1)} + C_{hfs}\frac{5K^2(K/4+1)+K[I(I+1)+J(J+1)+3-3I(I+1)J(J+1)]-5I(I+1)J(J+1)}{I(I-1)(2I-1)J(J-1)(2J-1)} \tag{105}$$

where

$$K = F(F+1) - I(I+1) - J(J+1) \tag{106}$$

$A_{hfs} = magnetic\ dipole\ constant$

$B_{hfs} = electric\ dipole\ constant$

$C_{hfs} = magnetic\ octupole\ constant$

Table 7. Cesium D line magnetic and electric interaction constants(Steck, 2009).

	$\mathbf{6^2S_{1/2}}$	$\mathbf{6^2P_{1/2}}$	$\mathbf{6^2P_{3/2}}$
A_{hfs}	$h \cdot 2.298\,157\,942\,5$ GHz	$h \cdot 291.9201(75)$ MHz	$h \cdot 50.288\,27(23)$ MHz
B_{hfs}	—	—	$h \cdot -0.4934(17)$ MHz
C_{hfs}	—	—	$h \cdot 0.560(70)$ kHz

Cesium D Line Strength

Line strengths are determined using the $S_{F''\ F'}$ from (Steck, 2009, eqn (41), Tab 8).

$$S_{F''\ F'} = (2F'+1)(2J+1) \begin{Bmatrix} J & J' & 1 \\ F' & F'' & I \end{Bmatrix}^2 \tag{107}$$

$S_{F''\ F'}$ obeys the rule(Steck, 2009, eqn (42))

$$\sum_{F'} S_{F''\ F'} = 1 \tag{108}$$

Strength factor values can be determined using *Mathematica*'s `SixJSymbol` function and Equation (107).

Tables 8 and 9 catalog the transition line strength values for the cesium D_1 and

D_2 hyperfine lines.

Table 8. Cs D_1 ($6^2\mathbf{S}_{1/2} \rightarrow 6^2\mathbf{P}_{1/2}$) hyperfine transition strength factors(Steck, 2009).

Transition $S_{F'' \ F'}$	**Strength** (unitless)
$S_{4\ 4}$	5/12
$S_{4\ 3}$	7/12
$S_{3\ 4}$	3/4
$S_{3\ 3}$	1/4

Table 9. Cs D_2 ($6^2\mathbf{S}_{1/2} \rightarrow 6^2\mathbf{P}_{3/2}$) hyperfine transition strength factors(Steck, 2009).

Transition $S_{F'' \ F'}$	**Strength** (unitless)
$S_{4\ 5}$	11/18
$S_{4\ 4}$	7/24
$S_{4\ 3}$	7/72
$S_{3\ 4}$	15/56
$S_{3\ 3}$	3/8
$S_{3\ 2}$	5/14

Buffer Gas Pressure Effects

Pressure effects vary by buffer gas type and pressure. The line is broadened as well as shifted in frequency. Table 10 shows the frequency shift and line width effects on the cesium D_1 and D_2 lines due to nitrogen and helium buffer gases.

Pressure effects must also be corrected for temperature. Given the data was taken at $T_{data} = 294.15\,\mathrm{K}$, the buffer gas pressure effects on system at temperature T_{sys}, in

Table 10. Pressure broadening and shift of cesium D line due to buffer gases(Andalkar and Warrington, 2002). Data was taken at 294.15 K

Buffer Gas	**Measured Quantity**	**Value** ($\mathrm{MHz\,Torr^{-1}}$)
N_2	D_1 width	19.51
N_2	D_1 shift	−8.23
N_2	D_2 width	22.68
N_2	D_2 shift	−6.73
He	D_1 width	26.21
He	D_1 shift	4.46
He	D_2 width	23.50
He	D_2 shift	0.75

K, and buffer gas pressure P_i, in Torr by

$$\Delta\nu_L = \frac{1}{2\pi}\left(\frac{1}{\tau_r}\right) + \sum_i \gamma_i \left(\frac{T_{sys}}{T_{data}}\right)^{1/2} P_i \tag{109}$$

$$\nu_0 \to \nu_0 + \sum_i \delta_i \left(\frac{T_{sys}}{T_{data}}\right)^{1/2} \tag{110}$$

where $\Delta\nu_L$ is the Lorentzian line width, and ν_0 is the center frequency for each hyperfine line.

Appendix C. Matlab® Code

Cesium D_2 Absorption Coefficient

The calculated absorption coefficient compares favorably to experimentally determined Cs absorption as shown in Figure 12 in Chapter IV Delay Prediction.

```
function [abs] = fnAbsCoeffCsD2(freq,T,PN2,PHe,PCH4)
%-------------------------------------------------------------------------
% Monte D. Anderson
% Department of Engineering Physics, Air Force Institute of Technology
% 19 Mar 2010
%-------------------------------------------------------------------------
% Calculates cesium D2 absorption coefficent (1/cm) at a given frequency
% at temperature T (K) and buffer gas pressures PN2, PHe, and PCH4 (Torr)
%-------------------------------------------------------------------------

%% CONSTANTS
global c eo h hbar kB AMU;
global AmCs MCs Inam vo tau;
global TransM numTrans;
global dvS12 s0 vD2;

% Physical Constants (NIST 2006 CODATA Internationally recommended values)
% http://physics.nist.gov/cuu/Constants/index.html
c = 2.99792458e8;           % vacuum speed of light (m/s)
eo = 8.85418781762e-12;     % vacuum permittivity (F/m)
h = 6.62606896e-34;         % Planck const (Js)
hbar = 1.054571628e-34;     % Planck const/2pi (Js)
kB = 1.3806504e-23;         % Boltzmann const (J/K)
AMU = 1.660538782e-27;      % Atomic Mass Unit (kg)

% Cesium Atomic Data
AmCs = 132.905451931;       % Atomic mass (AMU)
MCs = AmCs*AMU;             % Mass of Cs atom (kg)
Inam = 7/2;                 % Total nuclear angular momentum

% Cs D2 Data
vo = 351.72571850e12;       % Frequency (Hz)
tau = 30.32e-9;             % Lifetime (s)                          REF [1]
%-------------------------------------------------------------------------
% REFERENCE:
%   [1] J. M. Amini and H. Gould
%      High Precision Measurement of the Static Dipole Polarizability of Cs
%      Phys. Rev. Lett., American Physical Society, 2003, 91, 153001
%-------------------------------------------------------------------------
% Transition Matrix, contains allowed transitions and pertenent quantum
%   numbers in the format (Inam, Jupper, Flower, Fupper)
```

```
% NOTE: Jlower is 1/2 (ground state)
% NOTE: Inam is the same for all transitions in Cs.  This function was
%   built to accomdate elements with multiple isotopes like Rubidium.
TransM = [7/2 3/2 3 2;
          7/2 3/2 3 3;
          7/2 3/2 3 4;
          7/2 3/2 4 3;
          7/2 3/2 4 4;
          7/2 3/2 4 5];
numTrans = length(TransM);

%% Hyperfine Structure Energy Levels
vD2 = zeros(1,numTrans);
for j = 1:numTrans
    vD2(j) = (hfsEnergy(TransM(j,1),1,TransM(j,2),TransM(j,4))/h)-...
        (hfsEnergy(TransM(j,1),0,1/2,TransM(j,3))/h);
end
dvS12 = hfsEnergy(Inam,0,1/2,4)/h - hfsEnergy(Inam,0,1/2,3)/h;

%% Line Strength Factors, SFF
SFF = zeros(1,numTrans);
for n = 1:numTrans
    SFF(n) = S_fun(TransM(n,3),TransM(n,4),0.5,TransM(n,2),TransM(n,1));
end

%% Cross Section at Line Center (sigma_0)
s0 = zeros(1,numTrans);
for f = 1:numTrans
    s0(f) = sigma_0(SFF,vD2,f);
end

%% main function output
abs = NumDensity(T)*CrossSection(freq,T,PN2,PHe,PCH4);

end    %end of fnAbsCoeffCsD2 main function ------------------------------


%--------------------------------------------------------------------------
%% fnAbsCoeffCsD2 SUBFUNCTIONS

%% HYPERFINE ENERGY LEVELS -------------------------------------------------
function [dEhfs] = hfsEnergy(Inam,L,J,F)
% Calculates hyperfine structure energy
%--------------------------------------------------------------------------
% REFERENCES:
%   [2] E.Arimondo, M.Inguscio, and P.Violino
%       "Experimental determinations of the hyperfine structure...
%        ...in the alkali atoms"
%       Rev. Mod. Phys., American Physical Society, 1977, 49, 31-75
%
%   [3] V.Gerginov, A.Derevianko, and C.E.Tanner
%       "Observation of the Nuclear Magnetic Octupole Moment of Cs133"
```

```
94 %       Phys. Rev. Lett., American Physical Society, 2003, 91, 072501
95 %--------------------------------------------------------------------------
96 global h;
97
98 %Constants
99 AS12 = h*2.2981579425*1E9;      %(Hz)
100 AP12 = h*291.9201*1E6;          %(Hz)
101 AP32 = h*50.28827*1E6;          %(Hz)
102 BP32 = h*-0.4934*1E6;           %(Hz)
103 CP32 = h*0.560*1E3;             %(Hz)
104
105 K = F*(F + 1) - Inam*(Inam + 1) - J*(J + 1);
106
107 if(L == 0)
108     dEhfs = .5*AS12*K;
109 elseif(L == 1 && J == .5)
110     dEhfs = .5*AP12*K;
111 elseif(L == 1 && J == 1.5)
112     dEhfs = (.5*AP32*K) + BP32*((1.5*K*(K+1) -...
113        2*Inam*(Inam+1)*J*(J+1))/(4*Inam*(2*Inam-1)*J*(2*J-1))) +...
114        CP32*(5*(K^2)*((K/4)+1) +...
115        K*(Inam*(Inam+1) + J*(J+1) + 3 - 3*Inam*(Inam+1)*J*(J+1)) -...
116        5*Inam*(Inam+1)*J*(J+1))/(Inam*(Inam-1)*(2*Inam-1)*J*(J-1)*(2*J-1));
117 else
118     fprintf('\nIMPROPER INPUTS\n\n')
119     dEhfs = 0;
120 end
121
122 end
123
124 %% LINE STRENGTH FACTORS ------------------------------------------------
125 function [S] = S_fun(F,Fprime,J,Jprime,I)
126 S1 = Wigner6j(J,Jprime,1,Fprime,F,I);
127 S = (2*Fprime+1)*(2*J+1)*(S1^2);
128 end
129
130 %% WIGNER 6j FACTORS ----------------------------------------------------
131 function Wigner = Wigner6j(j1,j2,j3,J1,J2,J3)
132 % Wigner 6j-symbol calculator. Written by Amita B Deb, Clarendon Lab. 2007.
133 % Improved by Richard A. Holt, Univ. of Western Ontario, 2009.
134 % Further improved to deal with large input arguments by Lee Harper,
135 %   CRL Oxford, 2009.
136
137 % Builds on the m-file Wigner6jcoeff posted by Richard A. Holt.
138
139 % Calculates { j1, j2 ,j3}  using Racah formula.
140 %             J1  J2  J3
141 %--------------------------------------------------------------------------
142 % REFERENCE:
143 %   [4] I.I.Sobelman
144 %       Atomic Spectra and Radiative Transitions
145 %       Springer Series in Chemical Physics, Vol. 1, Springer (June 1979)
```

```
146 %-------------------------------------------------------------------------
147 % Finding Triangular coefficients
148 tri1 = triangle_coeff(j1,j2,j3);
149 tri2 = triangle_coeff(j1,J2,J3);
150 tri3 = triangle_coeff(J1,j2,J3);
151 tri4 = triangle_coeff(J1,J2,j3);
152
153 if (tri1==0||tri2==0||tri3==0||tri4==0)
154     Wigner=0;
155     return
156 end
157
158 % Finding the range of summation in the Racah formula.
159 a(1) = j1 + j2 + j3;
160 a(2) = j1 + J2 + J3;
161 a(3) = J1 + j2 + J3;
162 a(4) = J1 + J2 + j3;
163
164 rangei = max(a);
165
166 k(1) = j1 + j2 + J1 + J2;
167 k(2) = j2 + j3 + J2 + J3;
168 k(3) = j3 + j1 + J3 + J1;
169
170 rangef = min(k);
171
172 Wigner = 0;
173
174    for t=rangei:rangef
175         Wigner = Wigner + ((-1)^t)*exp(gammaln(t+2) -...
176           fung(t,j1,j2,j3,J1,J2,J3));
177    end
178
179    Wigner = (tri1*tri2*tri3*tri4)^(0.5)*Wigner;
180
181 end
182
183 % ----- Wigner6j subfunctions ---------------------------------------------
184
185 function r = fung(t, j1,j2,j3,J1,J2,J3)
186 % Calculating the logarithm of the denominator in Racah Formula, using
187 % the gamma function in place of the factorial.
188 r = sum(gammaln([(t-j1-j2-j3);(t-j1-J2-J3);(t-J1-j2-J3);(t-J1-J2-j3);...
189                  (j1+j2+J1+J2-t);(j2+j3+J2+J3-t);(j3+j1+J3+J1-t)] + 1));
190 end
191
192 %-------------------------------------------------------------------------
193 function tri = triangle_coeff(a,b,c)
194 % Calculates triangle coefficients for angular momenta.
195 % This version returns 0 if the triangle inequalities are violated.  (RAH)
196
197 if (a<0 || b<0 || c<0)
```

```
198     tri=0;
199     return
200 end
201
202 for xa = abs(a-b):1:a+b
203     if c==xa
204         tri = factorial(a+b-c)*factorial(a-b+c)*...
205             factorial(-a+b+c)/(factorial(a+b+c+1));
206         return
207     end
208 end
209
210 tri=0;
211
212 end
213
214 %% CROSS SECTION AT LINE CENTER ----------------------------------------
215 function [s0] = sigma_0(SFF,vD,x)
216 % Calculates cross section at line center for each hyperfine level.
217 global c vo tau TransM;
218
219 dvnat = 1/(2*pi*tau);   % natural linewidth
220
221 s0 = SFF(x)*(1/tau)*(((c*100)^2)/(8*pi))*(1/((vo+vD(x))^2))*...
222         ((2*TransM(x,2)+1)/(2*.5+1))*(2/(pi*dvnat));
223 end
224
225 %% NUMBER DENSITY ------------------------------------------------------
226 function [ndensity] = NumDensity(T)
227 % calculates number density (cm^-3) given Temperature (K) from ideal gas eq
228 global kB;
229
230 ndensity = (CsVaporPressure(T))/(kB*T)*101325*(1e-6);
231 end
232
233 %% VAPOR PRESSURE ------------------------------------------------------
234 function [Pv] = CsVaporPressure(T)
235 % Provides Cesium vapor pressure in atmospheres given Temperature (K)
236 %-------------------------------------------------------------------------
237 % REFERENCE:
238 %   [5] C.B.Alcock, V.P.Itkin, and M.K.Horrigan
239 %       Vapour pressure equations for the metallic elements: 298-2500K
240 %       Canadian Metallurgical Quarterly, 1984, 23, 309-313
241 %-------------------------------------------------------------------------
242 % Uses "Precise" equation for Cs vapor pressure.
243 % Uses melting point for Cs at 301.59K (NIST value)
244 % Valid for temperatures from melting point to 550K (per Alcock et al).
245
246 if(T ≥ 301.59 && T ≤ 550)
247     a = 8.232;
248     b = -4062;
249     c = -1.3359;
```

```
250 elseif(T < 301.59 || T > 550)
251     fprintf('\nTemperature is outside of allowed range.\n\n')
252     return
253 end
254 Pv = 10.^(a + b*(T^-1) + c*log10(T));
255 end
256 
257 %% CROSS SECTION ------------------------------------------------------------
258 function [cs] = CrossSection(x,T,PN2,PHe,PCH4)
259 % calculates cross section as function of frequency, x
260 global tau s0 vo TransM vD2;
261 
262 dvnat = 1/(2*pi*tau);
263 [gamma,shift,dvD,dvL] = BufferGas(T,PN2,PHe,PCH4);
264 
265 cs = (dvnat*pi/2)*(...
266     BoltzRatio(TransM(1,3),T)*s0(1)*...
267         ((x+vD2(1)+shift+vo)/(vD2(1)+shift+vo))*...
268         gVoigt((x-vD2(1)),dvL,dvD)+...
269     BoltzRatio(TransM(2,3),T)*s0(2)*...
270         ((x+vD2(2)+shift+vo)/(vD2(2)+shift+vo))*...
271         gVoigt((x-vD2(2)),dvL,dvD)+...
272     BoltzRatio(TransM(3,3),T)*s0(3)*...
273         ((x+vD2(3)+shift+vo)/(vD2(3)+shift+vo))*...
274         gVoigt((x-vD2(3)),dvL,dvD)+...
275     BoltzRatio(TransM(4,3),T)*s0(4)*...
276         ((x+vD2(4)+shift+vo)/(vD2(4)+shift+vo))*...
277         gVoigt((x-vD2(4)),dvL,dvD)+...
278     BoltzRatio(TransM(5,3),T)*s0(5)*...
279         ((x+vD2(5)+shift+vo)/(vD2(5)+shift+vo))*...
280         gVoigt((x-vD2(5)),dvL,dvD)+...
281     BoltzRatio(TransM(6,3),T)*s0(6)*...
282         ((x+vD2(6)+shift+vo)/(vD2(6)+shift+vo))*...
283         gVoigt((x-vD2(6)),dvL,dvD));
284 end
285 
286 %% BUFFER GAS EFFECTS -------------------------------------------------------
287 function [gamma,shift,dvD,dvL] = BufferGas(T,PN2,PHe,PCH4)
288 % Cs D2 buffer gas effects, including broadening and frequency shift
289 % OUTPUT:   gamma   pressure broadening due to buffer gas
290 %           shift   frequency shift due to buffer gas
291 %           dvD     Doppler broadening
292 %           dvL     Lorentzian homogeneous broadening (natural + pressure)
293 %-------------------------------------------------------------------------
294 % REFERENCES:
295 %   [6] A.Andalkar and R.B.Warrington
296 %       High-resolution measurement of the pressure broadening and shift
297 %           of the Cs D1 and D2 lines by N2 and He buffer gases
298 %       Phys. Rev. A 65, 032708 (2002)
299 %
300 %   [7] G. Pitz, D. Wertepny, and G. Perram
301 %       Pressure broadening and shift of the cesium D1 transition by the
```

```
302 %           noble gases and N2, H2, HD, D2, CH4, C2H6, CF4, and 3He
303 %       Phys. Rev. A 80, 062718 (2009)
304 %--------------------------------------------------------------------------
305 % Pressure broadening coefficients are temperature dependent such that
306 %   (gamma or shift)*((T/Tdata)^(1/2))*Pressure
307 % where
308 %   gamma or shift are the broadening or shift values (MHz/Torr)
309 %   T is the current temperature
310 %   Tdata is the temperature at which buffer gas values were measured
311 %
312 % Pressure effect values and Tdata below are taken from reference [2].
313
314 global tau c kB MCs vo;
315
316 gamma = (19.18e6)*((T/313)^(1/2))*PN2 ...
317     + (20.59e6)*((T/313)^(1/2))*PHe...
318     + (25.84e6)*((T/313)^(1/2))*PCH4;
319 shift = (-6.2e6)*((T/313)^(1/2))*PN2...
320     + (0.69e6)*((T/313)^(1/2))*PHe...
321     + (-8.86e6)*((T/313)^(1/2))*PCH4;
322
323 dvD = (vo + shift)*((8*kB*T*log(2))/(MCs*(c^2)))^(1/2);
324 dvL = (1/(2*pi*tau)) + gamma;
325 end
326
327 %% BOLTZMAN RATIO ---------------------------------------------------------
328 function [BR] = BoltzRatio(F,T)
329 % Calculates relative Boltzman distribution of ground state energy levels.
330 global kB h dvS12;
331
332 if(F == 3)
333     BR = 7./(7 + 9*exp(-(h*dvS12)./(kB.*T)));
334 elseif(F == 4)
335     BR = (9*exp(-(h*dvS12)./(kB.*T)))./(7 + 9*exp(-(h*dvS12)./(kB.*T)));
336 elseif(F ~= 3 && F ~= 4)
337     fprintf('\nIMPROPER INPUTS\n\n')
338     BR = 0;
339 end
340 end
341
342 %% VOIGT LINESHAPE --------------------------------------------------------
343 function [y] = gVoigt(v,dvL,dvD)
344 % A useful approximation for the Voigt convolution is given by Thompson
345 %--------------------------------------------------------------------------
346 % REFERENCE:
347 %   [8] William J. Thompson
348 %       Numerous neat algorithms for the Voigt profile function.
349 %       Computers in Physics, Vol 7, No. 6, Nov/Dec 1993.
350 %--------------------------------------------------------------------------
351 %   gV(u,a) = Re[Exp(z^2)erfc(z)]
352 %       z = a + iu
353 %       a = sqrt(ln(2)) vLorentzian/vDoppler
```

```
354 %       u = 2 sqrt(ln(2)) (v-vo)/vDoppler
355
356 % NOTE: Not valid for Doppler free spectra where vDoppler = 0
357 % NOTE: erfc(z) = 1 - erf(z) (related to the Faddeeva function)
358
359 a = sqrt(log(2))*(dvL/dvD);
360 u = 2*sqrt(log(2))*(v/dvD);
361 z = a + 1i*u;
362 y = 2*sqrt(log(2)/pi)*(1/dvD)*real(faddeeva(1i*z));
363 end
364
365 % ----- gVoigt subfunctions ---------------------------------------------
366
367 function w = faddeeva(z,N)
368 %-------------------------------------------------------------------------
369 % http://www.mathworks.com/matlabcentral/fileexchange/...
370 %      ...22207-faddeeva-function-fft-based
371 % Posted by Kesh (tikuma@lsu.edu) - 21 Nov 2008 (Updated 19 Feb 2009)
372 %-------------------------------------------------------------------------
373 % FADDEEVA   Faddeeva function
374 %   W = FADDEEVA(Z) is the Faddeeva function, aka the plasma dispersion
375 %   function, for each element of Z. The Faddeeva function is defined as:
376 %
377 %     w(z) = exp(-z^2) * erfc(-j*z)
378 %
379 %   where erfc(x) is the complex complementary error function.
380 %
381 %   W = FADDEEVA(Z,N) can be used to explicitly specify the number of terms
382 %   to truncate the expansion (see (13) in [1]). N = 16 is used as default.
383 %
384 %   Example:
385 %       x = linspace(-10,10,1001); [X,Y] = meshgrid(x,x);
386 %       W = faddeeva(complex(X,Y));
387 %       figure;
388 %       subplot(121); imagesc(x,x,real(W)); axis xy square; caxis([-1 1]);
389 %       title('re(faddeeva(z))'); xlabel('re(z)'); ylabel('im(z)');
390 %       subplot(122); imagesc(x,x,imag(W)); axis xy square; caxis([-1 1]);
391 %       title('im(faddeeva(z))'); xlabel('re(z)'); ylabel('im(z)');
392 %-------------------------------------------------------------------------
393 % Reference:
394 %   [9] J.A.C. Weideman, "Computation of the Complex Error Function," SIAM
395 %       J. Numerical Analysis, pp. 1497-1518, No. 5, Vol. 31, Oct., 1994
396 %       Available Online: http://www.jstor.org/stable/2158232
397 %-------------------------------------------------------------------------
398 if nargin<2, N = []; end
399 if isempty(N), N = 16; end
400
401 w = zeros(size(z)); % initialize output
402
403 %%%%%
404 % for purely imaginary-valued inputs, use erf as is if z is real
405 idx = real(z)==0; %
```

```
406 w(idx) = exp(-z(idx).^2).*erfc(imag(z(idx)));
407
408 if all(idx), return; end
409 idx = ¬idx;
410
411 %%%%%
412 % for complex-valued inputs
413
414 % make sure all points are in the upper half-plane (positive imag. values)
415 idx1 = idx & imag(z)<0;
416 z(idx1) = conj(z(idx1));
417
418 M = 2*N;
419 M2 = 2*M;
420 k = (-M+1:1:M-1)'; % M2 = no. of sampling points.
421 L = sqrt(N/sqrt(2)); % Optimal choice of L.
422
423 theta = k*pi/M;
424 t = L*tan(theta/2); % Variables theta and t.
425 f = exp(-t.^2).*(L^2+t.^2);
426 f = [0; f]; % Function to be transformed.
427 a = real(fft(fftshift(f)))/M2; % Coefficients of transform.
428 a = flipud(a(2:N+1)); % Reorder coefficients.
429
430 Z = (L+1i*z(idx))./(L-1i*z(idx));
431 p = polyval(a,Z); % Polynomial evaluation.
432 w(idx) = 2*p./(L-1i*z(idx)).^2 + (1/sqrt(pi))./(L-1i*z(idx)); % Eval w(z).
433
434 % convert the upper half-plane results to the lower half-plane if necesary
435 w(idx1) = conj(2*exp(-z(idx1).^2) - w(idx1));
436
437 end
```

Absorption Coefficient Changes for Cs D_1

The previous MATLAB® code example can be easily modified for cesium D_1 or any other atomic species with a single isotope. To change the MATLAB® absorption coefficient function on page C for cesium D_1, make the following modifications at the appropriate places within the code. To modify use of this code for other atomic elements, be sure to modify vapor pressure and buffer gas effect functions.

```
% Cs D1 Data
vo = 335.116048807e12;      % Frequency (Hz)
tau = 34.72e-9;             % Lifetime (s)
TransM = [7/2 1/2 3 3;
          7/2 1/2 3 4;
          7/2 1/2 4 3;
          7/2 1/2 4 4];
%hfsEnergy Constants...
AS12 = h*2.2981579425*1E9;      %(Hz)
AP12 = h*291.9201*1E6;          %(Hz)
AP32 = h*50.28827*1E6;          %(Hz)
BP32 = h*-0.4934*1E6;           %(Hz)
CP32 = h*0.560*1E3;             %(Hz)
%fnCrossSection.....
cs = (dvnat*pi/2)*(...
    BoltzRatio(TransM(1,3),T)*s0(1).*...
        ((x+vD1(1)+shift+vo)/(vD1(1)+shift+vo)).*...
        gVoigt((x-vD1(1)),dvL,dvD)+...
    BoltzRatio(TransM(2,3),T)*s0(2).*...
        ((x+vD1(2)+shift+vo)/(vD1(2)+shift+vo)).*...
        gVoigt((x-vD1(2)),dvL,dvD)+...
    BoltzRatio(TransM(3,3),T)*s0(3).*...
        ((x+vD1(3)+shift+vo)/(vD1(3)+shift+vo)).*...
        gVoigt((x-vD1(3)),dvL,dvD)+...
    BoltzRatio(TransM(4,3),T)*s0(4).*...
        ((x+vD1(4)+shift+vo)/(vD1(4)+shift+vo)).*...
        gVoigt((x-vD1(4)),dvL,dvD));
%BufferGasEffects...
gamma = (15.82e6)*((T/318)^(1/2))*PN2 ...
    + (24.13e6)*((T/323)^(1/2))*PHe...
    + (29.00e6)*((T/333)^(1/2))*PCH4;
shift = (-7.69e6)*((T/318)^(1/2))*PN2...
    + (4.24e6)*((T/323)^(1/2))*PHe...
    + (-9.28e6)*((T/333)^(1/2))*PCH4;
```

Cesium D_2 Hyperfine Energy Level

The following code sample is a code snippet that calculates the cesium D_2 hyperfine energy.

```
function [dEhfs] = hfsEnergy(Inam,L,J,F)
% Calculates hyperfine structure energy for Cs D2.  Given Inam, L, J and F
%   calculates the hyperfine energy difference.
%
% REFERENCES:
% Arimondo, E., Inguscio, M. and Violino, P.
% Experimental determinations of the hyperfine structure in the alkali atoms
% Rev. Mod. Phys., American Physical Society, 1977, 49, 31-75
%
% Gerginov, V.; Derevianko, A. & Tanner, C. E.
% Observation of the Nuclear Magnetic Octupole Moment of Cs133
% Phys. Rev. Lett., American Physical Society, 2003, 91, 072501
%
global h;

%Constants
AS12 = h*2.2981579425*1E9;      %(Hz)
AP12 = h*291.9201*1E6;          %(Hz)
AP32 = h*50.28827*1E6;          %(Hz)
BP32 = h*-0.4934*1E6;           %(Hz)
CP32 = h*0.560*1E3;             %(Hz)

K = F*(F + 1) - Inam*(Inam + 1) - J*(J + 1);

if(L == 0)
    dEhfs = .5*AS12*K;
elseif(L == 1 && J == .5)
    dEhfs = .5*AP12*K;
elseif(L == 1 && J == 1.5)
    dEhfs = (.5*AP32*K) + BP32*((1.5*K*(K+1) - ...
       2*Inam*(Inam+1)*J*(J+1))/(4*Inam*(2*Inam-1)*J*(2*J-1))) +...
       CP32*(5*(K^2)*((K/4)+1) + K*(Inam*(Inam+1) + J*(J+1) + 3 - ...
       3*Inam*(Inam+1)*J*(J+1)) -...
       5*Inam*(Inam+1)*J*(J+1))/(Inam*(Inam-1)*(2*Inam-1)*J*(J-1)*(2*J-1));
else
    fprintf('\nIMPROPER INPUTS\n\n')
    dEhfs = 0;
end

%end of function
```

Rubidium D_1 Absorption Coefficient

The absolute absorption of the rubidium D lines compares favorably to the theoretical and experimental results reported by Siddons *et al.*(Siddons et al., 2008).

```
function [abs] = fnAbsCoeffRbD1(freq,T,PHe,PCH4)
% Calculates rubidum D1 absorption coefficent (1/cm) at a given frequency
% at temperature T (K) and buffer gas pressures PHe and PCH4 (Torr)
%--------------------------------------------------------------------------
% Monte Anderson
% Air Force Institute of Technology, Department of Engineering Physics
%
% 27 Oct 2009
%==========================================================================

%% CONSTANTS
global c eo h hbar kB AMU;
global AmRb85 MRb85 Inam85 vo85 tau;
global AmRb87 MRb87 Inam87 vo87;
global TransM numTrans;
global dv85S12 dv87S12 s0 vHF;

% Physical Constants (NIST)
c = 2.99792458e8;           % vacuum speed of light (m/s)
eo = 8.85418781762e-12;     % vacuum permittivity (F/m)
h = 6.62606896e-34;         % Planck const (Js)
hbar = 1.054571628e-34;     % Planck const/2pi (Js)
kB = 1.3806504e-23;         % Boltzmann const (J/K)
AMU = 1.660538782e-27;      % Atomic Mass Unit (kg)

% Rubidium Atomic Data
AmRb85 = 84.911789732;      % Atomic mass (AMU) of Rb85
AmRb87 = 86.909180520;      % Atomic mass (AMU) of Rb87
MRb85 = AmRb85*AMU;         % Mass of Rb85 atom (kg)
MRb87 = AmRb87*AMU;         % Mass of Rb87 atom (kg)
Inam85 = 5/2;               % Total nuclear angular momentum Rb85
Inam87 = 3/2;               % Total nuclear angular momentum Rb87

% Rb D1 Data
vo85 = 377.107385690e12;    % Frequency (Hz) Rb85
vo87 = 377.1074633805e12;   % Frequency (Hz) Rb87
tau = 27.679e-9;           % Lifetime (s) Rb85 and Rb87

% REFERENCES


% Transition Matrix, contains allowed transitions and pertenent quantum
%   numbers in the format (Inam, Jupper, Flower, Fupper)
```

```
% NOTE: Jlower is 1/2 (ground state).
TransM = [5/2 1/2 2 2;
          5/2 1/2 2 3;
          5/2 1/2 3 2;
          5/2 1/2 3 3;
          3/2 1/2 1 1;
          3/2 1/2 1 2;
          3/2 1/2 2 1;
          3/2 1/2 2 2];
numTrans = length(TransM);

%% Hyperfine Structure - Transition Frequencies (from TransM)
vHF = zeros(1,numTrans);
for j = 1:numTrans
    vHF(j) = (hfsEnergyRb(TransM(j,1),1,TransM(j,2),TransM(j,4))/h)-...
       (hfsEnergyRb(TransM(j,1),0,1/2,TransM(j,3))/h) + dvIso(TransM(j,1));
end
dv85S12 = hfsEnergyRb(Inam85,0,1/2,3)/h - hfsEnergyRb(Inam85,0,1/2,2)/h;
dv87S12 = hfsEnergyRb(Inam87,0,1/2,2)/h - hfsEnergyRb(Inam87,0,1/2,1)/h;

%% Line Strength Factors, SFF
SFF = zeros(1,numTrans);
for n = 1:numTrans
    SFF(n) = S_fun(TransM(n,3),TransM(n,4),0.5,TransM(n,2),TransM(n,1));
end

%% Cross Section at Line Center (sigma_0)
s0 = zeros(1,numTrans);
for f = 1:numTrans
    s0(f) = sigma_0Rb(SFF,vHF,f);
end

%% main function output
abs = NumDensityRb(T)*CrossSectionRb(freq,T,PHe,PCH4);

end    %end of fnAbsCoeffRbD1 main function ----------------------------


%% fnAbsCoeffRbD1 SUBFUNCTIONS ==============================================


%% HYPERFINE ENERGY LEVELS ------------------------------------------------
function [dEhfs] = hfsEnergyRb(Inam,L,J,F)
% Calculates hyperfine structure energy for Rb D1 and D2.
%
% REFERENCES:
% Arimondo, E., Inguscio, M. and Violino, P.
% Experimental determinations of the hyperfine structure inthe alkali atoms
% Rev. Mod. Phys., American Physical Society, 1977, 49, 31-75
%
global h Inam85 Inam87;
```

```
96
97  %Constants Rb85
98  A85S12 = h*1.0119108130e9;          %(Hz)
99  A85P12 = h*120.527e6;               %(Hz)
100 A85P32 = h*25.0020e6;               %(Hz)
101 B85P32 = h*25.790e6;                %(Hz)
102
103 %Constants Rb87
104 A87S12 = h*3.417341305452145e9;     %(Hz)
105 A87P12 = h*407.24e6;                %(Hz)
106 A87P32 = h*84.7185e6;               %(Hz)
107 B87P32 = h*12.4965e6;               %(Hz)
108
109 K = F*(F + 1) - Inam*(Inam + 1) - J*(J + 1);
110
111 if (Inam == Inam85)          % Rb85 hyperfine energy levels
112     if(L == 0)
113         dEhfs = .5*A85S12*K;
114     elseif(L == 1 && J == .5)
115         dEhfs = .5*A85P12*K;
116     elseif(L == 1 && J == 1.5)
117         dEhfs = (.5*A85P32*K) + B85P32*((1.5*K*(K+1) -...
118             2*Inam*(Inam+1)*J*(J+1))/(4*Inam*(2*Inam-1)*J*(2*J-1)));
119     else
120         fprintf('\nIMPROPER INPUT-Hyperfine energy lvl determination\n\n')
121         dEhfs = 0;
122     end
123 elseif (Inam == Inam87)      % Rb87 hyperfine energy levels
124     if(L == 0)
125         dEhfs = .5*A87S12*K;
126     elseif(L == 1 && J == .5)
127         dEhfs = .5*A87P12*K;
128     elseif(L == 1 && J == 1.5)
129         dEhfs = (.5*A87P32*K) + B87P32*((1.5*K*(K+1) -...
130             2*Inam*(Inam+1)*J*(J+1))/(4*Inam*(2*Inam-1)*J*(2*J-1)));
131     else
132         fprintf('\nIMPROPER INPUT-Hyperfine energy lvl determination\n\n')
133         dEhfs = 0;
134     end
135 else
136     fprintf('\nIMPROPER INPUT-Hyperfine energy lvl determination\n\n')
137     dEhfs = 0;
138 end
139
140 end     %end of function
141
142 %Hyperfine subfunction
143 function dviso = dvIso(Inam)
144 % Provides Isotope shift for Rb85 - all frequencies relative to Rb87.
145 global vo85 vo87 Inam85;
146
147 dvo = vo87 - vo85;          % Isotope's hyperfine spectrum rel. to same
```

```
148                             %   central frquency vo so that
149                             %   voRb85 + dviso = voRb87
150
151 if (Inam == Inam85)
152     dviso = dvo;
153 else
154     dviso = 0;
155 end
156
157 end
158
159
160 %% LINE STRENGTH FACTORS ---------------------------------------------------
161 function [S] = S_fun(F,Fprime,J,Jprime,I)
162 S1 = Wigner6j(J,Jprime,1,Fprime,F,I);
163 S = (2*Fprime+1)*(2*J+1)*(S1^2);
164
165 end     %end of function
166
167
168 %% WIGNER 6j FACTORS -------------------------------------------------------
169 function Wigner = Wigner6j(j1,j2,j3,J1,J2,J3)
170 % Wigner 6j-symbol calculator. Written by Amita B Deb, Clarendon Lab. 2007.
171 % Improved by Richard A. Holt, Univ. of Western Ontario, 2009.
172 % Further improved to deal with large input arguments by Lee Harper,
173 % CRL Oxford, 2009.
174
175 % Builds on the m-file Wigner6jcoeff posted by Richard A. Holt.
176
177 % Calculates { j1, j2 ,j3}  using Racah formula.
178 %              J1  J2  J3
179
180 % Finding Triangular coefficients
181
182 tri1 = triangle_coeff(j1,j2,j3);
183 tri2 = triangle_coeff(j1,J2,J3);
184 tri3 = triangle_coeff(J1,j2,J3);
185 tri4 = triangle_coeff(J1,J2,j3);
186
187 if (tri1==0||tri2==0||tri3==0||tri4==0)
188     Wigner=0;
189     return
190 end
191
192 % Finding the range of summation in the Racah formula.
193
194 a(1) = j1 + j2 + j3;
195 a(2) = j1 + J2 + J3;
196 a(3) = J1 + j2 + J3;
197 a(4) = J1 + J2 + j3;
198
199 rangei = max(a);
```

```
200
201 k(1) = j1 + j2 + J1 + J2;
202 k(2) = j2 + j3 + J2 + J3;
203 k(3) = j3 + j1 + J3 + J1;
204
205 rangef = min(k);
206
207 Wigner = 0;
208
209    for t=rangei:rangef
210
211       Wigner = Wigner + ((-1)^t)*exp(gammaln(t+2) -...
212           fung(t,j1,j2,j3,J1,J2,J3));
213
214    end
215
216    Wigner = (tri1*tri2*tri3*tri4)^(0.5)*Wigner;
217
218 end
219
220 % ----- Wigner6j subfunctions --------------
221 function r = fung(t, j1,j2,j3,J1,J2,J3)
222 % Calculating the logarithm of the denominator in Racah Formula, using
223 % the gamma function in place of the factorial.
224 r = sum(gammaln([(t-j1-j2-j3);(t-j1-J2-J3);(t-J1-j2-J3);(t-J1-J2-j3);...
225                  (j1+j2+J1+J2-t);(j2+j3+J2+J3-t);(j3+j1+J3+J1-t)] + 1));
226
227 end
228
229 %-----------------------------------------
230 function tri = triangle_coeff(a,b,c)
231 % Calculates triangle coefficients for angular momenta.
232 % This version returns 0 if the triangle inequalities are violated.  (RAH)
233
234 if (a<0 || b<0 || c<0)
235     tri=0;
236     return
237 end
238
239 for xa = abs(a-b):1:a+b
240     if c==xa
241         tri = factorial(a+b-c)*factorial(a-b+c)*...
242             factorial(-a+b+c)/(factorial(a+b+c+1));
243         return
244     end
245 end
246
247 tri=0;
248
249 end     %end of function
250
251
```

```
%% CROSS SECTION AT LINE CENTER ----------------------------------------
function [s0] = sigma_0Rb(SFF,vD,x)
% Calculates cross section at line center for each hyperfine transition
global c vo85 vo87 tau TransM Inam85 Inam87;

if (TransM(x,1)==Inam85)
    vo = vo85;
elseif (TransM(x,1)==Inam87)
    vo = vo87;
else
    fprintf('\nERROR in sigma_0Rb -- Inam is outside allowed range.\n\n');
    return;
end

dvnat = 1/(2*pi*tau);

s0 = SFF(x)*(1/tau)*(((c*100)^2)/(8*pi))*(1/((vo+vD(x))^2))*...
        ((2*TransM(x,2)+1)/(2*.5+1))*(2/(pi*dvnat));

end


%% NUMBER DENSITY ------------------------------------------------------
function [ndensity] = NumDensityRb(T)
% calculates number density (cm^-3) given Temperature in Kelvin
global kB;

ndensity = (RbVaporPressure(T))/(kB*T)*101325*(1e-6);
end


%% VAPOR PRESSURE ------------------------------------------------------
function [Pv] = RbVaporPressure(T)
% Provides rubidium vapor pressure in atmospheres given T in Kelvin
%
% REFERENCE:
%   C.B.Alcock, V.P.Itkin, and M.K.Horrigan
%   Vapour pressure equations for the metallic elements: 298-2500K
%   Canadian Metallurgical Quarterly, 1984, 23, 309-313
%
% "Precise" equation for Rb vapour pressure.
% Uses melting point for Rb at 312.45K (39.30 degC)
% Valid for temperatures from melting point to 550K.
%
% "Practical" equations for RB are used from 298K to melting point.
%   There is a discontinuity at 312.45K.  Yields +/-5% or better precision.
%   For best precision, use temperatures between melting point and 550K.

if(T ≥ 312.45 && T ≤ 550)
    a = 8.316;
    b = -4275;
    c = -1.3102;
```

```
304     Pv = 10.^(a + b*(T^-1) + c*log10(T));
305 elseif (T ≥ 298 && T < 312.45)
306     a = 4.857;
307     b = -4040;
308     Pv = 10.^(a + b*(T^-1));
309 elseif (T < 298 || T > 550)
310     fprintf('\nTemperature is outside of allowed range.\n\n')
311     return
312 end
313 
314 end
315 
316 
317 %% CROSS SECTION ----------------------------------------------------------
318 function [cs] = CrossSectionRb(x,T,PHe,PCH4)
319 % Calculates cross section as function of frequency, x
320 global tau s0 vo85 vo87 TransM vHF numTrans Inam85 Inam87;
321 
322 dvnat = 1/(2*pi*tau);       % natural linewidth, ∆ nu natural
323 csHF = zeros(1,numTrans);   % Cross section for an individual HF transition
324 
325 temp = 0;
326 for n = 1:numTrans
327     Inam = TransM(n,1);
328     Flwr = TransM(n,3);
329     [gamma,shift,dvD,dvL] = BufferGasRb(T,Inam,PHe,PCH4);
330     if (Inam == Inam85)     % Set central frequency based on isotope (Inam)
331         vo = vo85;
332     elseif (Inam == Inam87)
333         vo = vo87;
334     else
335         fprintf('\nERROR in CrossSectionRB-Inam is outside range.\n\n');
336         return;
337     end
338     csHF = RbNatAbundance(Inam) * BoltzRatioRb(Inam,Flwr,T) * s0(n) * ...
339         ((x + vHF(n) + shift + vo) / (vHF(n) + shift + vo)) * ...
340         gVoigt((x - vHF(n)),dvL,dvD);
341     temp = temp + csHF;
342 end
343 
344 cs = (dvnat*pi/2) * temp;
345 
346 end
347 
348 function eta = RbNatAbundance(Inam)
349 % Return Rubidium natural abundance based on Total nuclear angular momentum
350 Eta85 = 0.7217;
351 Eta87 = 0.2783;
352 
353 if (Inam == 5/2)
354     eta = Eta85;
355     return;
```

```
356 elseif (Inam == 3/2)
357     eta = Eta87;
358     return;
359 else
360     fprintf('\nInam is outside of allowed range for Rb85 or Rb87.\n\n');
361     return;
362 end
363 
364 end
365 
366 %% BUFFER GAS EFFECTS ----------------------------------------------------
367 function [gamma,shift,dvD,dvL] = BufferGasRb(T,Inam,PHe,PCH4)
368 % Rb buffer gas effects - pressure broadening and frequency shift
369 %
370 % REFERENCE:
371 %   Rotondaro, M. D. & Perram, G. P.
372 %   Collisional broadening and shift of the rubidium D1 and D2 lines
373 %       (5^2S_1/2 -> 5^2P_1/2, 5^2S_1/2 -> 5^2P_3/2) by rare gases,
374 %       H_2, D_2, N_2, CH_4, and CF_4
375 %   Journal of Quan. Spect. and Radiative Transfer, 1997, 57, 497-507
376 
377 global tau c kB MRb85 MRb87 vo85 vo87 Inam85 Inam87 TransM;
378 
379 Tdata = 394.15; % Temperature (K) at which buffer gas values were measured
380 
381 % Set effect constants based on D1 or D2 line (J_upper).
382 if (TransM(1,2)==1/2)   %D1 values
383     gammaHe = 18.9e6;   % MHz/Torr
384     shiftHe = 4.71e6;   % MHz/Torr
385     gammaCH4 = 29.1e6;  % MHz/Torr
386     shiftCH4 = -7.92e6; % MHz/Torr
387 else %D2 values
388     gammaHe = 20.0e6;   % MHz/Torr
389     shiftHe = 0.37e6;   % MHz/Torr
390     gammaCH4 = 26.2e6;  % MHz/Torr
391     shiftCH4 = -7.00e6; % MHz/Torr
392 end
393 
394 % Set central frequency and mass based on isotope
395 if (Inam == Inam85)
396     vo = vo85;
397     MRb = MRb85;
398 elseif (Inam == Inam87)
399     vo = vo87;
400     MRb = MRb87;
401 else
402     fprintf('\nERROR in BufferGasRb-Inam is outside range.\n\n');
403     return;
404 end
405 
406 gamma = (gammaHe)*((T/Tdata)^(1/2))*PHe +(gammaCH4)*((T/Tdata)^(1/2))*PCH4;
407 shift = (shiftHe)*((T/Tdata)^(1/2))*PHe +(shiftCH4)*((T/Tdata)^(1/2))*PCH4;
```

```
408 dvD = (vo + shift)*((8*kB*T*log(2))/(MRb*(c^2)))^(1/2);
409 dvL = (1/(2*pi*tau)) + gamma;
410 end
411
412
413 %% BOLTZMAN RATIO ------------------------------------------------------
414 function [BR] = BoltzRatioRb(Inam,F,T)
415 global kB h dv85S12 dv87S12 Inam85 Inam87;
416
417 if (Inam == Inam85)
418     if(F == 2)
419        BR = 5./(5 + 7*exp(-(h*dv85S12)./(kB.*T)));
420     elseif(F == 3)
421        BR=(7*exp(-(h*dv85S12)./(kB.*T)))./(5+7*exp(-(h*dv85S12)./(kB.*T)));
422     elseif(F ~= 2 && F ~= 3)
423        fprintf('\nIMPROPER INPUTS\n\n')
424        BR = 0;
425     end
426 elseif (Inam == Inam87)
427     if(F == 1)
428        BR = 3./(3 + 5*exp(-(h*dv87S12)./(kB.*T)));
429     elseif(F == 2)
430        BR=(5*exp(-(h*dv87S12)./(kB.*T)))./(3+5*exp(-(h*dv87S12)./(kB.*T)));
431     elseif(F ~= 1 && F ~= 2)
432        fprintf('\nIMPROPER INPUTS\n\n')
433        BR = 0;
434     end
435 else
436     fprintf('\nIMPROPER INPUTS\n\n')
437     BR = 0;
438 end
439
440 end
441
442
443 %% VOIGT LINESHAPE -----------------------------------------------------
444 function [y] = gVoigt(v,dvL,dvD)
445 % A useful approximation for the Voigt convolution is given by Thompson
446 %
447 % REFERENCE:
448 % William J. Thompson
449 % Numerous neat algorithms for the Voigt profile function.
450 % Computers in Physics, Vol 7, No. 6, Nov/Dec 1993.
451 %
452 %   gV(u,a) = Re[Exp(z^2)erfc(z)]
453 %       z = a + iu
454 %       a = sqrt(ln(2)) vLorentzian/vDoppler
455 %       u = 2 sqrt(ln(2)) (v-vo)/vDoppler
456
457 % NOTE: Not valid for Doppler free spectra where vDoppler = 0
458 % NOTE: erfc(z) = 1 - erf(z) (related to the Faddeeva function)
459
```

```
460 a = sqrt(log(2))*(dvL/dvD);
461 u = 2*sqrt(log(2))*(v/dvD);
462 z = a + 1i*u;
463 y = 2*sqrt(log(2)/pi)*(1/dvD)*real(faddeeva(1i*z));
464 end
465
466 % ----- gVoigt subfunctions --------------
467
468 function w = faddeeva(z,N)
469 % FADDEEVA   Faddeeva function
470 %   W = FADDEEVA(Z) is the Faddeeva function, aka the plasma dispersion
471 %   function, for each element of Z. The Faddeeva function is defined as:
472 %
473 %     w(z) = exp(-z^2) * erfc(-j*z)
474 %
475 %   where erfc(x) is the complex complementary error function.
476 %
477 %   W = FADDEEVA(Z,N) can be used to explicitly specify the number of terms
478 %   to truncate the expansion (see (13) in [1]). N = 16 is used as default.
479 %
480 %   Example:
481 %       x = linspace(-10,10,1001); [X,Y] = meshgrid(x,x);
482 %       W = faddeeva(complex(X,Y));
483 %       figure;
484 %       subplot(121); imagesc(x,x,real(W)); axis xy square; caxis([-1 1]);
485 %       title('re(faddeeva(z))'); xlabel('re(z)'); ylabel('im(z)');
486 %       subplot(122); imagesc(x,x,imag(W)); axis xy square; caxis([-1 1]);
487 %       title('im(faddeeva(z))'); xlabel('re(z)'); ylabel('im(z)');
488 %
489 %   Reference:
490 %   [1] J.A.C. Weideman, "Computation of the Complex Error Function," SIAM
491 %       J. Numerical Analysis, pp. 1497-1518, No. 5, Vol. 31, Oct., 1994
492 %       Available Online: http://www.jstor.org/stable/2158232
493
494 if nargin<2, N = []; end
495 if isempty(N), N = 16; end
496
497 w = zeros(size(z)); % initialize output
498
499 %%%%%
500 % for purely imaginary-valued inputs, use erf as is if z is real
501 idx = real(z)==0; %
502 w(idx) = exp(-z(idx).^2).*erfc(imag(z(idx)));
503
504 if all(idx), return; end
505 idx = ¬idx;
506
507 %%%%%
508 % for complex-valued inputs
509
510 % make sure all points are in the upper half-plane (positive imag. values)
511 idx1 = idx & imag(z)<0;
```

```
512 z(idx1) = conj(z(idx1));
513
514 M = 2*N;
515 M2 = 2*M;
516 k = (-M+1:1:M-1)'; % M2 = no. of sampling points.
517 L = sqrt(N/sqrt(2)); % Optimal choice of L.
518
519 theta = k*pi/M;
520 t = L*tan(theta/2); % Variables theta and t.
521 f = exp(-t.^2).*(L^2+t.^2);
522 f = [0; f]; % Function to be transformed.
523 a = real(fft(fftshift(f)))/M2; % Coefficients of transform.
524 a = flipud(a(2:N+1)); % Reorder coefficients.
525
526 Z = (L+1i*z(idx))./(L-1i*z(idx));
527 p = polyval(a,Z); % Polynomial evaluation.
528 w(idx) = 2*p./(L-1i*z(idx)).^2 + (1/sqrt(pi))./(L-1i*z(idx)); % Evaluate w(z).
529
530 % convert the upper half-plane results to the lower half-plane if necesary
531 w(idx1) = conj(2*exp(-z(idx1).^2) - w(idx1));
532
533 end
```

Absorption Coefficient Changes for Rb D_2

The previous MATLAB® code example can be easily modified for rubidium D_2 or any other atomic species with multiple isotopes. To change the MATLAB® absorption coefficient function on page C for rubidium D_2 make the following modifications at the appropriate places within the code. To modify use of this code for other atomic elements, be sure to modify vapor pressure and buffer gas effect functions.

```
% Contstants...
% Rb D2 Data
vo85 = 384.230406373e12;     % Frequency (Hz) Rb85
vo87 = 384.2304844685e12;    % Frequency (Hz) Rb87
tau = 26.2348e-9;            % Lifetime (s) Rb85 and Rb87
TransM = [5/2 3/2 2 1;
          5/2 3/2 2 2;
          5/2 3/2 2 3;
          5/2 3/2 3 2;
          5/2 3/2 3 3;
          5/2 3/2 3 4;
          3/2 3/2 1 0;
          3/2 3/2 1 1;
          3/2 3/2 1 2;
          3/2 3/2 2 1;
          3/2 3/2 2 2;
          3/2 3/2 2 3];
```

Sample Cesium Absorption Coefficient Code

The following code sample illustrates use of MATLAB® functions `fnAbsCoeffCsD2.m`, `fnAbsCoeffCsD1.m` and `fnAbsCoeffCsD2SingleHFLine.m` creating figure output as shown in Figure 46.

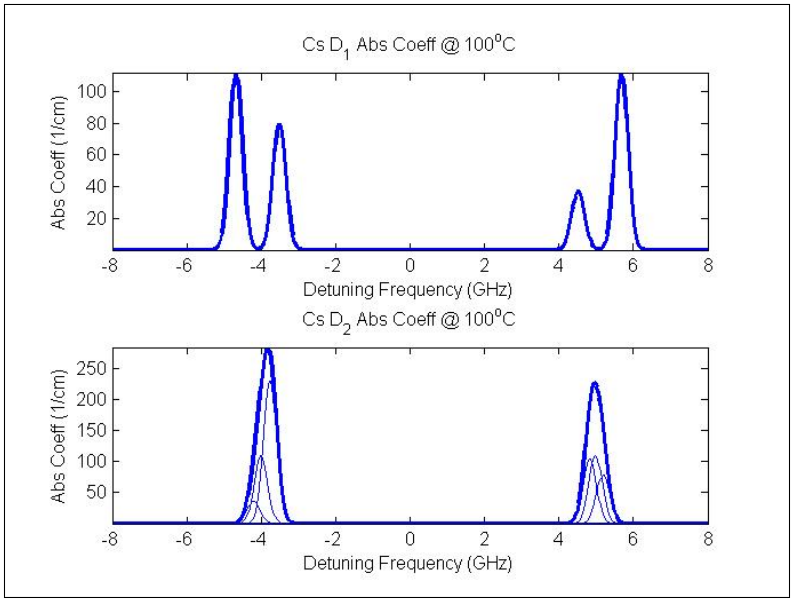

Figure 46. Sample Absorption Cesium Coefficient Code figure output

```
% Cesium Absorption Coefficient D1 and D2
%-------------------------------------------------------------------------
% Monte D. Anderson
% Department of Engineering Physics, Air Force Institute of Technology
% 6 Aug 2010
%-------------------------------------------------------------------------
% Calculates cesium D2 absorption coefficent (1/cm) at a given frequency
% at temperature T (K) and buffer gas pressures PN2, PHe, and PCH4 (Torr)
%-------------------------------------------------------------------------
% REQUIRES:
%   fnAbsCoeffCsD1
%   fnAbsCoeffCsD2
%   fnAbsCoeffCsD2SingleHFLine

%% CLEAR
close all
clear all
```

```
clc

tic

%% calcuations
c = 2.99792458e8;  %m/s
voD2 = 351725718;  %MHz
voD1 = 335116049;  %MHz

nu = linspace(-8e9,8e9,500);

T = 100 + 273.15;
PN2 = 0;
PHe = 0;
PCH4 = 0;
cell_length = 5;

absCoeffD1 = zeros(length(nu),1);
absCoeffD2 = zeros(length(nu),1);
lambdaD2 = zeros(length(nu),1);
lambdaD1 = zeros(length(nu),1);

for i=1:length(nu)
    absCoeffD1(i) = fnAbsCoeffCsD1(nu(i),T,PN2,PHe,PCH4);
    absCoeffD2(i) = fnAbsCoeffCsD2(nu(i),T,PN2,PHe,PCH4);
    a32(i) = fnAbsCoeffCsD2SingleHFLine(nu(i),T,PN2,PHe,3,2);
    a33(i) = fnAbsCoeffCsD2SingleHFLine(nu(i),T,PN2,PHe,3,3);
    a34(i) = fnAbsCoeffCsD2SingleHFLine(nu(i),T,PN2,PHe,3,4);
    a43(i) = fnAbsCoeffCsD2SingleHFLine(nu(i),T,PN2,PHe,4,3);
    a44(i) = fnAbsCoeffCsD2SingleHFLine(nu(i),T,PN2,PHe,4,4);
    a45(i) = fnAbsCoeffCsD2SingleHFLine(nu(i),T,PN2,PHe,4,5);
    lambdaD2(i) = c./(nu(i)*(1e-9)+voD2*(1e-3));
    lambdaD1(i) = c./(nu(i)*(1e-9)+voD1*(1e-3));
end

%% plot

figure
subplot(2,1,1);
    plot(nu*(1e-9),absCoeffD1,'LineWidth',2);
    title(['Cs D_1 Abs Coeff @ ',num2str(T-273.15),'^oC']);
    xlabel('Detuning Frequency (GHz)');
    ylabel('Abs Coeff (1/cm)');
    axis tight
subplot(2,1,2)
    plot(nu*(1e-9),absCoeffD2,'LineWidth',2);
    hold on
    plot(nu*(1e-9),a32,'LineWidth',1);
    plot(nu*(1e-9),a33,'LineWidth',1);
    plot(nu*(1e-9),a34,'LineWidth',1);
    plot(nu*(1e-9),a43,'LineWidth',1);
    plot(nu*(1e-9),a44,'LineWidth',1);
```

```
70      plot(nu*(1e-9),a45,'LineWidth',1);
71      title(['Cs D_2 Abs Coeff @ ',num2str(T-273.15),'^oC']);
72      xlabel('Detuning Frequency (GHz)');
73      ylabel('Abs Coeff (1/cm)');
74      axis tight
75      hold off
76
77  toc
78
79  % tblSaveD1 = [nu'*(1e-9) lambdaD1 absCoeffD1];
80  % tblSaveD2 = [nu'*(1e-9) lambdaD2 absCoeffD2];
81  % save 'C:\SimAbsCoeff-D1.dat' tblSaveD1 -ascii -double;
82  % save 'C:\SimAbsCoeff-D2.dat' tblSaveD2 -ascii -double;
```

Sample Rubidium Absorption Coefficient Code

The following code sample illustrates use of MATLAB® function `fnAbsCoeffRbD1.m`, creating figure output as shown in Figure 47.

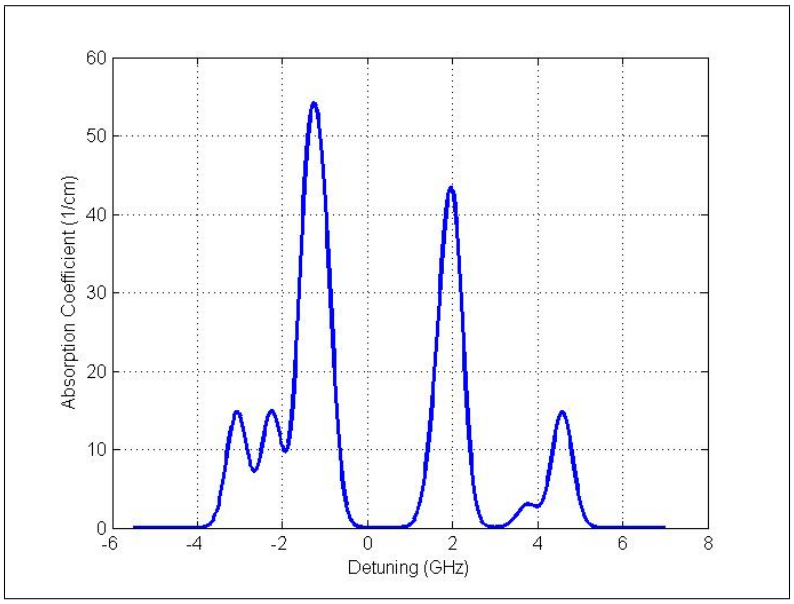

Figure 47. Sample Rubidium Absorption Coefficient Code figure output

```
%  RbD1AbsCoeffMaker.m
%--------------------------------------------------------------------------
% Monte D. Anderson
% Department of Engineering Physics, Air Force Institute of Technology
% 26 Feb 2010
%--------------------------------------------------------------------------
% Calculates absolute aborption coefficient from temperature in Kelvin
%   and buffer gas pressures
%--------------------------------------------------------------------------
clear all; close all; clc
tic

startGHz = -5.5;
stopGHz = 7;
numPts = 501;
ΔNu = (stopGHz - startGHz)/(numPts-1);

T = 273.15 + 110;    %temp in Kelvin
PHe = 0;             %Torr
```

```
PCH4 = 0;           %Torr

c = 2.99792458e8;   %m/s
vo87 = 377.1074633805e6;   % Frequency (MHz) Rb87

alpha = zeros(1,numPts);
nuref = zeros(1,numPts);
lambda = zeros(1,numPts);

number1 = 0;
for freq = startGHz:ΔNu:stopGHz   %GHz from nu ref
    number1 = number1+1;
    alpha(number1) = fnAbsCoeffRbD1(freq*1e9,T,PHe,PCH4);
    nuref(number1) = freq;
    lambda(number1) = c./(freq+vo87*(1e-3));
end

figure
plot(nuref,alpha,'b','LineWidth',2);
xlabel('Detuning (GHz)'); ylabel('Absorption Coefficient (1/cm)');
title(['Rb D_1 @ ',num2str(T-273.15),'^oC']);
grid on

figure
plot(lambda,alpha,'b','LineWidth',2);
xlabel('Wavelength (nm)'); ylabel('Absorption Coefficient (1/cm)');
title(['Rb D_1 @ ',num2str(T-273.15),'^oC']);
grid on

% I/Io ------------------------------------------------------------------
% Calculates intensity ratio I/Io

% cellLength = 5; % Cell length in cm
%
% IovrIo = zeros(1,2001);
% number1 = 0;
% for freq = -10:.01:10
%   number1 = number1+1;
%   IovrIo(number1) = exp(-fnAbsCoeffRbD1(freq*1e9,T,PHe,PCH4)*cellLength);
% end
%
% freq = -10:.01:10;
% figure
% hold on
% plot(freq,IovrIo,'r','LineWidth',2);
% xlabel('Detuning (GHz)'); ylabel('I/Io (unitless)');
% axis([-10 10 0 1]);
% grid on
% hold off

% Save Data -------------------------------------------------------------
tblSave = [lambda' alpha'];
```

```
72 %save 'C:\SimRbD1AbsCoeff-100C.txt' tblSave -ascii -double;
```

Kramers-Kronig Group Delay Prediction

The following code calculates delay from absorption coefficient using the Kramers-Kronig model. This code can be easy modified for any simulated absorption coefficient or used with observed absorption. Sample output is shown in Figure 48 and Figure 49.

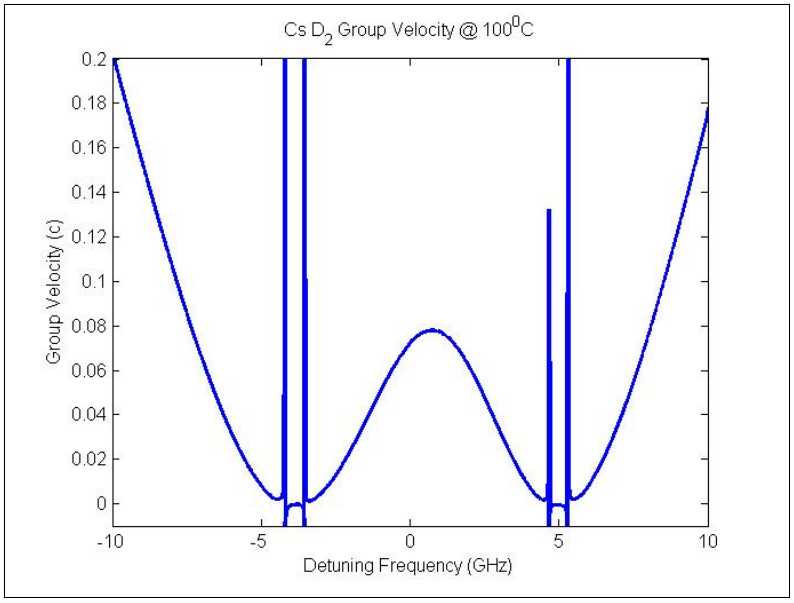

Figure 48. Group velocity output from Kramers-Kronig delay calculation.

```
% DelayPrediction.m
%--------------------------------------------------------------------------
% Monte D. Anderson
% Department of Engineering Physics, Air Force Institute of Technology
% 19 Mar 2010
%--------------------------------------------------------------------------
% Calculates predicted delay given absorption coefficient using the
% Kramers-Kronig delay model outlined in
%
% Monte D. Anderson, Glen P. Perram
% Slow light in cesium vapor: pulse delay measurements and predicted delay
% (Proceedings Paper) Published 11 February 2010
% Vol. 7612: Advances in Slow and Fast Light III,
% Selim M. Shahriar; Philip R. Hemmer, Editors, 76120A
%--------------------------------------------------------------------------
% REQUIRES:
```

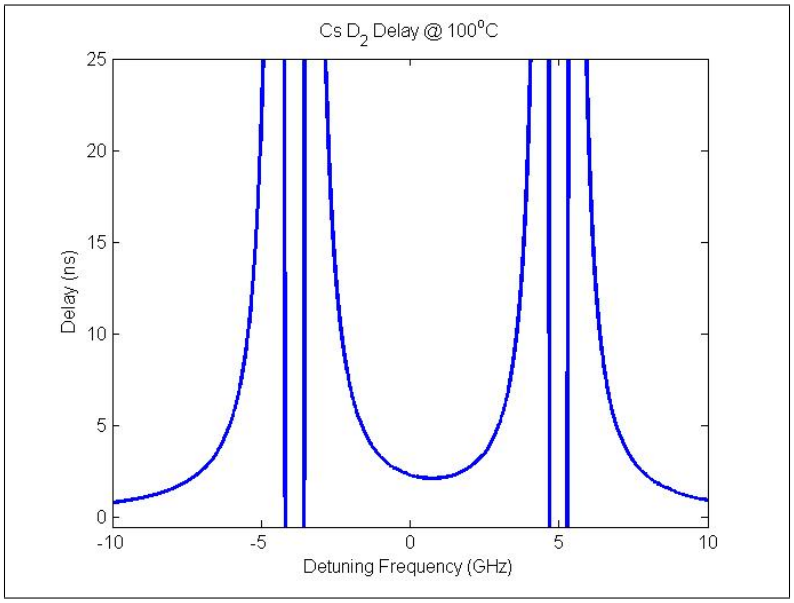

Figure 49. Delay output from Kramers-Kronig calculation.

```
%   fnAbsCoeffCsD2.m
%-------------------------------------------------------------------------

clear all;
close all;
clc;
tic

% Constants ---------------------------------------------------------------
% Physical Constants (NIST CODATA 2006 values)
c = 2.99792458e8;           % vacuum speed of light (m/s)

% Cs D2 Data
vo = 351.72571850e12;       % Frequency (Hz)

% Scenario Information ----------------------------------------------------
T = 100;            %Temporary temperature (C)
PN2 = 0;            %N2 pressure (Torr)
PHe = 0;            %He pressure (Torr)
PCH4 = 0;           %CH4 pressure (Torr)
vmin = -10100E6;    %ref frequency in Hz from center frequency
vmax = 10100E6;     %ref frequency in Hz from center frequency
NumPts = 10000;     %Total number of points will be NumPts+1
Δ_nu = (vmax - vmin)/NumPts;    %discrete step size in Hz

% Absorption Coefficient --------------------------------------------------
tblSimalpha = zeros(NumPts+1,2);
for n = 1:NumPts+1
```

```
45      tblSimalpha(n,1) = vmin - Δ_nu + n*Δ_nu;
46      tblSimalpha(n,2) = fnAbsCoeffCsD2(tblSimalpha(n,1),273.15+T,...
47          PN2,PHe,PCH4);
48  end
49
50  % figure
51  % plot(tblSimalpha(:,1),tblSimalpha(:,2))
52
53  % Real Index of Refraction ------------------------------------------------
54  t1 = zeros(1,NumPts+1);
55  tblnRe = zeros(NumPts+1,2);
56  for p = 0:NumPts
57      for m = 0:NumPts
58          if(m ≠ p)
59              t1(m+1) = (tblSimalpha(m+1,2)/(1e-2))/...
60                ((m*Δ_nu + vmin + vo)^2 - (p*Δ_nu + vmin + vo)^2);
61          else
62              t1(m+1) = 0;
63          end
64      end
65      tblnRe(p+1,1) = p*Δ_nu+vmin;
66      tblnRe(p+1,2) = 1+(((2.99792458e8)/(2*(pi^2)))*sum(t1)*Δ_nu);
67  end
68
69  % figure
70  % plot(tblnRe(:,1),tblnRe(:,2))
71
72  % dn/dv -------------------------------------------------------------------
73  tbldndv = zeros(NumPts+1,2);
74  for n = 2:NumPts
75      tbldndv(n,2) = (tblnRe(n+1,2) - tblnRe(n-1,2))/(2*Δ_nu);
76  end
77  tbldndv(:,1) = tblnRe(:,1);
78  tbldndv(1,2) = 0;
79  tbldndv(NumPts+1,2) = 0;
80
81  % figure
82  % plot(tbldndv(:,1),tbldndv(:,2))
83
84  % Group Velocity ----------------------------------------------------------
85  tblVg = zeros(length(0:NumPts),2);
86  for n = 0:NumPts
87      tblVg(n+1,1) = n*Δ_nu + vmin;
88      tblVg(n+1,2) = 1/(tblnRe(n+1,2) + (tblnRe(n+1,1) + vo)*tbldndv(n+1,2));
89  end
90
91  % figure
92  % plot(tblVg(:,1)*(1e-9),tblVg(:,2))
93
94  % Delay -------------------------------------------------------------------
95  cell_length = 5;  %cell length in centimeters
96  tblDelay = zeros(length(0:NumPts),2);
```

```
for n = 0:NumPts
    tblDelay(n+1,2) = cell_length/(tblVg(n+1,2)*2.99792458e10);
    tblDelay(n+1,1) = n*Δ_nu+vmin;
end

% figure
% plot(tblDelay(:,1),tblDelay(:,2))

% Plot/Export Data Files ------------------------------------------------

%save 'C:\SimAlpha.dat' tblSimalpha -ascii -double;

tblSaveVg = [tblVg(:,1)*(1e-9) tblVg(:,2)];
figure
    plot(tblSaveVg(:,1),tblSaveVg(:,2),'LineWidth',2);
    title(['Cs D_2 Group Velocity @ ',num2str(T),'^0C']);
    xlabel('Detuning Frequency (GHz)');
    ylabel('Group Velocity (c)');
    axis([-10 10 -0.01 0.2]);
% save 'C:\SimVg.dat' tblSaveVgrp -ascii -double;

tblSaveDelay = [tblDelay(:,1)*(1e-9) tblDelay(:,2)*(1e9)];
figure
    plot(tblSaveDelay(:,1),tblSaveDelay(:,2),'LineWidth',2);
    title(['Cs D_2 Delay @ ',num2str(T),'^oC']);
    xlabel('Detuning Frequency (GHz)');
    ylabel('Delay (ns)');
    axis([-10 10 -0.5 25]);
% save 'C:\SimDelay.dat' tblSaveDelay -ascii -double;

toc
```

Hole Burning Locations

The following code calculates hole burning locations for a cesium D_2 pump and corresponding hole locations in cesium D_1, producing the following output shown in Figure 50.

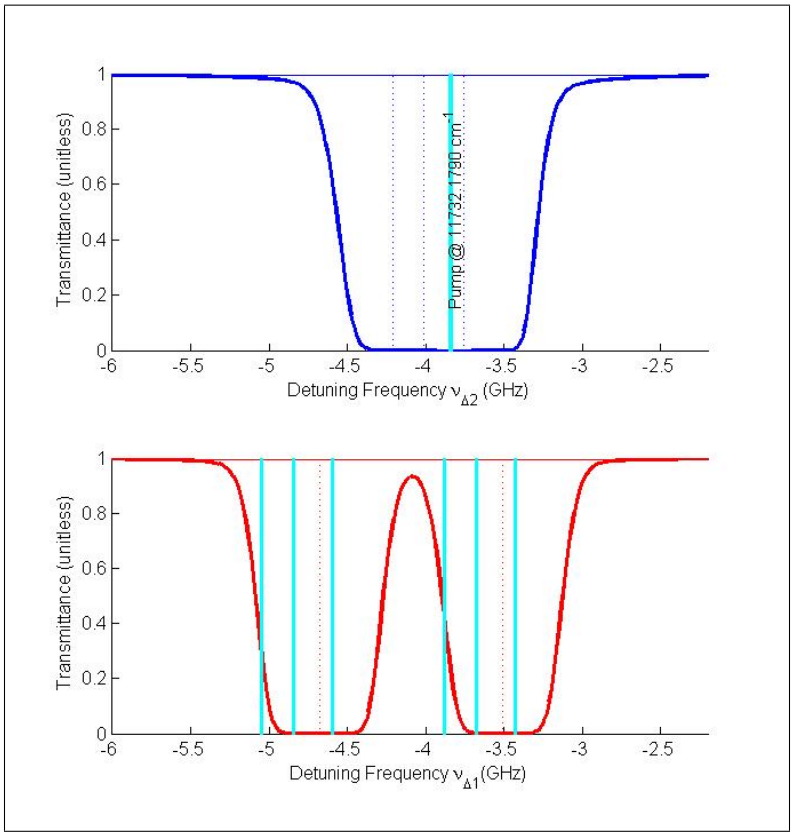

Figure 50. Hole location calculation output.

```
% HoleBurningLocations.m
%--------------------------------------------------------------------------
% Monte D. Anderson
% Department of Engineering Physics, Air Force Institute of Technology
% 19 Apr 2010
%
%   Given a frequency relative to the Cs D2 absorption, calculates the
%   difference from the D2 hyperfine transition frequencies, and plots
%   the same difference relative to all the D1 transitions.  This should
```

```
%   give relative positions of the hole burnt in the D1 absorption due to
%   the hole burnt in the D2 spectrum.
%
%-------------------------------------------------------------------------
%   REQUIRES
%       fnAbsCoeffCsD2.m
%       fnAbsCoeffCsD1.m
%       hfsEnergy.m
%-------------------------------------------------------------------------
clear all;
close all;
clc;

% CONSTANTS ::::::::::::::::::::::::::::::::::::::::::::::::::::::::::::::
global c eo h hbar kB AMU;
global AmCs MCs Inam voD1 voD2 tau;
% Physical Constants (NIST 2006 CODATA recommended values)
c = 2.99792458e8;           % vacuum speed of light (m/s)
eo = 8.85418781762e-12;     % vacuum permittivity (F/m)
h = 6.62606896e-34;         % Planck const (Js)
hbar = 1.054571628e-34;     % Planck const/2pi (Js)
kB = 1.3806504e-23;         % Boltzmann const (J/K)
AMU = 1.660538782e-27;      % Atomic Mass Unit (kg)
% Cesium Atomic Data
AmCs = 132.905451931;       % Atomic mass (AMU)
MCs = AmCs*AMU;             % Mass of Cs atom (kg)
Inam = 7/2;                 % Total nuclear angular momentum
% Cs D2/D1 Data
voD2 = 351.72571850e12;     % Frequency (Hz)
voD1 = 335.116049e12;       % Frequency (Hz)
tau = 30.32e-9;             % Lifetime (s)

%Transition Definitions
TransMD2 = [7/2 3/2 3 2;
          7/2 3/2 3 3;
          7/2 3/2 3 4;
          7/2 3/2 4 3;
          7/2 3/2 4 4;
          7/2 3/2 4 5];
numTransD2 = length(TransMD2);

TransMD1 = [7/2 1/2 3 3;
          7/2 1/2 3 4;
          7/2 1/2 4 3;
          7/2 1/2 4 4];
numTransD1 = length(TransMD1);

vD1 = zeros(1,numTransD1);
for j = 1:numTransD1
    vD1(j) = (hfsEnergy(TransMD1(j,1),1,TransMD1(j,2),TransMD1(j,4))/h)-...
        (hfsEnergy(TransMD1(j,1),0,1/2,TransMD1(j,3))/h);
end
```

```
dvS12 = hfsEnergy(Inam,0,1/2,4)/h - hfsEnergy(Inam,0,1/2,3)/h;

vD2 = zeros(1,numTransD2);
for j = 1:numTransD2
    vD2(j) = (hfsEnergy(TransMD2(j,1),1,TransMD2(j,2),TransMD2(j,4))/h)-...
        (hfsEnergy(TransMD2(j,1),0,1/2,TransMD2(j,3))/h);
end


% MAIN ..........................................................................
nu = linspace(-8e9,8e9,1000);

T = 50;
PN2 = 0;
PHe = 0;
PCH4 = 0;
CellLength = 5;

nuProbe = -3.84e9;      % 11732.1790
% nuProbe = -3.86e9;      % 11732.1783
% nuProbe = -3.924e9;       % 11732.1762
% nuProbe = -3.90e9;       % 11732.1770
dnuProbe = nuProbe - vD2;

nuabs = voD2 + nuProbe;
lambda = c/nuabs;
wavenum = nuabs/c;
fprintf('D2 Frequency ----\n');
fprintf('%3.4f nm\n',lambda*(1e9));
fprintf('%5.4f 1/cm\n',wavenum*(1e-2));
strwn = sprintf('%5.4f',wavenum*(1e-2));
fprintf('-----------------\n');

holesD1 = zeros(length(vD1),length(dnuProbe));
holeColorStr = zeros(length(vD1),length(dnuProbe));
for i=1:length(vD1)
    for j = 1:length(dnuProbe)
        holesD1(i,j) = vD1(i) - dnuProbe(j);
    end
end

absCoeffD1 = zeros(length(nu),length(T));
absCoeffD2 = zeros(length(nu),length(T));
lambdaD1 = zeros(length(nu),length(T));
IRatio = zeros(length(nu),length(T));
for i=1:length(nu)
        absCoeffD1(i,j) = fnAbsCoeffCsD1(nu(i),T+273.15,PN2,PHe,PCH4);
        absCoeffD2(i,j) = fnAbsCoeffCsD2(nu(i),T+273.15,PN2,PHe,PCH4);
        lambdaD1(i,j) = c./(nu(i)*(1e-9)+voD1*(1e-3));
        IRatio(i,j) = exp(-absCoeffD1(i,j)*CellLength);
end

```

```
% PLOTS ..........................................................
peak = max(max(max(absCoeffD1)),max(max(absCoeffD2)));
ylgt = linspace(0,peak,250);
ydrk = linspace(0,peak,1000);

plotmin = -6;
plotmax = -2.2;

figure
    subplot(2,1,1)
        hold all
        plot(nu*(1e-9),exp(-absCoeffD2*CellLength),'b');
        ax = axis;
        axis([plotmin plotmax 0 1]);
        plot([nuProbe*(1e-9) nuProbe*(1e-9)],[0 1],'c','LineWidth',3);
        h = text(nuProbe*(1e-9),ax(4)/2,[' Pump @ ',strwn,' cm^{-1}'],...
            'VerticalAlignment','middle',...
            'HorizontalAlignment','center',...
            'FontSize',9);
        set(h, 'rotation', 90)
        for i = 1:numTransD2
            plot([vD2(i)*(1e-9) vD2(i)*(1e-9)],[0 1],'b:')
        end
        xlabel('Detuning Frequency \nu_{\Delta2} (GHz)');
        ylabel('Transmittance (unitless)');
        hold off

    subplot(2,1,2)
        hold all
        plot([vD1(1)*(1e-9) vD1(1)*(1e-9)],[0 1],'r')
        ax = axis;
        axis([plotmin plotmax 0 1]);
        plot(nu*(1e-9),exp(-absCoeffD1*CellLength),'r');
        for i = 1:numTransD1
            plot([vD1(i)*(1e-9) vD1(i)*(1e-9)],[0 1],'r:')
        end
        for i=1:length(vD1)
            for j = 1:length(dnuProbe)
               plot([holesD1(i,j)*(1e-9) holesD1(i,j)*(1e-9)],[0 1],...
                   'c','LineWidth',2);
            end
        end
        xlabel('Detuning Frequency \nu_{\Delta1}(GHz)');
        ylabel('Transmittance (unitless)');
        hold off
```

Appendix D. Delay-Absorbance Plots

Introduction

Most of the delay plots in this manuscript are given in terms of delay as a function of detuning frequency. Other graphical interpretations are useful if there is physically meaningful information which can be extracted. In EIT slow light schemes, Kasapi *et al.*(Kasapi et al., 1995) used a particularly insightful plot with absorbance presented as a function of delay. The slope of the resulting EIT delay was given as the linewidth of the transitions (Kasapi et al., 1995).

Similar graphical representations of the absorbance as a function of delay can be created for delays observed in the linear dispersion regime. The following plots present theoretical absorbance-delay plots from the linear dispersion Kramers-Kronig delay predictions and delay data from the preceding chapters.

Temperature Dependence

Temperature dependence of the delay-absorbance curves are displayed in Figure 51 and Figure 52. The initial slope of the curve appears to follow a common asymptote, but the curves depart at longer delays at higher temperatures.

Pressure Dependence

Pressure dependent delay-absorbance curves are shown in Figure 53 and Figure 54 for several simulated helium-broadened samples from 0 Torr to 20 Torr. Notice how the curves no longer follow a common asymptotic limit compared to the temperature-dependent delay-absorbance curves thus the initial slope is clearly a function of pressure.

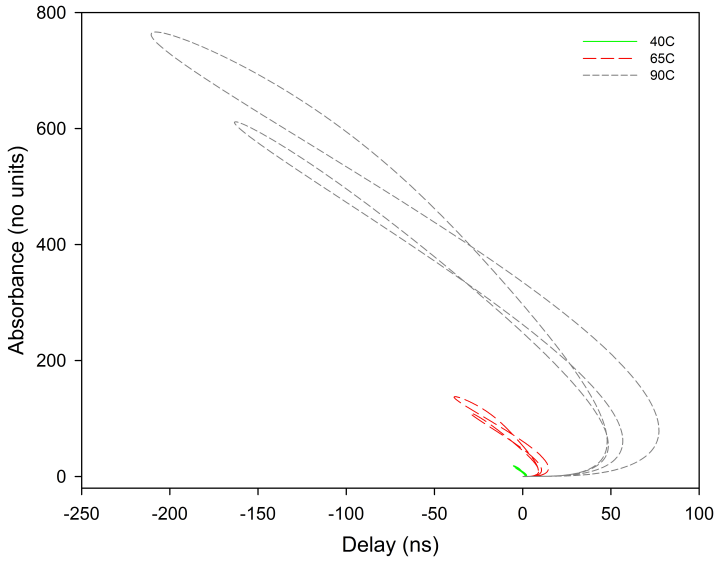

Figure 51. Delay-Absorbance plot showing temperature dependence between 40 °C and 90 °C.

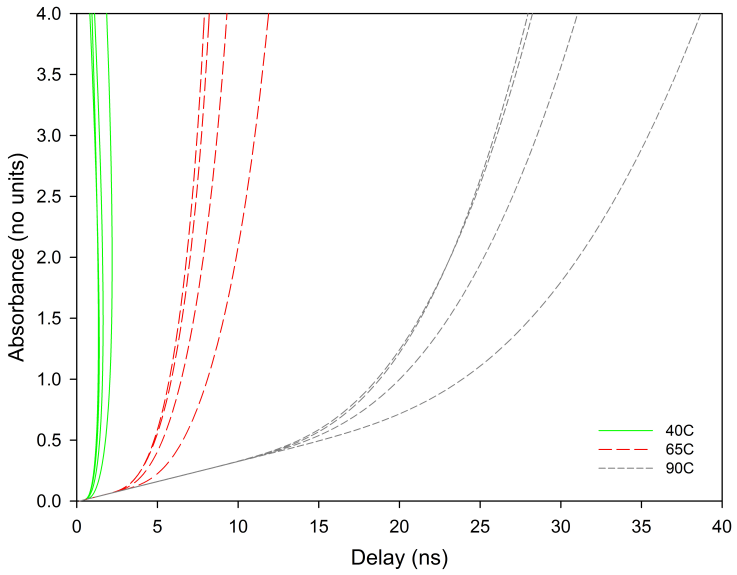

Figure 52. Delay-Absorbance plot showing temperature dependence between 40 °C and 90 °C showing detail of delay between 0 ns and 40 ns.

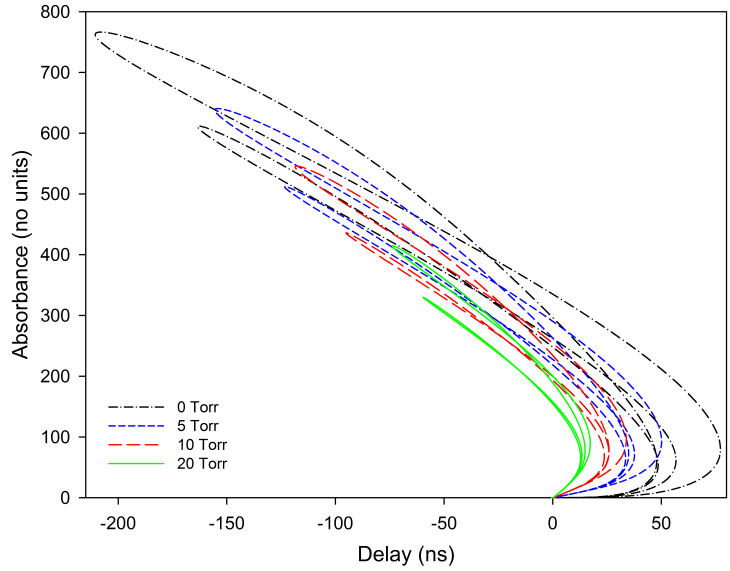

Figure 53. Delay-Absorbance plot showing pressure dependence between 0 Torr **and** 20 Torr**.**

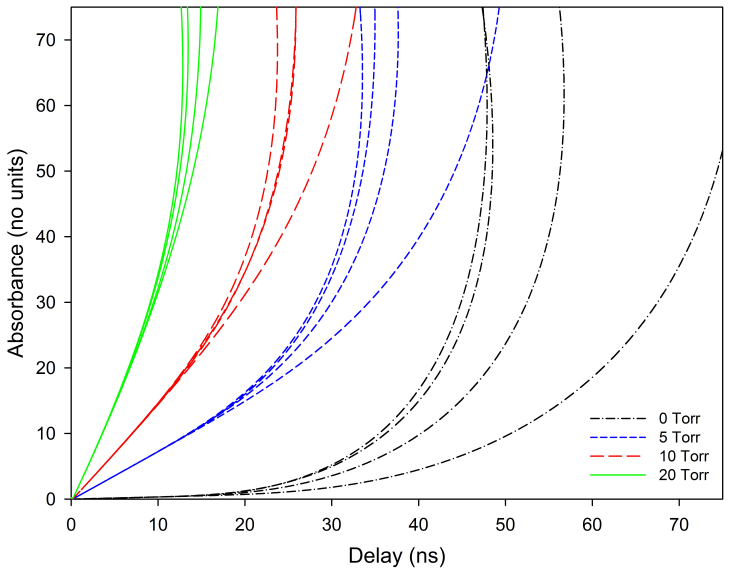

Figure 54. Delay-Absorbance plot showing pressure dependence between 0 Torr **and** 20 Torr**showing detail of delay between** 0 ns **and** 75 ns**.**

Linear Dispersion Delay

Linear dispersion data from Chapters III and IV are used to plot absorbance in Figure 55 as a function of delay and the predicted delay-absorbance curves (from simulation) are provided as reference.

Hole-burning Delay

Delay-absorbance curves in the regions surrounding the rapidly varying absorption created by spectral hole burning are shown in Figure 56 and Figure 57. Data showing all three pump powers (0 mW, 5 mW and 16 mW) are shown in Figure 56. No-pump (0 mW) delay-absorbance curve is shown in Figure 57 with the predicted curve for reference. Deviation from the predicted curve may be indicative of hole burning effects.

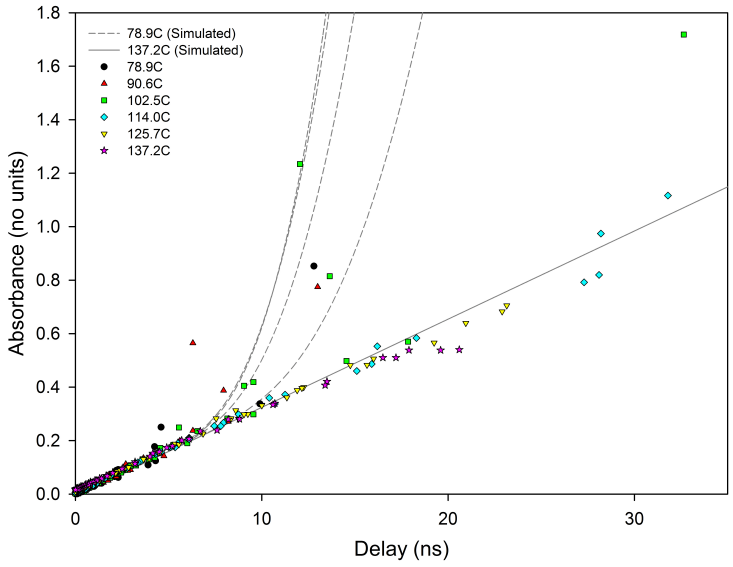

Figure 55. Delay-Absorbance plot showing linear dispersion delay as shown in Figure 7 with predicted delay-absorbance curves.

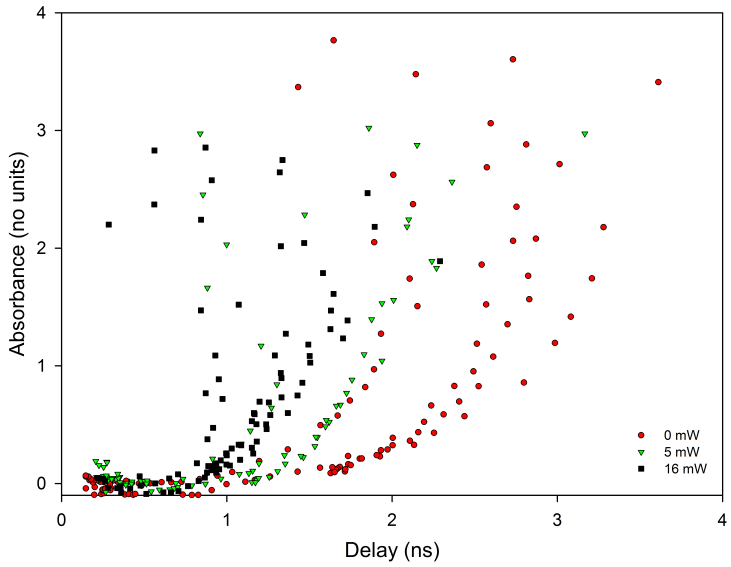

Figure 56. Delay-Absorbance plot showing hole-burning data as shown in Figure 24.

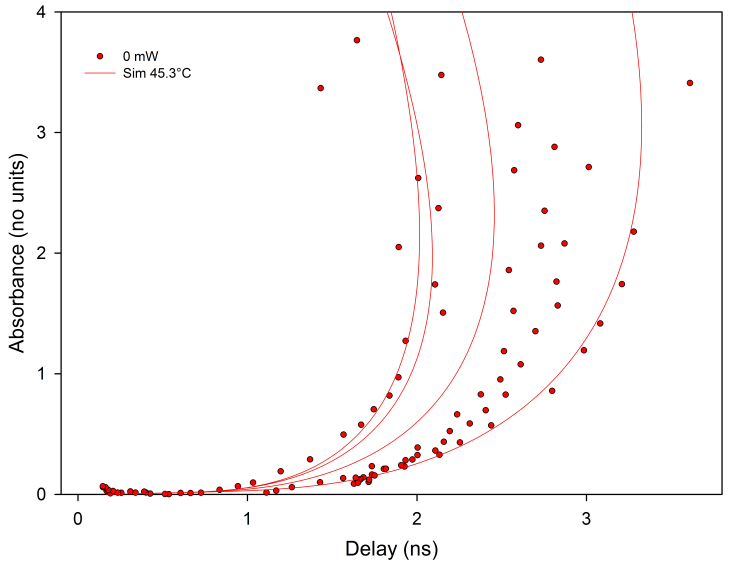

Figure 57. Delay-Absorbance plot showing 0 mW (no pump) hole-burning data as shown in Figure 24 with predicted delay-absorbance curves.

Bibliography

Agarwal, G. S. and T. N. Dey (2003, Dec). Slow light in doppler-broadened two-level systems. *Phys. Rev. A 68*(6), 063816.

Alcock, C. B., V. P. Itkin, and M. K. Horrigan (1984). Vapour pressure equations for the metallic elements:298-2500k. *Canadian Metallurgical Quarterly 23*, 309–313.

Allen, L. and J. H. Eberly (1987). *Optical Resonance and Two-Level Atoms*. Mineola NY: Dover Publications.

Amini, J. M. and H. Gould (2003, Oct). High precision measurement of the static dipole polarizability of cesium. *Phys. Rev. Lett. 91*(15), 153001.

Andalkar, A. and R. B. Warrington (2002, Feb). High-resolution measurement of the pressure broadening and shift of the Cs D_1 and D_2 lines by N_2 and He buffer gases. *Phys. Rev. A 65*(3), 032708.

Anderson, M. D. and G. P. Perram (2010a, Mar). Frequency tuning of the optical delay in cesium D_2 line including hyperfine structure. *Phys. Rev. A 81*(3), 033842.

Anderson, M. D. and G. P. Perram (2010b). Slow light in cesium vapor: pulse delay measurements and predicted delay. In S. M. Shahriar and P. R. Hemmer (Eds.), *Advances in Slow and Fast Light III*, Volume 7612, Bellingham, WA, pp. 76120A. SPIE.

Arimondo, E., M. Inguscio, and P. Violino (1977, Jan). Experimental determinations of the hyperfine structure in the alkali atoms. *Rev. Mod. Phys. 49*(1), 31–75.

Barrat, J. P. and C. Cohen-Tannoudji (1961a). Élargissement et déplacement des raies de résonance magnétique causés par une excitation optique. *Journal de Physique et le Radium 22*, 443.

Barrat, J. P. and C. Cohen-Tannoudji (1961b). Étude du pompage optique dans le formalisme de la matrice densité. *Journal de Physique et le Radium 22*, 329.

Beach, R. J., W. F. Krupke, V. K. Kanz, and S. A. Payne (2004). End-pumped continuous-wave alkali vapor lasers: experiment, model, and power scaling. *Journal of the Optical Society of America B 21*, 2151.

Bernabeu, E. and J. M. Alvarez (1980). Shift and broadening of hyperfine components of the first doublet of cesium perturbed by foreign gases. *Physical Review A 22*, 2690.

Bernath, P. F. (2005). *Spectra of Atoms and Molecules* (2nd ed.). Oxford University Press.

Beverini, N., P. Minguzzi, and F. Strumia (1971). Foreign-gas-induced cesium hyperfine relaxation. *Physical Review A 4*, 550.

Bigelow, M. S., N. N. Lepeshkin, and R. W. Boyd (2003, Mar). Observation of ultraslow light propagation in a ruby crystal at room temperature. *Phys. Rev. Lett. 90*(11), 113903.

Bolda, E. L., R. Y. Chiao, and J. C. Garrison (1993, Nov). Two theorems for the group velocity in dispersive media. *Phys. Rev. A 48*(5), 3890–3894.

Boller, K.-J., A. Imamolu, and S. E. Harris (1991, May). Observation of electromagnetically induced transparency. *Phys. Rev. Lett. 66*(20), 2593–2596.

Born, M. and E. Wolf (1999). *Principles of Optics* (7th ed.). Cambridge University Press.

Boyd, R. W. (2008). *Nonlinear Optics* (3rd ed.). Elsevier Science & Technology Books.

Boyd, R. W. and D. J. Gauthier (2002). "Slow" and "fast" light. *Progress in Optics 43*, 497–530.

Bradley, D. J., G. M. Gale, and P. D. Smith (1970). Self-induced transparency and dispersion delays in potassium vapour. *Nature 225*, 719.

Brillouin, L. (1960). *Wave Propagation and Group Velocity*, Volume 8 of *Pure and Applied Physics*. 111 Fifth Ave, New York, NY: Academic Press Inc.

Budker, D., D. F. Kimball, S. M. Rochester, and V. V. Yashchuk (1999, Aug). Nonlinear magneto-optics and reduced group velocity of light in atomic vapor with slow ground state relaxation. *Phys. Rev. Lett. 83*(9), 1767–1770.

Camacho, R. M., C. J. Broadbent, I. Ali-Khan, and J. C. Howell (2007). All-optical delay of images using slow light. *Physical Review Letters 98*, 043902.

Camacho, R. M., M. V. Pack, and J. C. Howell (2006a). Low-distortion slow light using two absorption resonances. *Physical Review A 73*, 063812.

Camacho, R. M., M. V. Pack, and J. C. Howell (2006b, Sep). Slow light with large fractional delays by spectral hole-burning in rubidium vapor. *Phys. Rev. A 74*(3), 033801.

Camacho, R. M., M. V. Pack, J. C. Howell, A. Schweinsberg, and R. W. Boyd (2007). Wide-bandwidth, tunable, multiple-pulse-width optical delays using slow light in cesium vapor. *Physical Review Letters 98*, 153601.

Casperson, L. and A. Yariv (1970). Longitudinal modes in a high-gain laser. *Applied Physics Letters 17*, 259.

Casperson, L. and A. Yariv (1971). Pulse propagation in a high-gain medium. *Phys Rev Lett 26*, 293.

Chiao, R. Y. and P. W. Milonni (2002). Fast light, slow light. *Optics and Photonics News 13*, 26–30.

Chu, S. and S. Wong (1982a). Linear pulse propagation in an absorbing medium. *Phys Rev Lett 48*, 738.

Chu, S. and S. Wong (1982b). Response. *Phys Rev Lett 49*, 1293.

Courtens, E. and A. Szöke (1968). On consequences of the different phase and signal velocities in self-induced transparency. *Physics Letters 28A*, 296.

Crisp, M. D. (1971, Nov). Concept of group velocity in resonant pulse propagation. *Phys. Rev. A 4*(5), 2104–2108.

Ehrenreich, T., B. Zhdanov, T. Takekoshi, S. P. Phillips, and R. J. Knize (2005). Diode pumped caesium laser. *Electronics Letters 41*, 415.

Faxvog, F. R., C. N. Y. Chow, T. Bieber, and J. A. Carruthers (1970). Measured pulse velocity greater than c in a neon absoprtion cell. *Applied Physics Letters 17*, 192.

Fleischhauer, M., A. Imamoglu, and J. P. Marangos (2005, Jul). Electromagnetically induced transparency: Optics in coherent media. *Rev. Mod. Phys. 77*(2), 633–673.

Fox, M. (2006). *Quantum Optics*. Oxford University Press.

Garrett, C. G. B. and D. E. McCumber (1970). Propagation of a gaussian light pulse through an anomalous dispersion medium. *Phys. Rev. A 1*(2), 305 – 313.

Gerginov, V., A. Derevianko, and C. E. Tanner (2003, Aug). Observation of the nuclear magnetic octupole moment of $cs133$. *Phys. Rev. Lett. 91*(7), 072501.

Griffiths, D. J. (1999). *Introduction to Electrodynamics* (3rd ed.). Prentice Hall.

Grischkowsky, D. (1973, Jun). Adiabatic following and slow optical pulse propagation in rubidium vapor. *Phys. Rev. A 7*(6), 2096–2102.

Harper, W. and B. S. Mathur (1967). Effective formalism in optical pumping. *Physical Review 163*, 163.

Harris, S. E., J. E. Field, and A. Imamoğlu (1990, Mar). Nonlinear optical processes using electromagnetically induced transparency. *Phys. Rev. Lett. 64*(10), 1107–1110.

Hau, L. V. (2001, September). Taming light with cold atoms. *Physics World* -, 35–40.

Hau, L. V., S. E. Harris, Z. Dutton, and C. H. Behroozi (1999, Feb). Light speed reduction to 17 metres per second in an ultracold atomic gas. *Nature 397*, 5.

Hutchings, D. C., M. Sheik-Bahae, D. J. Hagan, and E. W. V. Stryland (1992). Kramers-Kronig relations in nonlinear optics. *Optical and Quantum Electronics 24*, 1–30.

Jackson, J. D. (1999). *Classical Electrodynamics* (3rd ed.). Wiley, John & Sons, Incorporated.

Kasapi, A., M. Jain, G. Y. Yin, and S. E. Harris (1995, Mar). Electromagnetically induced transparency: Propagation dynamics. *Physical Review Letters 74*(13), 2447–2450.

Kash, M. M., V. A. Sautenkov, A. S. Zibrov, L. Hollberg, G. R. Welch, M. D. Lukin, Y. Rostovtsev, E. S. Fry, and M. O. Scully (1999, Jun). Ultraslow group velocity and enhanced nonlinear optical effects in a coherently driven hot atomic gas. *Phys. Rev. Lett. 82*(26), 5229–5232.

Khurgin, J. B. and R. S. Tucker (Eds.) (2009). *Slow Light Science and Applications*. CRC Press/Taylor & Francis Group.

Kim, K., H. S. Moon, C. Lee, S. K. Kim, and J. B. Kim (2003, Jul). Observation of arbitrary group velocities of light from superluminal to subluminal on a single atomic transition line. *Phys. Rev. A 68*(1), 013810.

Krupke, W. F., R. J. Beach, V. K. Kanz, and S. A. Payne (2003). Resonance transition 795-nm rubidium laser. *Optics Letters 28*, 2336.

Loudon, R. (2000). *The Quantum Theory of Light* (3rd ed.). Oxford University Press.

Marangos, J. P. (1998, March 1998). Electromagnetically induced transparency. *Journal of Modern Optics 45*, 471 – 503.

Mathur, B. S., H. Y. Tang, and W. Harper (1970). Light propagation in optically pumped alkali vapors. *Physical Review A 2*, 648.

McCall, S. L. and E. L. Hahn (1967). Self- induced transparency by pulsed coherent light. *Physical Review Letters 18*, 908.

McCall, S. L. and E. L. Hahn (1969, Jul). Self-induced transparency. *Phys. Rev. 183*(2), 457–485.

Menzel, R. (2007). *Photonics: Linear and Nonlinear Interactions of Laser Light and Matter* (2nd ed.). Springer.

Milonni, P. W. (2002). Controlling the speed of light pulses. *Journal of Physics B: Atomic, Molecular and Optical Physics 35*, R31.

Milonni, P. W. (2005). *Fast Light, Slow Light and Left-Handed Light*. Optics and Optoelectronics. Institute of Physics Publishing.

Morgus, L., T. Morgus, T. Drake, and J. Huennekens (2008). Hyperfine state-changing collisions of Cs ($6p_{1/2}$) atoms with argon perturbers. *Physical Review A 77*, 032704.

Noginov, M. A., G. Dewar, M. W. McCall, and N. I. Zheludev (Eds.) (2009). *Tutorials in Complex Photonic Media*. SPIE Press.

Patel, C. K. N. and R. E. Slusher (1967). Self-induced transparency in gases. *Physical Review Letters 19*, 1019.

Pitz, G. A. and G. P. Perram (2008). Pressure broadening of the D_1 and D_2 lines in diode pumped alkali lasers. In C. R. Phipps (Ed.), *High-Power Laser Ablation VII*, Volume 7005, pp. 700526. SPIE.

Purves, G. T., C. S. Adams, and I. G. Hughes (2006). Sagnac interferometry in a slow-light medium. *Physical Review A 74*, 023805.

Rabinowitz, P., S. Jacobs, and G. Gould (1962). Continuously optically pumped cs laser. *Applied Optics 1*, 513.

Rhodes, C. K., A. Szöke, and A. Javan (1968). The influence of level degeneracy on the self-induced transparency effect. *Physical Review Letters 21*, 1151.

Rotondaro, M. D. and G. P. Perram (1997, Apr). Collisional broadening and shift of the rubidium D_1 and D_2 lines ($5\,^2S_{1/2} \rightarrow 5\,^2P_{1/2}, 5\,^2S_{1/2} \rightarrow 5\,^2P_{3/2}$) by rare gases, H_2, D_2, N_2, CH_4, and CF_4. *Journal of Quantitative Spectroscopy and Radiative Transfer 57*(4), 497–507.

Scully, M. O., G. S. Agarwall, O. Kocharovskaya, V. V. Kozlov, and A. B. Matsko (2001). Mixed electromagnetically and self-induced transparency. *Optics Express 8*, 66.

Shakhmuratov, R. N. and J. Odeurs (2008, Mar). Slow light with a doublet structure: Underlying physical processes and basic limitations. *Phys. Rev. A 77*, 033854.

Shakhmuratov, R. N., A. Rebane, P. Mégret, and J. Odeurs (2005, May). Slow light with persistent hole burning. *Phys. Rev. A 71*(5), 053811.

Shi, Z., R. W. Boyd, R. M. Camacho, P. K. Vudyasetu, and J. C. Howell (2007, Dec). Slow-light fourier transform interferometer. *Phys. Rev. Lett. 99*(24), 240801.

Shi, Z., R. W. Boyd, D. J. Gauthier, and C. C. Dudley (2007). Enhancing the spectral sensitivity of interferometers using slow-light media. *Optics Letters 32*, 915.

Siddons, P., C. S. Adams, C. Ge, and I. G. Hughes (2008). Absolute absorption on rubidium d lines: comparison between theory and experiment. *Journal of Physics B: Atomic, Molecular and Optical Physics 41*(15), 155004 (10pp).

Siegman, A. E. (1986). *Lasers*. University Science Books.

Slusher, R. E. and H. M. Gibbs (1972). Self-induced transparency in atomic rubidium. *Physical Review A 5*, 1634.

Steck, D. A. (2009, 12 August). Cesium D line data. Revision 2.1.2.

Tanaka, H., H. Niwa, K. Hayami, S. Furue, K. Nakayama, T. Kohmoto, M. Kunitomo, and Y. Fukuda (2003, Nov). Propagation of optical pulses in a resonantly absorbing medium: Observation of negative velocity in rb vapor. *Phys. Rev. A 68*(5), 053801.

Thompson, W. J. (1993, Nov/Dec). Numerous neat algorithms for the voigt profile function. *Computers in Physics 7*(6), 627–631.

Tornos, J. and J. C. Amare (1986). Hyperfine relaxation of an optically pumped cesium vapor. *Applied Spectroscopy 40*, 596.

Tucker, R. S., P.-C. Ku, and C. J. Chang-Hasnain (2005). Slow-light optical buffers: capabilities and fundamental limitations. *IEEE/OSA Journal of Lightwave Technology 23*, 4046.

Vudyasetu, P. K., R. M. Camacho, and J. C. Howell (2008, Mar). Storage and retrieval of multimode transverse images in hot atomic rubidium vapor. *Physical Review Letters 100*, 123903. (Received 5 December 2007; published 26 March 2008).

Xiao, M., Y.-q. Li, S.-z. Jin, and J. Gea-Banacloche (1995, Jan). Measurement of dispersive properties of electromagnetically induced transparency in rubidium atoms. *Phys. Rev. Lett. 74*(5), 666–669.

Zibrov, A. S., M. D. Lukin, L. Hollberg, D. E. Nikonov, M. O. Scully, H. G. Robinson, and V. L. Velichansky (1996, May). Experimental demonstration of enhanced index of refraction via quantum coherence in rb. *Phys. Rev. Lett. 76*(21), 3935–3938.

REPORT DOCUMENTATION PAGE

Form Approved
OMB No. 074-0188

1. REPORT DATE *(DD-MM-YYYY)*	**2. REPORT TYPE**	**3. DATES COVERED** *(From – To)*
15-12-2010	Doctoral Dissertation	Sep 2007 - Sep 2010

4. TITLE AND SUBTITLE

Tunable optical delay in Doppler-broadened cesium vapor

5a. CONTRACT NUMBER

5b. GRANT NUMBER

5c. PROGRAM ELEMENT NUMBER

6. AUTHOR(S)

Monte D. Anderson, LtCol, USAF

5d. PROJECT NUMBER

5e. TASK NUMBER

5f. WORK UNIT NUMBER

7. PERFORMING ORGANIZATION NAMES(S) AND ADDRESS(S)

Air Force Institute of Technology
Graduate School of Engineering and Management (AFIT/EN)
2950 Hobson Way
WPAFB OH 45433-7765

8. PERFORMING ORGANIZATION REPORT NUMBER

AFIT/DS/ENP/10-S01

9. SPONSORING/MONITORING AGENCY NAME(S) AND ADDRESS(ES)

Dr. Harro Ackermann
High Energy Laser Joint Technology Office (HEL-JTO)
801 University Blvd. SE, Suite 209
Albuquerque, NM 87106

10. SPONSOR/MONITOR'S ACRONYM(S)

HEL-JTO

11. SPONSOR/MONITOR'S REPORT NUMBER(S)

12. DISTRIBUTION/AVAILABILITY STATEMENT

APPROVED FOR PUBLIC RELEASE; DISTRIBUTION UNLIMITED

13. SUPPLEMENTARY NOTES

14. ABSTRACT

Variable-delay tunable optical delay line or optical buffers are critical for the development of all-optical networks components as well as interferometry and analytic instruments. Recent research on slow light may hold the key for the development of the first practical tunable optical delay device. In this research the linear dispersion delay model is a valuable improvement over currently used Lorentzian approximations and provides a significant addition to the field tunable slow light delays. This work presents the first reported spectral hole-burnt linear dispersion delay effects in an alkali vapor. The hyperfine relaxation observations present insight into the complex bleach wave dynamics during a high-intensity pulsed pump in DPAL systems.

15. SUBJECT TERMS

Slow Light, Optical Delay, Alkali Vapor, Diode-Pumped Alkali Laser (DPAL)

16. SECURITY CLASSIFICATION OF:			**17. LIMITATION OF ABSTRACT**	**18. NUMBER OF PAGES**	**19a. NAME OF RESPONSIBLE PERSON**
a. REPORT	**b. ABSTRACT**	**c. THIS PAGE**			Dr. Glen P. Perram, AFIT/ENP
U	U	**U**	**U**	154	**19b. TELEPHONE NUMBER** *(Include area code)* (937) 255-3636, x4504; glen.perram@afit.edu

Standard Form 298 (Rev. 8-98)
Prescribed by ANSI Std. Z39-18